New insights into Arctic environmental change from high-temporal resolution satellite remote sensing

by
Sarah W. Cooley

B.S. Geological Sciences – Geophysics, University of North Carolina at Chapel Hill, 2015
MPhil Polar Studies, University of Cambridge, 2016

A Dissertation submitted in partial fulfillment of the requirements for the Degree of Doctor of Philosophy in the Department of Earth, Environmental and Planetary Sciences at Brown University

Providence, Rhode Island
May 2020

This dissertation by Sarah W. Cooley is accepted in its present form by the Department of Earth, Environmental and Planetary Sciences as satisfying the dissertation requirement for the degree of Doctor of Philosophy.

Date____________________________ ______________________________________

Laurence C. Smith, Advisor

Recommended to the Graduate Council

Date____________________________ ______________________________________

Meredith G. Hastings, Reader

Date____________________________ ______________________________________

Amanda H. Lynch, Reader

Date____________________________ ______________________________________

John F. Mustard, Reader

Date____________________________ ______________________________________

Karen E. Frey, Reader

Approved by the Graduate Council

Date____________________________ ______________________________________

Andrew G. Campbell
Dean of the Graduate School

CURRICULUM VITAE

Sarah W. Cooley

Institute at Brown for Environment and Society
85 Waterman St, Providence, RI 02906
sarah-cooley.com | sarah_cooley@brown.edu

Education

2020 **Brown University**
PhD Candidate in Earth, Environmental and Planetary Sciences
Graduate Affiliate of the Institute at Brown for Environment and Society
Advisor: Prof. Laurence C. Smith. Thesis: *New insights into Arctic environmental change from high-temporal resolution satellite remote sensing*

2016-2017 **University of California, Los Angeles**
PhD Student in Geography. Advisor: Prof. Laurence C. Smith

2016 **University of Cambridge**
MPhil with Distinction in Polar Studies, Scott Polar Research Institute.
Advisor: Dr. Poul Christoffersen. Thesis: *A 16-year record of supraglacial lake extent in West Greenland: analysis of inland expansion and rapid drainage events*

2015 **University of North Carolina at Chapel Hill**
B.S. with Highest Distinction and Highest Honors in Geological Sciences – Geophysics, Minor in Mathematics. GPA 3.9/4.0. Honors Thesis: *Observing spatial and temporal patterns in Arctic river ice breakup using MODIS imagery*

Grants and Awards (total $583,100)

2020-2023 **Stanford Science Fellowship** ($273,000)

2020 **Building Future Faculty Fellow –** North Carolina State University (*postponed due to COVID-19)

2019 **Arctic Futures 2050 Early Career Travel Grant** ($750)

2019 **IUGG Early Career Travel Grant** ($750)

2019 **GSA Graduate Student Research Grant** ($1,600)

2017 **AGU Outstanding Student Paper Award** – Cryosphere Division

2017-2020 **Planet Labs Research Ambassador** – one of 14 researchers selected to receive free, unrestricted access to Planet Labs satellite imagery

2017 **UCLA Canadian Studies Fellowship** ($1,500)

2015-2020 **National Science Foundation Graduate Research Fellowship** ($138,000)

2015-2016 **Gates Cambridge Scholarship** ($40,000)

2015 **Op White Award** – UNC Chancellor's Award for the outstanding student in Geological Sciences

2015 **First Prize Undergraduate Presentation** – UNC Geoscience Research Symposium

2014 **Phi Beta Kappa**

2011-2015 **Morehead-Cain Scholarship** – the US's oldest full merit scholarship and funded summer enrichment program ($122,000)

2011-2015 **National Merit Scholar** ($5,500)

Peer-Reviewed Publications

In Review or In Revision:

14. Pitcher, L.H., L.C. Smith, **S.W. Cooley,** A. Zaino, R. Carlson, J. Pettit, C.J. Gleason, T. Minear, J.V. Fayne, M. Harlan, T. Langhorst, S.N. Topp, W. Dolan, E. Kyzivat, A. Pietroniro, D. Yang, T. Carter, C. Onclin, D. Moreira, M. Berge-Nguyen, J.-F. Cretaux and T.M. Pavelsky (in review), Advancing field-based GPS surveying for validation of remotely sensed water surface elevation products, *Frontiers in Earth Science – Hydrosphere*

13. Fayne, J.V., L.C. Smith, L.H. Pitcher, E.D. Kyzivat, **S.W. Cooley**, M.G. Cooper, M. Denbina, A. Chen, X. Wu, C. Chen and T.M. Pavelsky (in revision), First Airborne Observations of Arctic-Boreal Water Surface Elevations from AirSWOT Ka-Band InSAR and LVIS LiDAR, *Environmental Research Letters*

12. Ryan, J.C., L.C. Smith, **S.W. Cooley**, L.H. Pitcher, and T.M. Pavelsky (in revision), Toward global characterization of inland water reservoirs using ICESat-2 altimetry and climate reanalysis, *Geophysical Research Letters*

In Press:

11. **Cooley, S.W.,** J.C. Ryan, L.C. Smith, C. Horvat, B. Pearson, B. Dale and A. Lynch (in press), Coldest Canadian Arctic communities face greatest reductions in shorefast sea ice, *Nature Climate Change*

Published:

10. Ryan, J.C., L.C. Smith, M. Wu, **S.W. Cooley,** C. Miege, L. Montgomery, L. Koenig, X. Fettweis, B. Noel and M. van den Broeke (2020), Evaluation of CloudSat's cloud-profiling radar for mapping snowfall rates across the Greenland Ice Sheet, *Journal of Geophysical Research – Atmospheres.* doi.org/10.1029/2019JD031411

9. Kyzivat, E.D., L.C. Smith, L.H. Pitcher, J.V. Fayne, **S.W. Cooley**, M.G. Cooper, S.N. Topp, T. Langhorst, M. Harlan, C. Horvat, C.J. Gleason and T.M. Pavelsky (2019), A high-

resolution airborne color-infrared camera water mask for the NASA ABoVE campaign, *Remote Sensing.* doi.org/10.3390/rs11182163

8. Ryan, J.C., L.C. Smith, D. Van As, **S.W. Cooley**, M.G. Cooper, L.H. Pitcher and A. Hubbard (2019), Greenland Ice Sheet surface melt amplified by snowline migration and bare ice exposure, *Science Advances.* doi.org/10.1126/sciadv.aav3738
    - Brown University press release: Migrating snowline plays outsized role in setting pace of Greenland ice melt
    - Coverage in Nature, Quartz

7. **Cooley, S.W.,** L.C. Smith, J.C. Ryan, L.H. Pitcher and T.M. Pavelsky (2019), Arctic-Boreal lake dynamics revealed using CubeSat imagery, *Geophysical Research Letters.* doi.org/10.1029/2018GL081584
    - Brown University press release: Tiny satellites reveal water dynamics in thousands of northern lakes

6. Pitcher, L., T. Pavelsky, L. Smith, D. Moller, E. Altenau, G. Allen, C. Lion, D. Butman, **S. Cooley**, J. Fayne, and M. Bertram (2018), AirSWOT InSAR mapping of surface water elevations and hydraulic gradients across the Yukon Flats Basin, Alaska, *Water Resources Research*. doi.org/10.1029/2018WR023274

5. Cooper, M.G., J. Schaperow, **S.W. Cooley**, S. Alam, L.C. Smith, and D. Lettenmaier (2018), Climate elasticity of low flows in the maritime western US mountains, *Water Resources Research, 54.* doi.org/10.1029/2018WR022816

4. Cooper, M.G., L.C. Smith, A.K. Rennermalm, C. Miege, L.H. Pitcher, J.C. Ryan, K. Yang and **S.W. Cooley** (2018), Near surface meltwater storage in low-density bare ice of the Greenland ice sheet ablation zone, *The Cryosphere 12,* 955 – 970. doi.org/10.5194/tc-12-955-2018

3. **Cooley, S.W.**, L.C. Smith, L. Stepan and J. Mascaro (2017), Tracking dynamic northern surface water changes with high frequency Planet CubeSat imagery, *Remote Sensing 9,* 1309. doi.org/10.3390/rs9121306

2. **Cooley, S.W.** and P. Christoffersen (2017), Observation bias correction reveals more rapidly draining lakes on the Greenland Ice Sheet, *Journal of Geophysical Research – Earth Surface 122.* doi.org/10.1002/2017JF004255

1. **Cooley, S.W.** and T.M. Pavelsky (2016), Spatial and temporal patterns in Arctic river ice breakup revealed by automated ice detection using MODIS imagery, *Remote Sensing of Environment 175,* 310-322. doi.org/10.1016/j.rse.2016.01.004

Selected Conference Presentations

**Oral Presentation **Invited*

2019 ***Cooley, S.W.,** J.C. Ryan, L.C. Smith, C.H. Horvat, B. Pearson, B. Dale and A. Lynch, Sensitivity of shorefast ice breakup to a warming climate in Arctic communities, *AGU Fall Meeting, San Francisco, California.*

2019 ****Cooley, S.W.,** L.C. Smith, J.C. Ryan, L.H. Pitcher and T.M. Pavelsky, Tracking fine-scale changes in surface water using CubeSat imagery (Panelist for Centennial Session "Past and Future of Remote Sensing of Hydrology"), *AGU Fall Meeting, San Francisco, California.*

2019 **Cooley, S.W.,** J.C. Ryan, B. Dale, C.H. Horvat, L.C. Smith, N. Cuba and A. Lynch, Combining satellite remote sensing and traditional knowledge to understand mechanisms of shorefast ice breakup in the Arctic, *Arctic Futures 2050, Washington, D.C.*

2019 ****Cooley, S.W.,** L.C. Smith, J.C. Ryan, L.H. Pitcher and T.M. Pavelsky, Arctic-Boreal lake dynamics revealed using CubeSat imagery, *IUGG General Assembly, Montreal, Canada.*

2018 ***Cooley, S.W.,** L.C. Smith, J.C. Ryan, L.H. Pitcher and T.M. Pavelsky, Arctic-Boreal surface water dynamics tracked using CubeSat imagery, *AGU Fall Meeting, Washington, D.C.*

2018 **Cooley, S.W.**, L.C. Smith, L.H. Pitcher, T.M. Pavelsky and S.N. Topp, Tracking seasonal evolution of surface water extent in the Yukon Flats, Alaska and the Canadian Shield, *NASA Arctic Boreal Vulnerability Experiment* (*ABoVE) Science Team Meeting, Seattle, Washington.*

2017 ***Cooley, S.W.**, L.C. Smith, L.H. Pitcher, T.M. Pavelsky and S.N. Topp, Tracking seasonal evolution of surface water extent in Central Alaska and the Canadian Shield, *AGU Fall Meeting, New Orleans, Louisiana.*

2016 ***Cooley, S.W.** and P. Christoffersen, Characterizing the frequency and elevational extent of rapid drainage events in West Greenland, *AGU Fall Meeting, San Francisco, California.*

2016 **Cooley, S.W.** and T.M. Pavelsky, Spatial and temporal patterns in Arctic river ice breakup revealed by automated ice detection from MODIS imagery, *EGU General Assembly, Vienna, Austria.*

Invited Talks

Feb 2020 **University of Illinois,** "Tracking high latitude hydrology from space: how advancing technologies allow us to see more than ever before", Seminar, Department of Geology, Champaign-Urbana, IL

Feb 2020 **University of Washington,** “Tracking high latitude surface water dynamics using CubeSat imagery and machine learning”, Satellite Image Analysis Seminar, eScience Institute, Seattle, WA

Feb 2020 **University of Washington,** “New insights into community-scale changes in shorefast sea ice from satellite remote sensing”, Environmental Fluid Mechanics Seminar, Applied Physics Laboratory, Seattle, WA

Feb 2020 **Brown University,** “New insights into community-scale changes in shorefast sea ice from satellite remote sensing”, Lunch Bunch, Department of Earth, Environmental and Planetary Sciences, Providence RI

Jan 2020 **University of Oregon,** “Tracking high latitude hydrology from space: how advancing technologies allow us to see more than ever before”, Colloquium, Department of Geography, Eugene, OR

Jan 2020 **University of Pittsburgh,** “Tracking high latitude hydrology from space: how advancing technologies allow us to see more than ever before”, Colloquium, Department of Geology and Environmental Science, Pittsburgh, PA

Nov 2018 **NASA Surface Water Ocean Topography (SWOT) Cal/Val Workshop, “**Mapping Inundation Extent for SWOT Cal/Val”, Pasadena, CA

Nov 2018 **Planet Labs**, “Tracking Arctic-Boreal Surface Water Dynamics using Planet Imagery”, San Francisco, CA

May 2018 **NASA Inundation Extent Workshop**, “Mapping inundation extent using optical imagery”, Boulder, CO

Feb 2018 **Brown University**, “Tracking the Seasonal Evolution of Arctic surface water extent using CubeSat imagery”, Lunch Bunch, Department of Earth and Environmental Sciences, Providence, RI

Apr 2017 **NASA Earth-to-Sky Climate Change Science Communication Conference**, “Draining lakes and melting ice: Changes in the hydrology of the Northwest Territories”, Yellowknife, NWT, Canada

Fieldwork

Apr-May 2019 **Uummannaq, Greenland** – Part of an interdisciplinary team working on co-production of shorefast ice knowledge in Uummannaq Fjord, North Greenland. Funded by NSF Navigating the New Arctic Grant #1835473 (PI Jonathan Ryan) and a GSA Graduate Student Research Grant.

March 2018 **Nunavut, Canada** – Participant in the inaugural Sentinel North International Arctic Field School in Iqaluit, Nunavut, Canada. Funded by an IBES Graduate Travel and Training Grant.

Jun-Aug 2017 **Northern Canada and Alaska** – Six weeks studying northern surface water as part of NASA's Arctic Boreal Vulnerability Experiment (ABoVE). Performed ground validation for NASA AirSWOT and surveyed 50+ lakes across Saskatchewan, the Northwest Territories and Alaska. Funded by NASA Grants #NNX17AC60A and NNX16AH83G (PI Laurence Smith).

Jun-Aug 2016 **Kangerlussuaq, Greenland** – Six weeks studying the seasonal evolution of the surface hydrology of the ice sheet margin. Funded by NASA Grant #NNX14AH93G (PI Laurence Smith).

Jun-Aug 2013 **Juneau Icefield, Alaska and Canada** – Participant in the Juneau Icefield Research Program. Traversed the Juneau Icefield in Southeast Alaska and British Columbia and conducted independent research on surface strain rates on Taku Glacier. Funded by the Morehead-Cain Scholarship Program.

Teaching and Mentoring

Brown Department of Earth, Environmental and Planetary Sciences, Providence, RI

Spring 2020 Guest Lecturer, GEOL 1330, Global Environmental Remote Sensing
Fall 2019 Sheridan Center for Teaching and Learning Certificate I
Summer 2019 Undergraduate Research Mentor for Vida Steiro
Spring 2019 Guest Lecturer, GEOL 1330, Global Environmental Remote Sensing
Spring 2019 Teaching Assistant and Guest Lecturer, GEOL 1310, Global Water Cycle
Spring 2018 Guest Lecturer, GEOL 1330, Global Environmental Remote Sensing

UNC Department of Geological Sciences, Chapel Hill, NC

Fall 2014 Undergraduate Teaching Assistant, GEOL 72H, Field Geology of Eastern California
Fall 2012 Undergraduate Teaching Assistant, GEOL 72H, Field Geology of Eastern California

Outreach

The Polar Museum, Scott Polar Research Institute, Cambridge, UK 2015-2016
Polar Science Outreach Volunteer

Mount Rainier National Park, Paradise, WA June-September 2015
Geoscientist-in-the-Park (Interpretation Division)

UNC Office for Undergraduate Research, Chapel Hill, NC 2014-2015
Undergraduate Research Ambassador

Media

Planet Pulse, More Sats. More Science., Dec. 19, 2017

AGU Eos, *Airborne surveys examine water levels of lakes perched on permafrost*, Dec. 14, 2017

UNC Spotlights, *Carolina student earns Gates Cambridge Scholarship***,** Feb. 12, 2015

Memberships, Service and Skills

Member:	American Geophysical Union (2016-present) American Association of Geographers (2018-present) Geological Society of America (2019-present) Association of Early Career Polar Scientists (2015-present)
Reviewer:	Science Advances Permafrost and Periglacial Processes
Convener:	Remote Sensing of Hydrology and Environmental Change in the Cryosphere, AGU Fall Meeting 2019
Organizer:	Brown Department of Earth Sciences Graduate Student Conference, 2018
Computers:	Expert in Matlab, ArcGIS, Python, QGIS and ENVI.
Fieldwork:	FAA Certified Remote UAS Pilot NOLS Certified Wilderness First Responder

Acknowledgements

I first would like to thank my advisor, Larry Smith, for putting up with me the past four years. Across two institutions, sabbatical, a book and many other changes, it has not been an easy journey but I have emerged out the other side a much better scientist for it.

I am so grateful to everyone in the Department of Earth, Environmental and Planetary Sciences at Brown for welcoming me here and enabling me to have an easy transition from UCLA. Three years is a very short time to pass through a department and I greatly appreciate all the support I have received during this time. Jack Mustard has provided me with countless advice and support and I am particularly grateful to him for pushing me to remember to put the science first and the remote sensing second. Jim Russell and Meredith Hastings were instrumental in helping me transition to Brown and for always being willing to provide advice when needed. Amanda Lynch and the staff of IBES have made me feel very welcome and have provided me with a home at the office. DEEPS and IBES are both wonderful places and I feel very fortunate to have had such a positive experience here over the past three years.

I owe a huge thank you to Joe Mascaro and Planet's Education and Research Program for giving me a chance at the start of my PhD and for their continued support over the past three years. Working with CubeSat imagery was one of the best decisions I have ever made and much of this dissertation would not have been possible if not for their trust and willingness to provide me with data. Thank you also to Karen Frey for her willingness to serve as my external reader and for making the trek down to Providence.

I am indebted to the many teachers and mentors throughout my educational journey who set me along this path. First to my high school math teacher, Lori Bohan, for supporting me through ups and downs and instilling within me the confidence to pursue this sort of career. Thanks to Allen Glazner and Drew Coleman at the University of North Carolina for convincing me to major in geology and taking an interest in me as a first-year student. The Morehead-Cain Scholarship program at UNC provided me with unparalleled support and opportunity as an undergrad and set me up for future success. Thanks also to my masters advisor, Poul Christoffersen, and to many friends and colleagues at the Scott Polar Research Institute at the University of Cambridge. I will always look back very fondly on my time at SPRI and feel that I grew enormously as a scientist and person during my year there. Lastly, I am very grateful to Tamlin Pavelsky for first introducing me to hydrology and remote sensing and for many years of advice and support. He is an excellent example of what a scientist, advisor and mentor should be.

I wish to thank all members of the Smith research group for their support and friendship over the past four years. Splitting a group in half from coast to coast is never an ideal situation, but I am grateful that we have managed to retain our group dynamic, collegiality and willingness to collaborate and help each other. My field experiences with Smith group members and other colleagues have been a particular highlight of my time in graduate school and have taught me that fieldwork goes best when everyone gets along and is having fun! Thank you to Matt, Lincoln, Johnny, Larry, Tamlin, Simon, Chris, Brigt and everyone else I have had the pleasure of working with in Greenland, Canada and/or Alaska. Thanks especially to Lincoln Pitcher for helping guide me through my PhD, teaching me how to be a good field scientist, and most importantly being a friend I could always reach out to even when thousands of miles away. And there aren't enough words to thank Johnny Ryan, who over the past three years has provided unwavering support and pushed me to be the best scientist and person I could possibly be. I cannot imagine having gone on this journey without him.

I lastly would like to thank my family, without whose support none of this would be possible. My mom has supported me through moving across the country and traveling around the world in support of this goal. Even though pursuing a PhD in earth science is very far from her own experience, she has always stood behind me and only rarely questioned my decisions! Alex, Robert, Jim and the rest of my family also deserve many thanks for their support and for only rarely asking me about my research and future plans.

Finally, this dissertation is dedicated to my father, who gifted me his love of the outdoors, fascination with science and never-ending desire to learn. I so wish I could share tales of my Arctic adventures with him but I know he would be so proud that this what I have chosen to do with my life.

TABLE OF CONTENTS

LIST OF FIGURES

Chapter 1: Coldest Canadian Arctic Communities Face Greatest Reductions in Shorefast Sea Ice

Chapter 2: Tracking Dynamic Northern Surface Water Changes with High-Frequency Planet CubeSat Imagery

Chapter 3: Arctic-Boreal Lake Dynamics Revealed using CubeSat Imagery

Main Text Figures

Supplementary Figures

LIST OF TABLES

Introduction

Since the start of the industrial era, the Earth's climate has warmed due to anthropogenic emissions of greenhouse gases. Some of the fastest rates of warming, often more than twice the global average, are occurring in northern and boreal regions due to Arctic amplification (Serreze & Barry, 2011). This rapid climate change in the northern high latitudes has had dramatic environmental consequences, including reductions in sea ice extent (Notz & Stroeve, 2016), melting of glaciers and ice sheets (Mouginot et al., 2019), thawing permafrost (Hollesen et al., 2015) and an intensifying northern hydrologic cycle (Rawlins et al., 2010). Many of these changes feedback into global climate through sea level rise (Bamber et al., 2019), carbon release from permafrost thaw (Turetsky et al., 2020) and sea ice-atmosphere linkages (Francis & Vavrus, 2012). Arctic environmental change also has notable consequences for local communities, such as increased water resource vulnerability (Alessa et al., 2008), riskier transportation due to loss of sea ice and river ice (Ford et al., 2019), and changes to subsistence hunting practices (Ford et al., 2006). Over the next few decades, Arctic climate warming is expected to intensify, exacerbating global impacts and further threatening the environment, ecosystems, and people of the Arctic.

Documenting Arctic environmental change and understanding its effects first requires high quality observations. Our longest instrumental records of Arctic climate come from meteorological reports and river gauging stations. Air temperature records, often beginning in the 1800s, provide key evidence of anthropogenic warming (Box, 2002; Overland et al., 2004). Observations of river and lake ice extend back 150 years or more and have revealed consistent trends towards a shorter duration of ice cover (Magnuson et al., 2000). Large Eurasian rivers have been gauged since the 1930s, and the notable increase in river discharge they record is one of the best-documented impacts of climate change in the Arctic (Peterson et al., 2002). Even shorter in situ records, such as permafrost borehole temperatures, provide important insights into key indicators of environmental change (Biskaborn et al., 2019). Due to the vastness, remoteness and lack of infrastructure in Arctic regions, however, ground data in Arctic regions is generally sparse and limited to a few populated areas and research stations. Furthermore, changing geopolitical priorities mean that in many northern regions, ground stations are no longer being maintained (Shiklomanov et al., 2002). Despite the high quality and importance of these ground-based measurements, in situ data therefore are insufficient for understanding Arctic environmental change.

Over the past few decades, rapid developments in satellite remote sensing have transformed our ability to investigate Arctic environmental change at broad spatial scales. Passive microwave satellite sensors such as the Scanning Multichannel Microwave Radiometer (SMMR) available since 1979 have documented the precipitous decline in pan-Arctic sea ice extent (Stroeve et al., 2012). The suite of Landsat satellites have provided medium to high resolution data since 1972, which has been vital for constraining decadal-scale changes in surface water (Pekel et al., 2016), mapping ice sheet and glacier velocities (Tedstone et al., 2015), and observing greening of Arctic vegetation (Fraser et al., 2011). The launch of NASA's Moderate Resolution Imaging Spectrometer (MODIS) aboard the Terra and Aqua satellites in 2000 increased the temporal detail of observations, providing valuable insight into changes in the albedo of the Greenland Ice Sheet (Box et al., 2012) and spatiotemporal variability in river ice breakup (Cooley & Pavelsky, 2016). While advances in both satellite sensors and techniques for analyzing satellite imagery over the past few decades have been critical for the development of scientific understanding about Arctic climate change, however, these traditional satellite sensors are all limited by a tradeoff between high spatial and high temporal resolution imagery. This tradeoff has precluded research into dynamic processes that occur at daily to weekly time scales, meaning that many processes, such as coastal sea ice dynamics and sub-seasonal fluctuations in lake area, remain understudied or poorly understood.

In the past few years, there has been rapid development in the capacity to observe fine-scale, dynamic processes from space. Although MODIS launched in 2000, and is thus not a new advance, its record now spans two decades and therefore enables new insights into decadal-scale changes into daily-scale processes. More recently, the development and launch of hundreds of small breadbox-sized satellites known as CubeSats over the past few years by companies such as Planet Labs now provides daily data of the entire Earth's surface at 3m resolution. In this dissertation, I demonstrate how these advances in technology combined with novel methodological approaches enable better understanding of dynamic Arctic environmental change.

In **Chapter 1**, I present new insights into the processes controlling shorefast sea ice breakup using the now decadal-scale MODIS record. Shorefast sea ice, also known as landfast ice, represents a small percentage of the total Arctic sea ice cover, yet it is of outsized importance to Arctic communities which rely on the seasonal stable shorefast ice platform for protection against erosion, access to traditional hunting grounds and transportation between otherwise isolated communities (Baztan et al., 2017; Eicken, 2010; Gearheard et al., 2006). While the decline of sea ice in the Arctic Ocean is well-documented, the 25 x 25 km resolution of passive microwave sensors used to observe sea ice is unable to resolve shorefast ice processes which occur along coastal margins. Consequently, little is known about drivers of shorefast ice growth and breakup and how it might change in the future. To determine controls on breakup timing and project their changes into the future, we develop a novel method to map the timing of shorefast ice breakup using MODIS imagery around 28 communities in Northern Canada and Greenland over 2000-2018. While we do not observe any trends in breakup timing over the 19-year period, we find that breakup timing is strongly correlated with springtime air temperature. By combining these air temperature sensitivities with climate model outputs, we then quantify projected future reductions in springtime shorefast ice season by 2100, which range from 5 to 44 days earlier. Surprisingly, we find the coldest and northernmost Arctic communities are projected to experience the most dramatic reductions in springtime ice duration. This research emphasizes the localized nature of climate change and highlights a greater than expected vulnerability in the high Arctic.

In **Chapter 2**, I present our initial research testing the value of newly available CubeSat imagery for mapping fine-scale changes in northern surface water dynamics. The northern high latitudes are home to the highest density of lakes on Earth (Pekel et al., 2016). Understanding how these lakes change on both seasonal and interannual time scales is critical for assessing environmental sensitivity to climate change and monitoring the hydrology of these remote and generally poorly studied regions. As Arctic and Boreal lakes are net sources of carbon dioxide and methane, variations in lake surface area also modulate terrestrial carbon dioxide and methane emissions to the atmosphere, a highly important but little understood component of the carbon cycle (Bastviken et al., 2011; Raymond et al., 2013). While many studies have examined decadal-scale changes in northern surface water using Landsat and other high spatial resolution sensors (e.g. Chen et al., 2014; Nitze et al., 2017; Olthof et al., 2015; Smith et al., 2005), the coarse temporal resolution of these sensors precludes their use for observing seasonal fluctuations and has therefore limited research into intra-annual surface water variability. Starting in 2016, however, the advent of new small satellites known as CubeSats operated by companies such as Planet has created new opportunities for mapping fine-scale surface water dynamics. Through operation in a constellation of more than a hundred satellites, CubeSat imagery now provides near-daily data of the entire Earth's surface at 3 m resolution, a significant step-change from previous observation capabilities. Due to the newness of this technology, however, it first required accuracy assessment and development of new methodology. We therefore first test the use of CubeSat imagery to map changes in water area over a 625 km^2 area of the Yukon Flats in Central Alaska during summer 2016. In one of the very first applications of CubeSat imagery, we identify several unique challenges associated with CubeSat imagery, including lack of an automated cloud mask, lack of atmospheric correction, radiometric calibration uncertainty and geolocation error. Despite these challenges, however, we conclude that CubeSat imagery can be used to accurately map water area and the high spatial and temporal resolution of CubeSat imagery make it valuable for understanding dynamic environmental change.

In **Chapter 3**, I present our efforts to use CubeSat imagery to track changes in lake area over four large study regions in Northern Canada and Alaska covering diverse climatic and physiographic terrains. Chapter 2 demonstrates that CubeSat imagery has scientific value, yet this work focuses on a small area and requires significant manual intervention. The real test of CubeSat imagery's utility for hydrologic research is thus whether it can be used to track changes in surface water over large areas. To do this, we develop a novel method that incorporates object-based lake-tracking and machine learning-derived observation filtering to overcome the key challenges of CubeSat imagery. Through analysis of >75,000 images and >25 TB of data, we identify a surprisingly hydrologically dynamic landscape and a near-ubiquitous decline in lake area between May and October. We find that the high spatial and high temporal resolution of CubeSat imagery enables observation of small shoreline fluctuations unobservable by previous sensors which cumulatively sum to substantial seasonal variability. These results have implications for the estimation of freshwater carbon emissions, which are often higher along seasonally fluctuating lake margins.

References

Alessa, L., Kliskey, Æ. A., Lammers, Æ. R., Arp, Æ. C., White, D., Hinzman, Æ. L., & Busey, Æ. R. (2008). The Arctic Water Resource Vulnerability Index : An Integrated Assessment Tool for Community Resilience and Vulnerability with Respect to Freshwater, 523–541. https://doi.org/10.1007/s00267-008-9152-0

Bamber, J. L., Oppenheimer, M., Kopp, R. E., Aspinall, W. P., & Cooke, R. M. (2019). Ice sheet contributions to future sea-level rise from structured expert judgment, *116*(23). https://doi.org/10.1073/pnas.1817205116

Bastviken, D., Cole, J., Pace, M., & Tranvik, L. (2004). Methane emissions from lakes: Dependence of lake characteristics, two regional assessments, and a global estimate. *Global Biogeochemical Cycles*, *18*(4), 1–12. https://doi.org/10.1029/2004GB002238

Bastviken, D., Tranvik, L. J., Downing, J. A., Crill, P. M., & Enrich-Prast, A. (2011). Freshwater methane emissions offset the continental carbon sink. *Science*, *331*(6013), 50. https://doi.org/10.1126/science.1196808

Baztan, J., Cordier, M., Huctin, J., & Zhu, Z. (2017). Life on thin ice: Insights from Uummannaq, Greenland for connecting climate science with Arctic communities. *Polar Science*, *13*, 100–108. https://doi.org/10.1016/j.polar.2017.05.002

Biskaborn, B. K., Smith, S. L., Noetzli, J., Matthes, H., Vieira, G., & Streletskiy, D. A. (2019). Permafrost is warming at a global scale. *Nature Communications*, *10:264*. https://doi.org/10.1038/s41467-018-08240-4

Box, J E, Fettweis, X., Stroeve, J. C., Tedesco, M., Hall, D. K., & Steffen, K. (2012). Greenland ice sheet albedo feedback: thermodynamics and atmospheric drivers. *The Cryosphere*, 821–839. https://doi.org/10.5194/tc-6-821-2012

Box, Jason E. (2002). Survey of Greenland Instrumental Temperature Records: 1873-2001. *International Journal of Climatology*, *22*, 1829–1847. https://doi.org/10.1002/joc.852

Chen, M., Rowland, J. C., Wilson, C. J., Altmann, G. L., & Brumby, S. P. (2014). Temporal and spatial pattern of thermokarst lake area changes at Yukon Flats, Alaska. *Hydrological Processes*, *28*(November 2012), 837–852. https://doi.org/10.1002/hyp.9642

Cooley, S. W., & Pavelsky, T. M. (2016). Spatial and temporal patterns in Arctic river ice breakup revealed by automated ice detection from MODIS imagery. *Remote Sensing of Environment*, *175*, 310–322. https://doi.org/10.1016/j.rse.2016.01.004

Eicken, H. (2010). Indigenous Knowledge and Sea Ice Science : What Can We Learn from Indigenous Ice Users ?, 357–376. https://doi.org/10.1007/978-90-481-8587-0

Ford, J D, Clark, D., Pearce, T., Copland, L., Dawson, J., New, M., & Harper, S. L. (2019). Changing access to ice, land and water in Arctic communities. *Nature Climate Change*, *9*(April). https://doi.org/10.1038/s41558-019-0435-7

Ford, James D, Smit, B., & Wandel, J. (2006). Vulnerability to climate change in the Arctic: A case study from Arctic Bay, Canada. *Global Environmental Change*, *16*, 145–160. https://doi.org/10.1016/j.gloenvcha.2005.11.007

Francis, J. A., & Vavrus, S. J. (2012). Evidence linking Arctic amplification to extreme weather in midlatitudes. *Geophysical Research Letters*, *40*(17), 4734–4739. https://doi.org/10.1002/grl.50880

Fraser, R. H., Olthof, I., & Carri, M. (2011). Detecting long-term changes to vegetation in northern Canada using the Landsat satellite image archive. *Environmental Research Letters*, *6*. https://doi.org/10.1088/1748-9326/6/4/045502

Gearheard, S., Matumeak, W., Angutikjuaq, I., Maslanik, J., Huntington, H. P., Gearheard, S., et al. (2006). “It’s Not that Simple”: A Collaborative Comparison of Sea Ice Environments, Their Uses, Observed Changes , and Adaptations in Barrow, Alaska, USA, and Clyde River, Nunavut, Canada. *AMBIO: A Journal of the Human Environment*, *35*(June).

Holgerson, M. A., & Raymond, P. A. (2016). Large contribution to inland water CO2and CH4emissions from very small ponds. *Nature Geoscience*, *9*(3), 222–226. https://doi.org/10.1038/ngeo2654

Hollesen, J., Matthiesen, H., Møller, A. B., & Elberling, B. (2015). Permafrost thawing in organic Arctic soils accelerated by ground heat production, *5*(June). https://doi.org/10.1038/NCLIMATE2590

Jones, M. C., Grosse, G., Jones, B. M., & Anthony, K. W. (2012). Peat accumulation in drained thermokarst lake basins in continuous, ice-rich permafrost , northern Seward Peninsula, Alaska. *Journal of Geophysical Research*, *117*, 1–16. https://doi.org/10.1029/2011JG001766

Kokelj, S. V., & Jorgenson, M. T. (2013). Advances in thermokarst research. *Permafrost and Periglacial Processes*, *24*(October 2012), 108–119. https://doi.org/10.1002/ppp.1779

Magnuson, J., Robertson, D., Benson, B., Wynne, R., Livingstone, D., Arai, T., et al. (2000). Historical trends in lake and river ice cover in the northern hemisphere. *Science*, *289*, 1743–6. https://doi.org/10.1126/science.289.5485.1743

Mouginot, J., Rignot, E., Bjørk, A. A., van den Broeke, M., Millan, R., Morlighem, M., et al. (2019). Forty-six years of Greenland Ice Sheet mass balance from 1972 to 2018. *Proceedings of the National Academy of Sciences*, *116*(19), 201904242. https://doi.org/10.1073/pnas.1904242116

Nitze, I., Grosse, G., Jones, B. M., Arp, C. D., Ulrich, M., Fedorov, A., & Veremeeva, A. (2017). Landsat-based trend analysis of lake dynamics across Northern Permafrost Regions. *Remote Sensing*, *9*(7), 1–28. https://doi.org/10.3390/rs9070640

Notz, D., & Stroeve, J. (2016). Observed Arctic sea-ice loss directly follows anthropogenic CO2 emission. *Science*, *354*(6313), 747–750. https://doi.org/10.1126/science.aag2345

Olthof, I., Fraser, R. H., & Schmitt, C. (2015). Landsat-based mapping of thermokarst lake dynamics on the Tuktoyaktuk Coastal Plain, Northwest Territories, Canada since 1985. *Remote Sensing of Environment*, *168*, 194–204. https://doi.org/http://dx.doi.org/10.1016/j.rse.2015.07.001

Overland, J. E., Spillane, M. C., Percival, D. B., Wang, M., & Mofjeld, H. O. (2004). Seasonal and Regional Variation of Pan-Arctic Surface Air Temperature over the Instrumental Record. *Journal of Climate*, *17*, 3263–3282.

Pekel, J.-F., Cottam, A., Gorelick, N., & Belward, A. S. (2016). High-resolution mapping of global surface water and its long-term changes. *Nature*, *540*(7633), 418–422. https://doi.org/10.1038/nature20584

Peterson, B. J., Holmes, R. M., McClelland, J. W., Vörösmarty, C. J., Lammers, R. B., Shiklomanov, A. I., et al. (2002). Increasing river discharge to the Arctic Ocean. *Science*, *298*(December), 2171–2173. https://doi.org/10.1126/science.1077445

Rawlins, M. A., Steele, M., Holland, M. M., Adam, J. C., Cherry, J. E., Francis, J. A., et al. (2010). Analysis of the Arctic system for freshwater cycle intensification: Observations and expectations. *Journal of Climate*, *23*, 5715–5737. https://doi.org/10.1175/2010JCLI3421.1

Raymond, P. A., Hartmann, J., Lauerwald, R., Sobek, S., McDonald, C., Hoover, M., et al. (2013). Global carbon dioxide emissions from inland waters. *Nature*, *503*(7476), 355–359. https://doi.org/10.1038/nature12760

Serreze, M. C., & Barry, R. G. (2011). Processes and impacts of Arctic amplification: A research synthesis. *Global and Planetary Change*, *77*(1–2), 85–96. https://doi.org/10.1016/j.gloplacha.2011.03.004

Shiklomanov, A. I., Lammers, R. B., & Vorosmarty, C. J. (2002). Widespread decline in hydrological monitoring threatens pan-Arctic research. *EOS*, *83*(2).

Smith, L. C., Sheng, Y., MacDonald, G. M., & Hinzman, L. D. (2005). Disappearing Arctic lakes. *Science*, *308*(5727), 1429. https://doi.org/10.1126/science.1108142

Stroeve, J. C., Serreze, M. C., Holland, M. M., Kay, J. E., Malanik, J., & Barrett, A. P. (2012). The Arctic's rapidly shrinking sea ice cover: a research synthesis. *Climatic Change*, *110*, 1005–1027. https://doi.org/10.1007/s10584-011-0101-1

Tedstone, A. J., Nienow, P. W., Gourmelen, N., Dehecq, A., Goldberg, D., & Hanna, E. (2015). Decadal slowdown of a land-terminating sector of the Greenland Ice Sheet despite warming. *Nature*, *526*, 692–695. https://doi.org/10.1038/nature15722

Turetsky, M. R., Abbott, B. W., Jones, M. C., Anthony, K. W., Olefeldt, D., Schuur, E. A. G., et al. (2020). Carbon release through abrupt permafrost thaw. *Nature Geoscience*, *13*(February). https://doi.org/10.1038/s41561-019-0526-0

CHAPTER 1

Coldest Canadian Arctic Communities Face Greatest Reductions in Shorefast Sea Ice

Sarah W. Cooley[1,2*], Jonathan C. Ryan[2], Laurence C. Smith[1,2], Chris Horvat[1,2], Brodie Pearson[1,3], Brigt Dale[4] and Amanda Lynch[1,2]

[1]Department of Earth, Environmental and Planetary Sciences, Brown University, 324 Brook St, Providence, Rhode Island, USA, 02912.

[2]Institute at Brown for the Environment and Society, Brown University, 85 Waterman St, Providence, Rhode Island, USA, 02912.

[3]College of Earth, Ocean, and Atmospheric Sciences, Oregon State University, 101 SW 26th St, Corvallis, Oregon, USA, 97331

[4]Nordland Research Institute, Universetetalleen 11, Bodø, Norway.

Currently in press in *Nature Climate Change*

Abstract

Shorefast sea ice comprises only ~12% of the total sea ice cover on Earth yet has outsized importance for Arctic societies and ecosystems (Eicken et al., 2009; Ford et al., 2009; Mahoney, 2018). Relatively little is known, however, about the dominant drivers of shorefast ice breakup or how it will respond to climate warming. Here, we use nineteen years of near-daily satellite imagery to document the timing of shorefast ice breakup in 28 communities in northern Canada and western Greenland that rely on shorefast ice for transportation and traditional subsistence activities. We find that breakup timing is strongly correlated with springtime air temperature, but its sensitivity varies substantially between communities. By combining these observed sensitivities with a range of future climate warming scenarios, we quantify plausible future reductions in springtime shorefast ice season by 2100, ranging from 5 to 44 days earlier each year. Paradoxically, it is the coldest communities that are projected to experience the most dramatic reductions in springtime ice season duration. Our results emphasize the local nature of physical climatic changes and the contrasting implications of climate warming for different Arctic communities.

1. Introduction

The Arctic is currently experiencing some of the fastest rates of environmental change on Earth, including reductions in sea ice extent (Notz & Stroeve, 2016), melting of glaciers and ice sheets (Mouginot et al., 2019), lengthening of the growing season (Park et al., 2016), thawing of permafrost (Biskaborn et al., 2019) and intensification of the hydrologic cycle (Rawlins et al., 2010). For Arctic coastal communities, perhaps the most impactful result of climate warming is changes to shorefast sea ice. Shorefast ice, also known as landfast sea ice or "fast" ice, is immobile sea ice frozen to the shore which forms along the Arctic coastline during winter and spring (Fig. 1.1). Shorefast ice is a stable, critically important transportation platform, connecting isolated communities and providing access to traditional hunting and fishing grounds for 3 – 9 months each year (Gearheard et al., 2006). The presence of shorefast ice also mitigates coastal erosion which threatens many Arctic communities located along subsiding coastal margins (Overeem et al., 2011). Shorefast ice is a critical habitat for marine mammals such as seals and polar bears (Laidre et al., 2008), and polynyas that form seaward of shorefast ice edges create hotspots of high ecological productivity (Mundy et al., 2009). Shorefast ice, rather than drift ice, therefore provides most of the "sea ice services" (Eicken et al., 2009) utilized by Arctic communities.

Since the early 2000s, residents of many Arctic communities have reported that shorefast ice is thinner, freezes up later and breaks up earlier than in the 1990s (Baztan et al., 2017; Gearheard et al., 2006; Laidler et al., 2009; Meier et al., 2006). These changes increase travel risk, reduce hunting success and threaten traditional activities (Laidler et al., 2009; Meier et al., 2006; Pearce et al., 2010), further exacerbating insecurity in communities already experiencing socioeconomic and cultural stress (Baztan et al., 2017; Ford et al., 2009). Despite its critical socioeconomic importance and reports of its decline, shorefast ice is challenging to observe and model and therefore has remained understudied. Shorefast ice is poorly resolved by coarse resolution (~25 km) passive microwave sensors typically used to map sea ice extent, because it forms within narrow fjords and along complex coastlines. The few studies that have analyzed fine-scale changes in shorefast ice have primarily focused on Northern Alaska, notably along the coastline near Utqiagvik (Mahoney et al., 2007; Mahoney et al., 2014; Petrich et al., 2012), while longer term changes have relied on coarse resolution models and/or observations (Galley et al., 2012; Howell et al., 2016). Long-term changes in shorefast ice and controls on its decline therefore remain largely unknown, especially at the community scale outside of Alaska.

Here, we document the timing of shorefast ice breakup from 2000 to 2018 for 28 coastal Arctic communities using daily cloud-filtered satellite imagery acquired by NASA's Moderate Resolution Imaging Spectroradiometer (MODIS). The communities are located in Nunavut and the Northwest Territories (N.W.T.), Canada, and in Western Greenland (Fig. 1.2). All have strong cultural, economic, and environmental ties to shorefast ice. We compare our remotely sensed observations to surface air temperature records measured by automated weather stations (AWS) and atmospheric reanalysis (ERA-Interim) and find a strong atmospheric control on the timing of shorefast ice breakup. The strength of these correlations allows us to empirically assess the environmental sensitivity of individual communities to atmospheric warming. We then use global climate model simulations to project which communities may experience the greatest changes in shorefast ice by 2100. Our place-based approach allows us to determine how climate change will affect human settlements with important cultural heritage in the Arctic.

2. Methods

2.1 Satellite Imagery

Shorefast ice was mapped using the atmospherically corrected MODIS Level 2 product, MOD09GQ, a daily product with a ground sampling resolution of 250 m (Figure S1.2) created from the Moderate Resolution Imaging Spectrometer aboard NASA's Terra satellite (Vermote & Wolfe, 2015). The high temporal and spatial resolution of MOD09GQ allowed us to distinguish shorefast ice in narrow Arctic fjords with sufficiently fine resolution to resolve the timing of breakup accurately. Clouds and cloud shadows were masked using the cloud mask from coincident MOD09GA products which were resampled (nearest neighbors) from 1000 m to 250 m pixel resolution to match the MOD09GQ products. We analyzed all daily imagery collected between day of year 60 and 240 (March 1 to August 28) over 2000-2018.

2.2 Breakup Detection

Our classification and breakup detection method builds off the river ice breakup detection method presented in Cooley and Pavelsky (2016). First, we created a land/ocean mask using high resolution coastline shapefiles from Statistics Canada (https://open.canada.ca/data/en/dataset/a883eb14-0c0e-45c4-b8c4-b54c4a819edb) and GADM (https://gadm.org/index.html) which were combined with the resampled MOD09GA cloud masks to exclude all land and cloudy pixels in the MOD09GQ images. Each MODIS band 2 (841 – 876 nm) image was then classified into snow, ice and water using simple thresholds in band 2 reflectance (< 0.1 = water, 0.1 – 0.5 = ice and > 0.5 = snow; note reflectance is MOD09GQ digital number multiplied by 0.001). Next, we applied a 5 x 5 km grid covering the fjord and/or coastal ocean within ~20 km of each community to each image and determined the percentage of cloud-free MODIS pixels that were classified as snow, water and ice for each grid cell. This produced a daily time series of snow, ice and water percent for each grid cell from March to August for every year between 2000 and 2018 (Figure S1.3).

Using these time series, we determined the annual date of breakup for each 5 x 5 km grid cell. First, all days with >50% cloud cover were removed and Hampel and 5-day median filters were applied to the time series to remove outliers caused by sensor noise or failure of the MODIS cloud mask. Only grid cells which had a snow or ice value > 90% for at least 3 consecutive cloud-free observations in each year were analyzed to ensure that shorefast ice was present. Breakup date detection proceeded for each time series as follows:

(1) We identified the first five-observation period when the grid cell averaged at least 50% open water.
(2) We determined the first day within or following this five-observation period when the grid cell reached 90% open water.
(3) To account for cloud cover, the breakup date was then defined as the midpoint between this date and the previous cloud-free observation, with the uncertainty in breakup detection the difference between the two (Cooley & Pavelsky, 2016) (Figure S1.3).

This process was repeated for all grid cells within 20 km of the community for all years which yielded a mean uncertainty in breakup timing due to cloud obscuration of $\pm$ 1.9 days. We defined the breakup date for each individual community for each year as the mean breakup timing in these grid cells. Breakup dates were allowed to be fractional during the temperature analysis, but for simplicity were rounded to the nearest day in the table and in the text. While we acknowledge that community use of shorefast ice generally ceases before the fjord is 90% open water, we chose this breakup threshold because it is a consistent metric that is interpretable to both scientists and local community members as the point in which the area surrounding each community becomes clear of ice. To mitigate possible influence of drift ice on breakup detection, grid cells which on average do not transition from >90% ice to >90% water each spring/summer were removed from the analysis, as in our manual examination of the imagery, grid cells in our study area containing substantial drift ice tended to have this characteristic. We note that this method does not explicitly distinguish between drift ice and shorefast ice. While this distinction is not required along the complex coastlines and fjords of the Canadian Arctic Archipelago and Western Greenland where nearly all sea ice is landlocked, we caution the use of this approach in regions of the Arctic where shorefast ice is less extensive, such as along the Bering and Chukchi coasts in Alaska.

We assessed the accuracy of this method first through sensitivity analysis of the water thresholds. Water reflectance thresholds of 0.08, 0.09, 0.10 (chosen threshold), 0.11 and 0.12 were tested for three communities over the full MODIS record. Changes to the threshold had comparatively small impacts on breakup timing, shifting breakup by only 0-4 days on average (Figure S1.4), and had little-to-no impact on correlations with air temperature. Therefore, although the choice of water threshold may slightly shift the exact date of breakup, it is unlikely to affect any of our conclusions.

We also assessed the accuracy of this method by comparison to high resolution Planet and Sentinel-2 imagery. We compared the breakup dates for each community in 2017 and 2018 with breakup dates manually detected using high resolution, near-daily Planet Labs and Sentinel-2 satellite imagery. This comparison was imperfect, as there are biases associated with manual detection and furthermore cloud cover and missing imagery can impact results when comparing between sensors. However, it was a useful external check on the breakup dates to ensure accuracy of the method. For both 2017 and 2018, manually and automatically detected breakup dates were strongly correlated with an $R^2 > 0.93$. The RMSE between manually and automatically detected dates was 4.3 days in 2017 and 4.2 days for 2018, and the median difference between the dates was 1.8 days for 2017 and 3.4 days for 2018, suggesting confidence in our breakup detection method (Figure S1.5).

2.3 Temperature Analyses

To assess the relationship between breakup timing and springtime air temperature we used both automated weather station (AWS) data from each community and the ERA-Interim reanalysis product (Dee et al., 2011). For Canadian communities, hourly AWS data were obtained from the Government of Canada Historical Weather Data (http://climate.weather.gc.ca/). For Greenlandic communities, hourly AWS data were obtained from Danish Meteorological Institute (https://www.dmi.dk/publikationer/). All hourly data were averaged to a daily mean, and to avoid bias caused by diurnal temperature variability, days with less than 22 hours of data were excluded. To produce the yearly springtime air temperature records, we averaged between stations if multiple stations were available and interpolated between days if data was missing. Years where more than 4 days of spring air temperature were missing were excluded to limit the effect this bias could have on reported results. Overall, 23 of 28 communities had AWS data meeting these standards for >10 years over 2000-2018.

We also used ERA-Interim reanalysis data (Dee et al., 2011) as it provides a consistent record available over all 28 communities between 2000-2018 (https://www.ecmwf.int/en/forecasts/datasets/reanalysis-datasets/era-interim) and has been shown to perform well over the Arctic(Lindsay et al., 2014). To produce the springtime air temperature time series, six-hourly temperature values from the nearest four ERA-Interim grid cells to each community were averaged into a daily time series.

For both AWS and ERA-Interim datasets, we calculated the mean air temperatures (in °C) for each community over a set period in the spring:

Eq. (1) $$T_s = \sum_{EoS\,-\,40}^{EoS\,-\,5} T_d\ (°C)\ /36$$

Where T_s = mean springtime air temperature (in °C), EoS = end of spring and T_d = daily air temperature (in °C). We defined the "end of spring" as the earliest date of breakup for each community which ensured that our calculation of springtime air temperature encompassed the period prior to breakup for each community given the wide range in breakup timing. To determine the length of the period prior to the "end of spring" which best predicts breakup timing, we optimized for maximum average R^2 over all communities and tested between 15 and 75 days prior to the earliest breakup. We excluded the five days prior to the end of spring to ensure that the mean springtime temperature was calculated only over days with near complete ice cover, thus mitigating any potential effect of a positive feedback between open-water and air temperature (Mahoney et al., 2007). This analysis yielded 40 days prior to the end of spring as the optimal period over which to calculate degree days, though changing the number of days prior to the end of breakup from 35 to 45 days has little impact on correlations with air temperature.

To estimate future changes in breakup, we used daily 2 m temperature outputs from eight CMIP5 global climate models, namely BNU-ESM, CCSM4, CESM1-CAM5, CSIRO-Mk3-6-0, GFDL-CM3, IPSL-CM5A-LR, NorESM1 and BCC-CSM1 (Taylor et al., 2012). These eight model runs were chosen as they all provide daily 2 m air temperature data over 2006-2099 under RCP2.6 (low emission), RCP4.5 (midrange mitigation) and RCP8.5 (high emissions) scenarios. The yearly springtime degree day time series were produced by averaging the daily temperature time series for all grid cells located within a 2° x 2° box surrounding each community and calculating springtime degree days as described above. We chose this sampling strategy due to inconsistencies in CMIP5 model resolutions. Next, all 94-year modeled springtime degree day time series were normalized to their 2006-2018 average, and a 10-year median filter was applied. We then calculated projected future changes in breakup timing by applying the air temperature sensitivities, calculated using ERA-Interim and normalized to 2006-2018, to the future springtime degree day time series.

3. Results

Our satellite remote sensing analysis of shorefast ice breakup, defined as the first day when the 20 km surrounding each community reaches >90% open water, provides a consistent 19-year breakup record for all 28 communities in Figure 1.2 with an average uncertainty due to cloud cover of ± 1.9 days. We find substantial variability in breakup timing across the study region, with colder communities, as defined by mean annual air temperature (MAAT), experiencing later breakup than warmer communities ($R^2 = 0.50$, $p < 0.001$). From 2000 to 2018, mean breakup timing ranged from May 29 (standard deviation = ± 17 days) in Uummannaq to August 1 (± 10 days) in Grise Fiord, with an average date of July 11 (± 15 days) across all communities. Regionally, shorefast ice cleared first in the Western Northwest Passage (June 30, ± 8 days) and remained the longest in the Central Northwest Passage (July 24, ± 6 days) and Northern Baffin Bay (July 23, ± 7 days). On average, breakup varied by 34 days in each community over the 19-year period, ranging from a minimum of 16 days in Tuktoyaktuk to a maximum of 76 days in Ulukhaktok (Table S1.1). Importantly, this interannual variability in shorefast ice breakup timing is not necessarily associated with drift ice extent, with the correlation between shorefast breakup timing and regional drift ice extent (Fetterer et al., 2019) positively significant for just 9 of 28 communities over the study period (see Supplementary Information).

Much of the interannual variability in shorefast ice breakup is associated with local fluctuations in springtime air temperature (Fig. 1.3), here defined as the mean daily 2 m air temperature during a 36-day spring period defined by the earliest date of observed shorefast ice breakup in each fjord. Of 23 communities having at least 10 years of in situ AWS data, 18 exhibit a significant correlation between AWS springtime air temperature and breakup at 95% confidence (mean $R^2 = 0.56$) (Fig. S1.1, Table S1.1). Similarly, 25 of 28 communities exhibit a significant correlation at 95% confidence (mean $R^2 = 0.49$) (Fig. 1.3; Table S1.1) when compared with 2 m air temperature from ERA-Interim reanalysis (Dee et al., 2011). We hypothesize the absence of the relationship in the other three communities is due to persistent year-round open water near the community in Cape Dorset and a potential influence of drift ice on shorefast ice breakup detection in Ulukhaktok and Resolute. We also note that while air temperature appears to be the dominant control on breakup timing, some of the uncertainty in the correlations may be explained by winds and ocean temperatures.

While nearly all of the communities studied here exhibit strong empirical correlations between springtime air temperature and breakup, the sensitivity of the relationship (i.e. the slope of linear regression; Fig. 1.3) is highly variable between communities. Most sensitive is Grise Fiord, at -7.5 days/°C, and least sensitive is Tuktoyaktuk at -1.1 days/°C (Table S1.1). Regional patterns in sensitivity are also evident, with the Northern Baffin Bay region experiencing -6.1 days/°C and Western Northwest Passage just -2.5 days/°C (Fig. 1.4). We find that breakup in colder communities is more sensitive to climate fluctuations than in warmer communities ($R^2 = 0.30$, $p < 0.01$; Fig. 1.4). This observed relationship between MAAT and sensitivity strengthens even further if the two warmest communities (Uummannaq and Sanikiluaq) are excluded ($R^2 = 0.59$, $p < 0.001$; Fig. 1.4a).

By applying our observed empirical correlations between springtime air temperature and shorefast ice breakup to a range of projected future air temperatures from CMIP5 global climate model simulations (Taylor et al., 2012), we find a correspondingly wide range of projected declines in breakup timing. Under a high emissions scenario (RCP8.5), we find that by 2099, changes in breakup timing range from 5 days earlier (Tuktoyaktuk) to 44 days earlier (Taloyoak), with an average change of 20 ($\pm$ 9) days earlier across all communities (Table S1.1). Regionally, the Central Northwest Passage is projected to experience the largest reduction in spring shorefast ice season (-31 days) and Western Northwest Passage the smallest (-12 days) (Figs. 1.4 and 1.5). These overall geographical patterns are preserved under the RCP4.5 (-9 days on average) and RCP2.6 (-7 days) scenarios (Fig. 1.5). As with breakup sensitivity, there is a linear correlation between MAAT and predicted future change in breakup ($R^2 = 0.24$, $p = 0.01$), suggesting that colder communities will experience greater reductions in springtime shorefast ice than warmer communities (Fig. 1.4c). Similarly, the relationship between MAAT and predicted future change is stronger when the two warmest communities are excluded ($R^2 = 0.36$, $p < 0.01$; Fig. 1.4c).

4. Discussion and Conclusions

This study presents the first community-level assessment of shorefast ice breakup across Northern Canada and West Greenland, thus providing insight into an understudied process that critically affects the livelihoods, cultures, and economies of coastal Arctic communities. Our analysis identifies large sub-regional variability in both the present-day timing of shorefast ice breakup and its sensitivity to future warming. While future work is needed to determine whether these findings are broadly applicable outside of the Canadian Arctic Archipelago, a clear northward trend in sensitivity is especially notable and underscores the necessity of localized approaches for assessing environmental sensitivity to Arctic climate change.

The strong positive correlations between breakup timing and springtime air temperatures over the period 2000-2018 suggest that surface-atmosphere interactions exert a first-order control on shorefast ice breakup. While few studies have specifically examined the relationship between breakup and springtime air temperature, the strong role of atmospheric interactions helps to corroborate recent work finding surface air temperature to be the dominant control on both drift ice extent (Olonscheck et al., 2019) and outlet glacier termini positions (Cook et al., 2019) in our study region. Although we find no statistically significant trends in air temperature or breakup timing in any community during our 19-year record, Arctic air temperatures are projected to rapidly increase in the future (Pithan & Mauritsen, 2014). The strongly positive correlation between springtime air temperatures and shorefast ice breakup identified here therefore suggests that breakup will occur earlier in the future, highlighting the potential exposure of coastal Arctic communities to anthropogenically-induced climate warming.

While all communities are likely to experience earlier shorefast ice breakup in the future, breakup in colder communities is notably more sensitive to changes in springtime air temperature than in warmer communities (Fig. 1.4). This regional variability in breakup sensitivity holds contrasting implications for communities in Northern Canada and Western Greenland, particularly when socioeconomic and cultural differences are also considered. For example, communities that are most reliant on traditional subsistence activities, such as Clyde River and Taloyoak (-6.5 and -6.9 days/°C, respectively), are especially vulnerable to earlier ice breakup. Breakup in these two communities is expected to occur 23 to 44 days earlier, respectively, by 2099, suggesting that economically and culturally significant activities on the ice will be harder to maintain in the future (Gearheard et al., 2006). Communities located along increasingly popular Arctic cruise ship routes, such as Cambridge Bay (-4.8 days/°C, -29 days in 2099) and Pond Inlet (-5.6 days/°C, -23 days in 2099), however, may experience some benefits from earlier ice breakup. Our prediction of a substantially reduced shorefast ice season in these communities has the potential to enhance economic development through increased ship port-of-calls, alongside negative environmental and cultural impacts from rising numbers of cruise ships (Stewart et al., 2007).

In contrast to these examples, communities such as Tuktoyaktuk (-1.1 days/°C, -5 days in 2099) and Paulatuk (-2.3 days/°C, -11 days in 2099) are projected to be less affected by shorefast ice reductions. Due to its low climatic sensitivity and high potential for coastal economic development due to its new year-round connection to the North American road network (Bennett, 2018), Tuktoyaktuk, in particular, may be less vulnerable to the cultural and economic changes caused by climate warming than other communities assessed here. These nuances emphasize the importance of taking a community-based approach to climate studies and recognizing that even within the rapidly changing Arctic, climate change does not affect all communities equally.

The results and projections presented here provide useful insight into varying spatial patterns of Arctic climate change and the exposure of coastal communities to environmental change. However, other factors beyond air temperature (e.g. winds, ocean temperatures and surface waves) also likely influence shorefast ice breakup timing. Similarly, breakup timing is just one of several shorefast ice metrics that affect community ice usage. Future work should thus consider incorporating additional environmental variables, together with shorefast ice thickness (Dumas et al., 2006), stability (Dammann et al., 2019), and freeze-up date (Yu et al., 2014). Such analysis may elucidate the mechanisms controlling breakup and how they differ between warmer and colder communities, therefore lending further confidence to our projections. Additional human and/or geographic factors unrelated to climate change may also influence community vulnerability to reductions in shorefast ice. For example, the two warmest communities, Uummannaq, and to a lesser extent Sanikiluaq, already experience much earlier breakup than other communities (May 29th and June 21st on average, respectively) and a shorter ice season. Therefore, the sociocultural impact of even comparatively small changes in breakup timing could be severe. This is exemplified by the 2005 winter in Uummannaq when stable shorefast sea ice never formed, meaning that locals could not access the ice and many dog teams were unused for nearly two years. In a warmer climate, such occurrences may become more frequent and lead to the loss of traditional cultural activities such as dog sledding and seal hunting on the ice (Baztan et al., 2017).

Overall, our study of shorefast sea ice applies broad-scale remote sensing and climate modeling tools at a community-level to identify complexity at the sub-regional scale. The observed variability in shorefast sea ice appears to be localized and not necessarily correlated with pan-Arctic drift ice records, corroborating previous reports by both local residents (Baztan et al., 2017) and scientists (Mahoney et al., 2014). The high susceptibility of the coldest, northernmost communities of Northern Canada and Western Greenland to reduced shorefast ice seasons emphasizes the importance of considering the local nature of climatic changes alongside community-level differences when making policy decisions or other preparations for the consequences of climate change. Because shorefast ice is one of many environmental assets important to Arctic communities, future research combining broad-scale analysis tools with community-level characteristics may help provide more actionable information for Arctic populations facing substantial climatic and social change.

Acknowledgments

This research was funded by a NSF Navigating the New Arctic Grant, #1836473. S.C. acknowledges funding from an NSF Graduate Research Fellowship and from a Geological Society of America Student Research Grant. We gratefully acknowledge Ann Andreasen, the Uummannaq Polar Institute and Uummannaq Childrens Home for providing lodging and fieldwork support. We thank Paaluk Kreutzmann and Malik Johansen for sharing their knowledge and their assistance in the field. We acknowledge the World Climate Research Programme's Working Group on Coupled Modeling, which is responsible for CMIP, and we thank the climate modeling groups listed in the

Methods for producing and making available their model output. We thank three anonymous reviewers for their very thoughtful and helpful feedback on earlier versions of this manuscript.

References

Baztan, J., Cordier, M., Huctin, J., & Zhu, Z. (2017). Life on thin ice: Insights from Uummannaq, Greenland for connecting climate science with Arctic communities. *Polar Science*, *13*, 100–108. https://doi.org/10.1016/j.polar.2017.05.002

Bennett, M. M. (2018). From state-initiated to Indigenous-driven infrastructure: The Inuvialuit and Canada's first highway to the Arctic Ocean. *World Development*, *109*, 134–148. https://doi.org/10.1016/j.worlddev.2018.04.003

Biskaborn, B. K., Smith, S. L., Noetzli, J., Matthes, H., Vieira, G., & Streletskiy, D. A. (2019). Permafrost is warming at a global scale. *Nature Communications*, *10*. https://doi.org/10.1038/s41467-018-08240-4

Cook, A. J., Copland, L., Noël, B. P. Y., Stokes, C. R., Bentley, M. J., Sharp, M. J., et al. (2019). Atmospheric forcing of rapid marine-terminating glacier retreat in the Canadian Arctic Archipelago. *Science Advances*, (March), 1–11.

Cooley, S. W., & Pavelsky, T. M. (2016). Spatial and temporal patterns in Arctic river ice breakup revealed by automated ice detection from MODIS imagery. *Remote Sensing of Environment*, *175*, 310–322. https://doi.org/10.1016/j.rse.2016.01.004

Dammann, D. O., Eriksson, L. E. B., Mahoney, A. R., Eicken, H., & Meyer, F. J. (2019). Mapping pan-Arctic landfast sea ice stability using Sentinel-1 interferometry. *The Cryosphere*, 557–577.

Dee, D. P., Uppala, S. M., Simmons, A. J., Berrisford, P., Poli, P., Kobayashi, S., et al. (2011). The ERA-Interim reanalysis: configuration and performance of the data assimilation system. *Quarterly Journal of the Royal Meteorological Society*, *137*(April), 553–597. https://doi.org/10.1002/qj.828

Dumas, J. A., Flato, G. M., & Brown, R. D. (2006). Future Projections of Landfast Ice Thickness and Duration in the Canadian Arctic. *Journal of Climate*, 5175–5189.

Eicken, H., Lovecraft, A. L., & Druckenmiller, M. L. (2009). Sea-Ice System Services: A Framework to Help Identify and Meet Information Needs Relevant for Arctic Observing Networks. *Arctic*, *62*(2), 119–136.

Fetterer, F., Knowles, K., Meier, W. H., Savoie, M., & Windnagel, A. K. (2019). Sea Ice Index, Version 3. Boulder, Colorado, USA: NSIDC: National Snow and Ice Data Center. https://doi.org/https://doi.org/10.7265/N5K072F8.

Ford, J. D., Gough, W. A., Laidler, G. J., Macdonald, J., Irngaut, C., & Qrunnut, K. (2009). Sea ice, climate change , and community vulnerability in northern Foxe Basin , Canada. *Climate Research*, *38*(February), 137–154. https://doi.org/10.3354/cr00777

Galley, R. J., Else, B. G. T., Howell, S. E. L., Lukovich, J. V, & Barber, D. G. (2012). Landfast Sea Ice Conditions in the Canadian Arctic : 1983-2009. *Arctic*, *65*(2), 133–144.

Gearheard, S., Matumeak, W., Angutikjuaq, I., Maslanik, J., Huntington, H. P., Gearheard, S., et al. (2006). “It’s Not that Simple”: A Collaborative Comparison of Sea Ice Environments, Their Uses, Observed Changes , and Adaptations in Barrow, Alaska, USA, and Clyde River, Nunavut, Canada. *AMBIO: A Journal of the Human Environment*, *35*(June).

Howell, S. E. L., Laliberté, F., Kwok, R., Derksen, C., & King, J. (2016). Landfast ice thickness in the Canadian Arctic Archipelago from observations and models, 1463–1475. https://doi.org/10.5194/tc-10-1463-2016

Laidler, G. J., Ford, J. D., Gough, W. A., Ikummaq, T., Gagnon, A. S., Kowal, S., et al. (2009). Travelling and hunting in a changing Arctic: assessing Inuit vulnerability to sea ice change in Igloolik, Nunavut. *Climatic Change*, 363–397. https://doi.org/10.1007/s10584-008-9512-z

Laidre, K. L., Stirling, I., Lowry, L., Wiig, O., Heide-Jorgensen, M. P., & Ferguson, S. H. (2008). Quantifying the sensitivity of Arctic marine mammals to climate-induced habitat change. *Ecological Applications*, *18*(2), 97–125.

Lindsay, R., Wensnahan, M., Schweiger, A., & Zhang, J. (2014). Evaluation of seven different atmospheric reanalysis products in the arctic. *Journal of Climate*, *27*(7), 2588–2606. https://doi.org/10.1175/JCLI-D-13-00014.1

Mahoney, A., Eicken, H., Gaylord, A. G., & Shapiro, L. (2007). Alaska landfast sea ice : Links with bathymetry and atmospheric circulation. *Journal of Geophysical Research*, *112*(July 2006). https://doi.org/10.1029/2006JC003559

Mahoney, A. R. (2018). Landfast Sea Ice in a Changing Arctic. In E. Osborne, J. A. Richter-Menge, & M. O. Jeffries (Eds.), *Arctic Report Card 2018*.

Mahoney, A. R., Eicken, H., Gaylord, A. G., & Gens, R. (2014). Landfast sea ice extent in the Chukchi and Beaufort Seas: The annual cycle and decadal variability. *Cold Regions Science and Technology*. https://doi.org/10.1016/j.coldregions.2014.03.003

Meier, W. N., Stroeve, J., & Gearheard, S. (2006). Bridging perspectives from remote sensing and Inuit communities on changing sea-ice cover in the Baffin Bay region. *Annals of Glaciology*, 433–438.

Mouginot, J., Rignot, E., Bjørk, A. A., van den Broeke, M., Millan, R., Morlighem, M., et al. (2019). Forty-six years of Greenland Ice Sheet mass balance from 1972 to 2018. *Proceedings of the National Academy of Sciences*, *116*(19), 201904242. https://doi.org/10.1073/pnas.1904242116

Mundy, C. J., Gosselin, M., Ehn, J., Gratton, Y., Rossnagel, A., Palmer, M., et al. (2009). Contribution of under-ice primary production to an ice-edge upwelling phytoplankton bloom in the Canadian Beaufort Sea, *36*, 1–5. https://doi.org/10.1029/2009GL038837

Notz, D., & Stroeve, J. (2016). Observed Arctic sea-ice loss directly follows anthropogenic CO2 emission. *Science*, *354*(6313), 747–750. https://doi.org/10.1126/science.aag2345

Olonscheck, D., Mauritsen, T., & Notz, D. (2019). Arctic sea-ice variability is primarily driven by atmospheric temperature fluctuations. *Nature Geoscience*. https://doi.org/10.1038/s41561-019-0363-1

Overeem, I., Anderson, R. S., Wobus, C. W., Clow, G. D., Urban, F. E., & Matell, N. (2011). Sea ice loss enhances wave action at the Arctic coast, *38*(June), 1–6. https://doi.org/10.1029/2011GL048681

Park, T., Ganguly, S., Tømmervik, H., Euskirchen, E. S., & Høgda, K. (2016). Changes in growing season duration and productivity of northern vegetation inferred from long-term remote sensing data. *Environmental Research Letters*, *11*.

Pearce, T., Smit, B., & Ford, J. D. (2010). Inuit vulnerability and adaptive capacity to climate change in Ulukhaktok , Northwest Territories, Canada. *Polar Record*, *46*(237), 157–177. https://doi.org/10.1017/S0032247409008602

Petrich, C., Eicken, H., Zhang, J., Krieger, J., Fukamachi, Y., & Ohshima, K. I. (2012). Coastal landfast sea ice decay and breakup in northern Alaska : Key processes and seasonal prediction. *Journal of Geophysical Research*, *117*, 1–19. https://doi.org/10.1029/2011JC007339

Pithan, F., & Mauritsen, T. (2014). Arctic amplification dominated by temperature feedbacks in contemporary climate models. *Nature Geoscience*, *7*(3), 181–184. https://doi.org/10.1038/ngeo2071

Rawlins, M. A., Steele, M., Holland, M. M., Adam, J. C., Cherry, J. E., Francis, J. A., et al. (2010). Analysis of the Arctic system for freshwater cycle intensification: Observations and expectations. *Journal of Climate*, *23*, 5715–5737. https://doi.org/10.1175/2010JCLI3421.1

Stewart, E. J., Howell, S. E. L., Draper, D., Yackel, J., & Tivy, A. (2007). Sea Ice in Canada's Arctic: Implications for Cruise Tourism. *Arctic*, *60*(4), 370–380.

Taylor, K. E., Stouffer, R. J., & Meehl, G. A. (2012). An overview of CMIP5 and the experiment design. *Bulletin of the American Meteorological Society*, *93*(4), 485–498. https://doi.org/10.1175/BAMS-D-11-00094.1

Vermote, E. F., & Wolfe, R. (2015). MOD09GQ MODIS/Terra Surface Reflectance Daily L2G Grlobal 250m SIN Grid V006.

Yu, Y., Stern, H., Fowler, C., Fetterer, F., & Maslanik, J. (2014). Interannual Variability of Arctic Landfast Ice between 1976 and 2007. *Journal of Climate*, 227–243. https://doi.org/10.1175/JCLI-D-13-00178.1

Figures

Figure 1.1. Images of shorefast sea ice: (a) seal hunter returning home by dogsled to Uummannaq, Greenland in April 2019; (b) shorefast ice edge roughly 15 km from Uummannaq in May 2019, 10 days before MODIS-detected breakup; (c) snowmobile travel on shorefast sea ice outside Iqaluit, Nunavut in March 2018; (d) small boat awaiting shorefast ice breakup near Iqaluit, Nunavut in March 2018 (all photos by lead author).

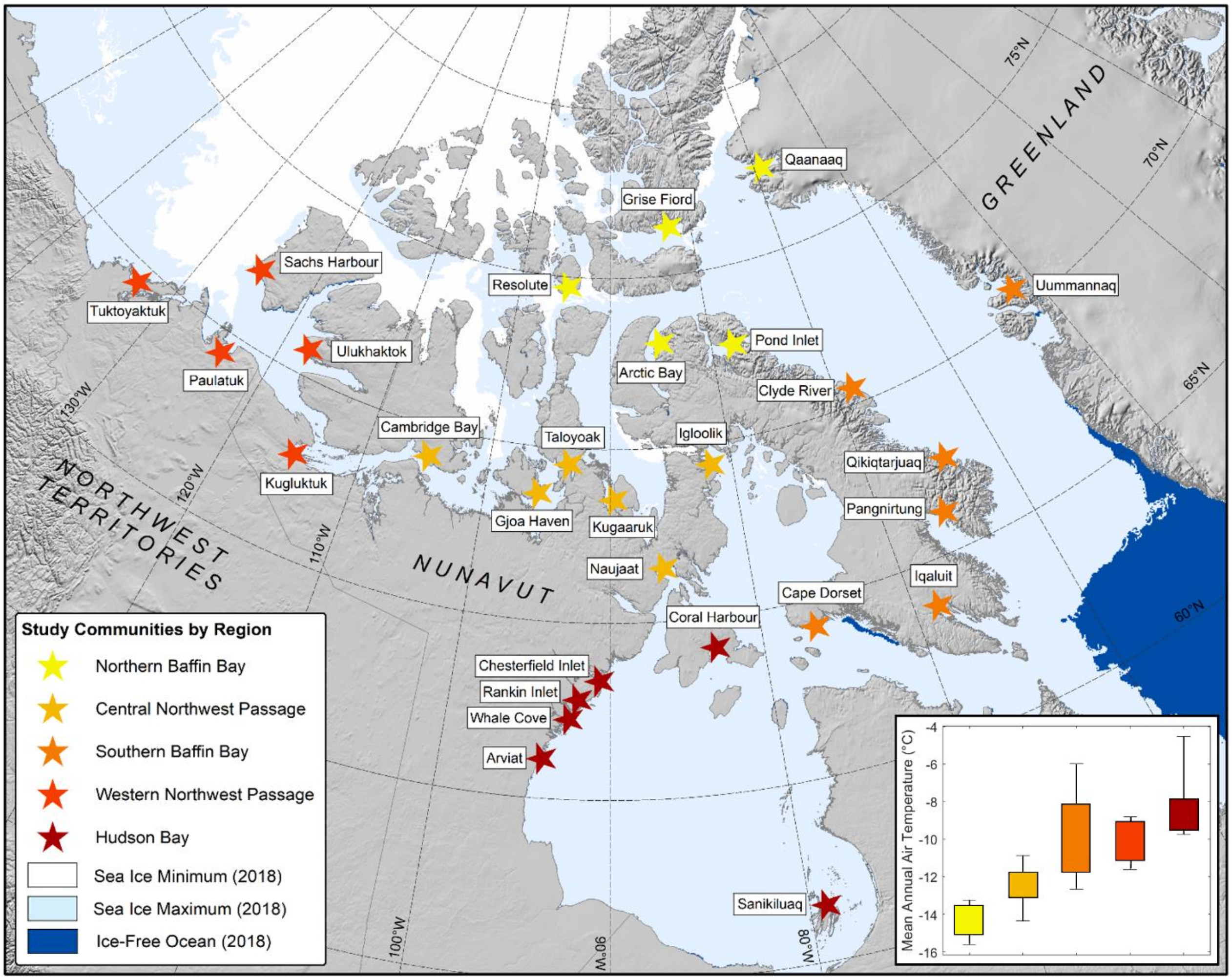

Figure 1.2. Study area map including 28 settlement communities impacted by shorefast sea ice in Nunavut and the Northwest Territories (N.W.T.), Canada, and in western Greenland. Communities are labeled and colored by subregion. Within the ocean, white illustrates the 2018 drift and shorefast ice minimum, light blue drift and shorefast sea ice maximum and dark blue perennially open ocean in 2018 as observed by NSIDC MASIE (https://nsidc.org/data/masie). Inset shows a box plot of mean annual air temperature (MAAT) over 2000-2018 for each community sub-region, where box limits represent the upper and lower quartiles and whiskers illustrate the full data range.

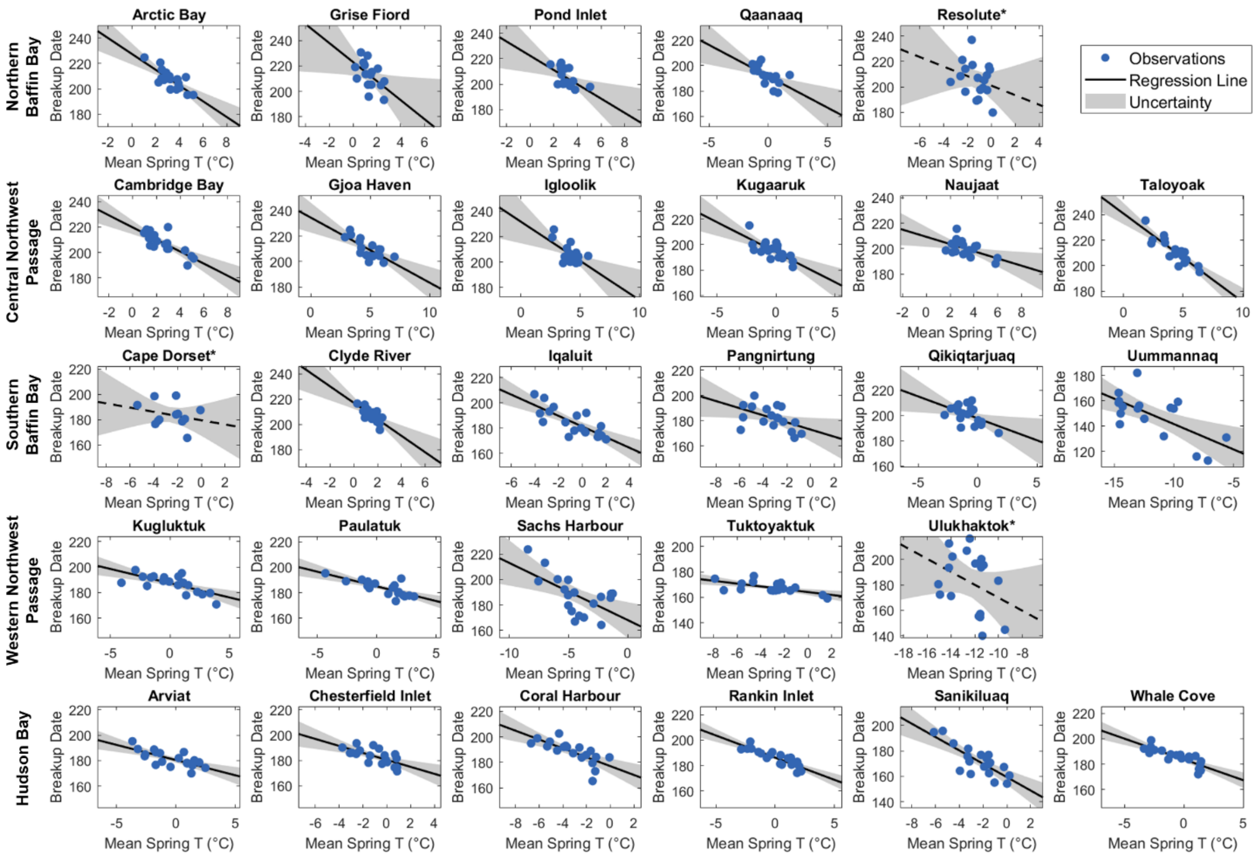

Figure 1.3. Scatter plots of shorefast ice breakup timing vs. mean springtime air temperature (°C) for all 28 communities as calculated using ERA-Interim data. Each row shows communities from the same sub-region as defined in Figure 1. Black lines show the linear regressions between shorefast ice breakup timing and springtime air temperature, with gray shading indicating the uncertainty in this regression calculated as the 95th confidence interval. A dashed line and a single asterisk after community name indicates communities where breakup timing and degree days are uncorrelated at $p < 0.05$. The x and y-axes are standardized by range to illustrate the variability in slope.

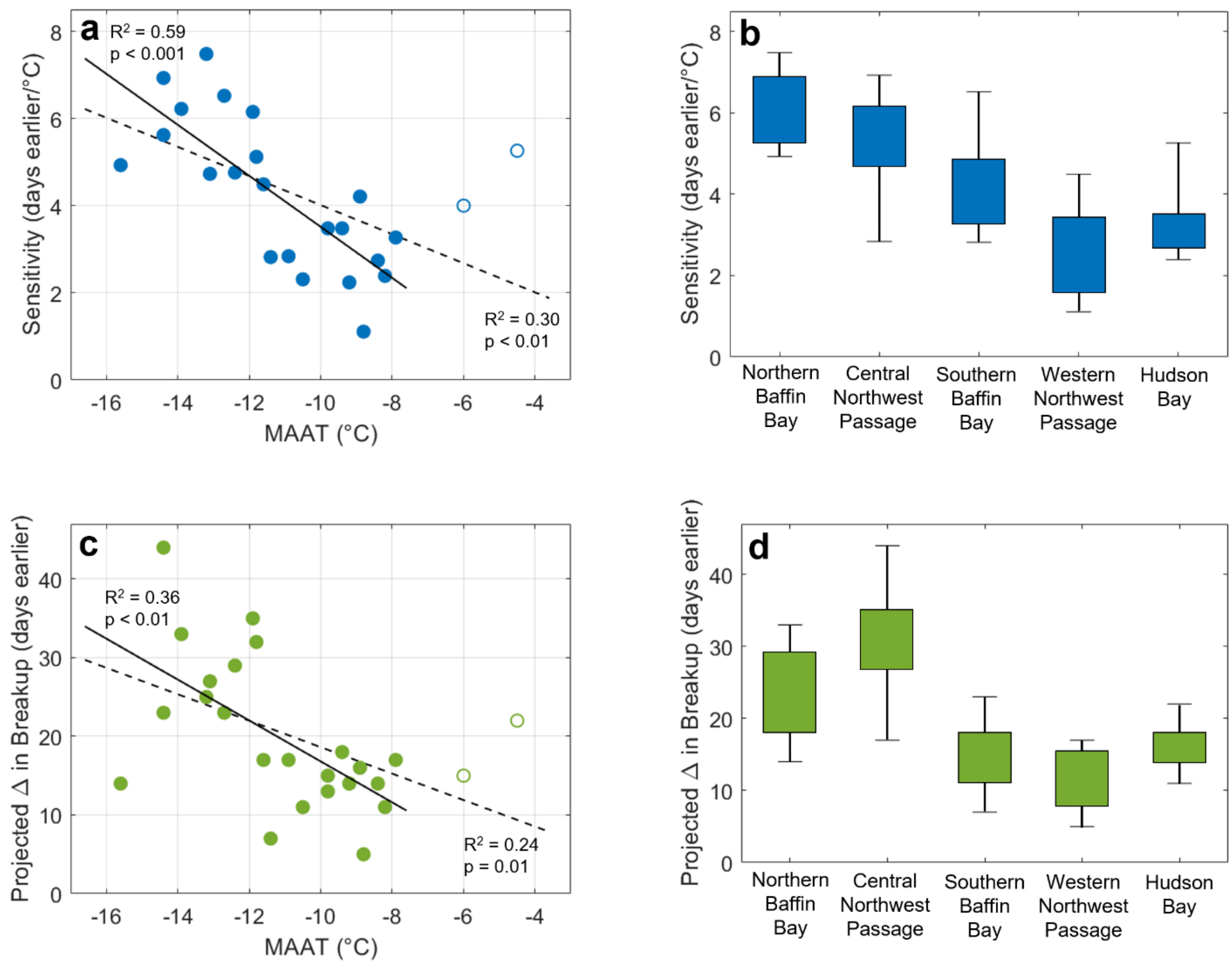

Figure 1.4. Patterns in breakup sensitivity and projected change in breakup by temperature and region. Panel (a) shows the relationship between mean annual air temperature (MAAT, °C) and shorefast ice breakup sensitivity (days earlier/°C), illustrating how colder communities are more sensitive to springtime air temperature than warmer communities. Panel (b) plots breakup sensitivity by sub-region, ordered left to right from coldest to warmest. Panel (c) shows the relationship between MAAT and projected change in breakup in 2099 (days earlier), further illustrating that colder communities are likely to experience greater changes than warmer communities. Panel (d) plots projected change in breakup in 2099 by sub-region. For (a) and (c), dashed lines show the relationship for all 28 communities, and solid lines show the relationship excluding Uummannaq and Sanikiluaq (the two warmest communities, shown as open circles on both plots). For panels (b) and (d), box limits represent the upper and lower quartiles and the whiskers illustrate the full data range.

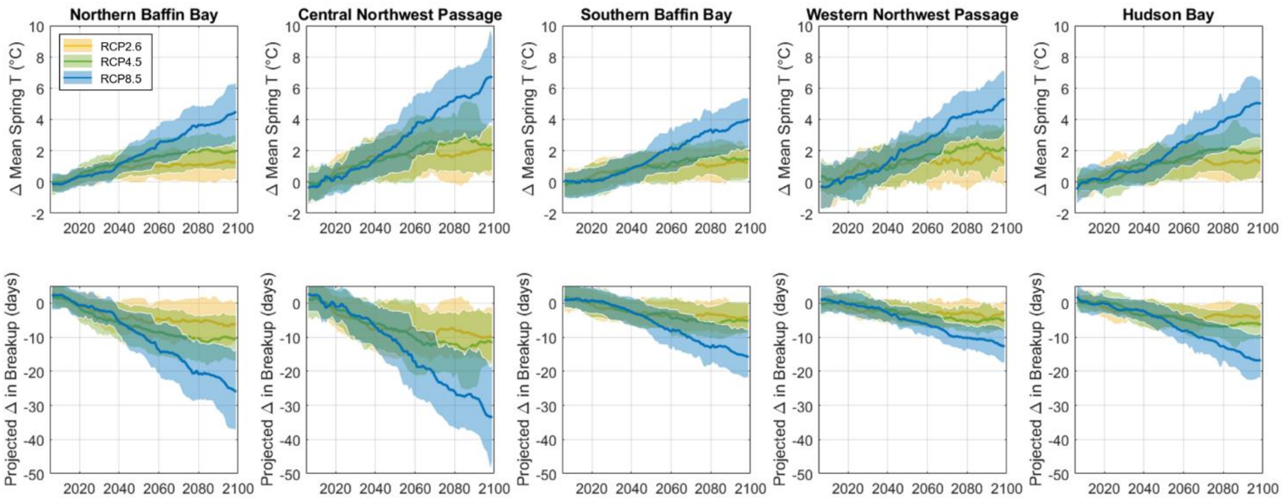

Figure 1.5. Projected changes in shorefast ice breakup using eight CMIP5 climate models. The first row shows the projected changes in springtime air temperature averaged over each sub-region for RCP2.6 (yellow), RCP4.5 (green) and RCP8.5 (blue), and the second row shows the corresponding projected changes in breakup timing for each sub-region. Shaded areas indicate the ensemble-averaged 25th and 75th percentile projections of all the models for each community. Sub-regions are ordered from coldest to warmest from left to right; note the much smaller projected shorefast ice reductions in Southern Baffin Bay, Western Northwest Passage and Hudson Bay compared to the colder Northern Baffin Bay and Central Northwest Passage sub-regions.

Supplementary Information

Supplementary Text 1: Comparison with NSIDC Sea Ice Extent

To determine whether shorefast sea ice extent is correlated with drift ice extent, we compared the MODIS-derived shorefast ice breakup time series to annual sea ice extent indices calculated from the National Snow and Ice Data Center (NSIDC) Sea Ice Index. For each community, we calculated the Pearson's R correlation between breakup timing and annual minimum (September) sea ice extent, minimum extent in March, April and May and the minimum extent during the 36-day "springtime" period as defined for each community. These indices were calculated for each communities' corresponding NSIDC Sea Ice region, namely Baffin, Beaufort, Canadian Arctic Archipelago and Hudson. Note that these NSIDC sea ice regions do not correspond to the regions used in this analysis.

The strongest correlations were found between breakup timing and annual minimum sea ice extent, with nine of the twenty-eight communities exhibiting correlations at $p < 0.05$. Regionally, five of twelve communities located in the Canadian Arctic Archipelago, three of six Baffin communities, and the only Beaufort community exhibited correlations. Interestingly, none of the nine Hudson communities exhibited correlations with annual minimum sea ice extent. We also tested correlations with the minimum ice extent over March-May and the minimum ice extent over the "springtime" period used for air temperature calculations for each community. Tuktoyaktuk, the sole Beaufort community, was the only community that exhibited correlations across all three metrics, suggesting a potential role of linkages between offshore ice and breakup timing along the Tuktoyaktuk Peninsula coast. The lack of consistent correlations in other communities highlights the localized dynamics of shorefast sea ice and cautions against using drift ice records for documenting coastal sea ice change in Northern Canada and Greenland.

Supplementary Figures

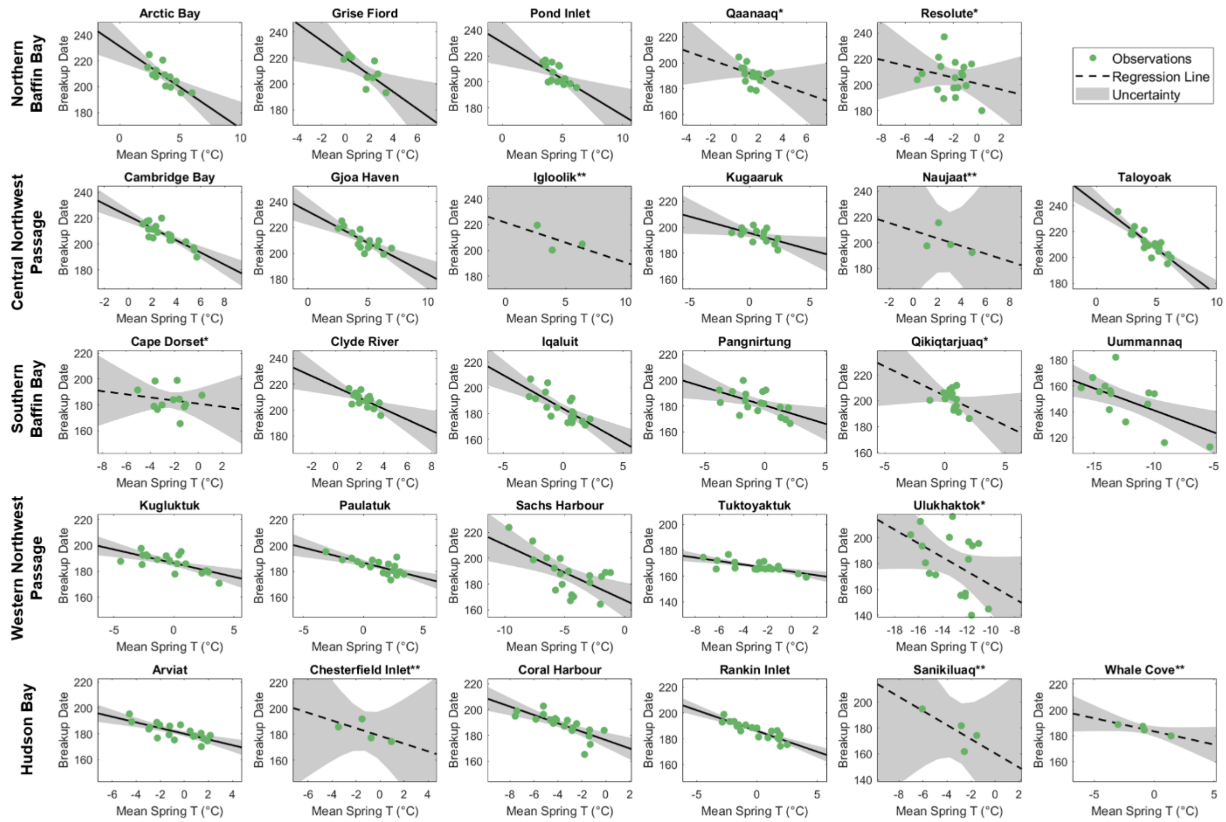

Figure S1.1. Scatter plots of shorefast ice breakup timing vs. mean springtime air temperature (DD, °C) for all 28 communities as calculated using local AWS data. Each row shows communities from the same sub-region as defined in Figure 1. Black lines show the linear regressions between the shorefast ice breakup timing and DD, with gray shading indicating the uncertainty in this regression. Single asterisk after community name indicates communities where breakup timing and degree days are uncorrelated at $p < 0.05$; double asterisk after community name indicates communities with less than 10 years of AWS data. The x and y-axes are standardized by range to illustrate the variability in slope.

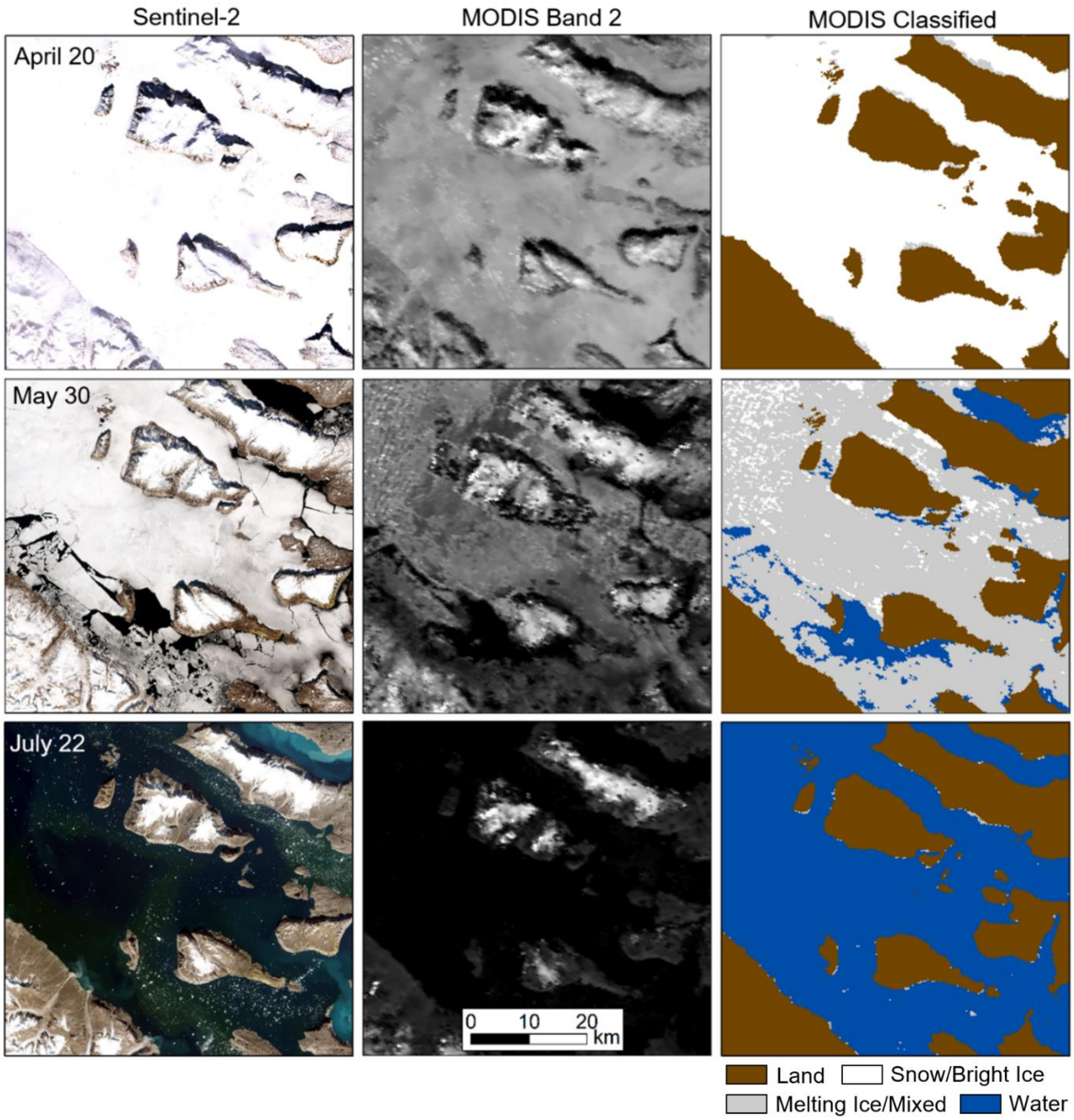

Figure S1.2. Example of MODIS classification in Uummannaq Fjord, Greenland during 2017. Left column shows true color Sentinel-2 imagery, middle column shows MODIS Band 2 (841 – 876 nm) imagery from the same date, and the right column shows the corresponding classification of the MODIS image, where brown is land, white is snow and bright ice, gray is dark, melting ice or mixed ice and water, and blue is water.

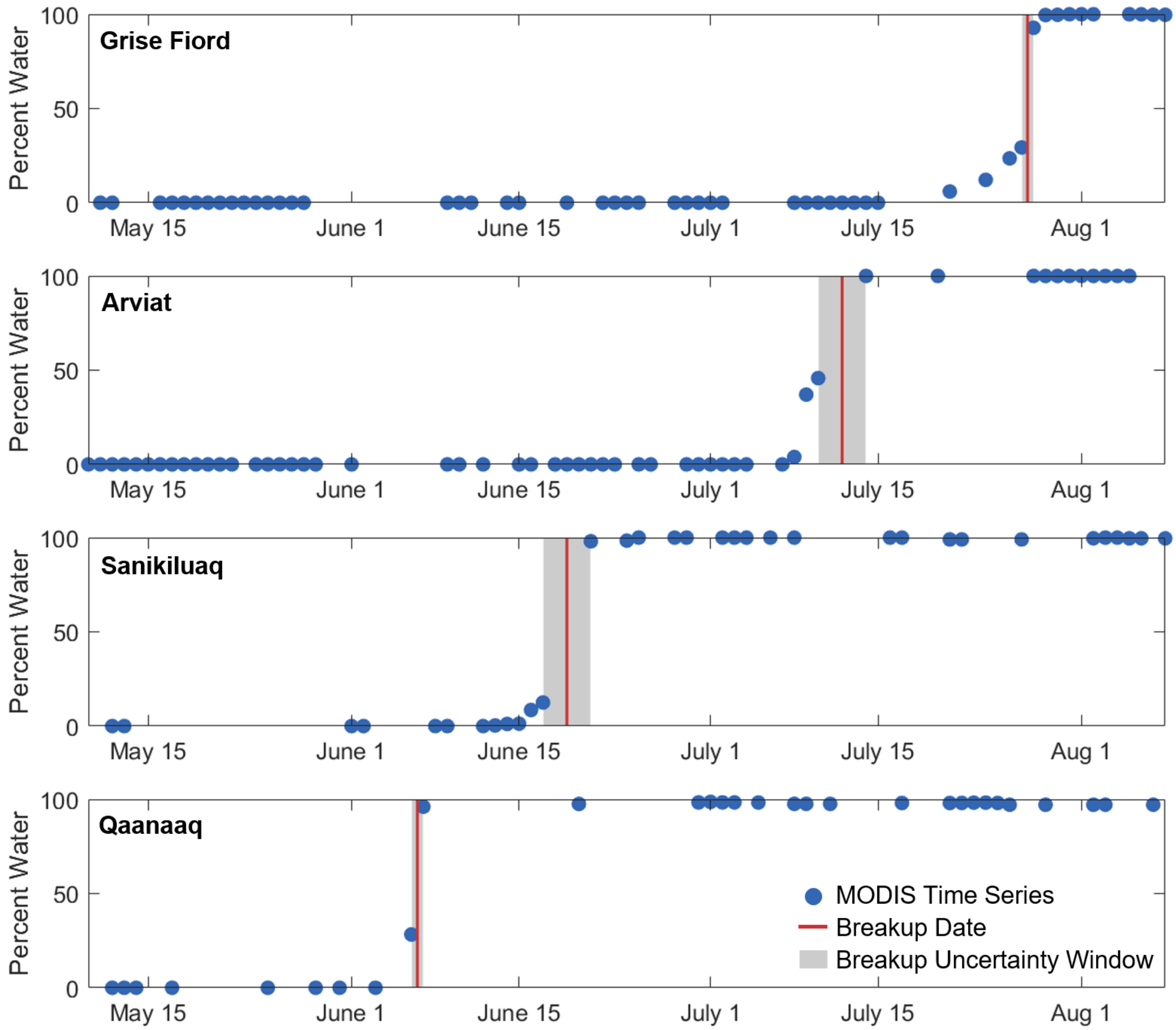

Figure S1.3. Example of MODIS-derived percent water time series for grid cells located near four communities in 2006. The blue dots represent the MODIS time series after cloud removal and median filtering. The red line represents the detected breakup date, defined as the mid-point of the first day where the grid cell >90% water and the previous observation. The gray shaded region represents the uncertainty due to cloud cover.

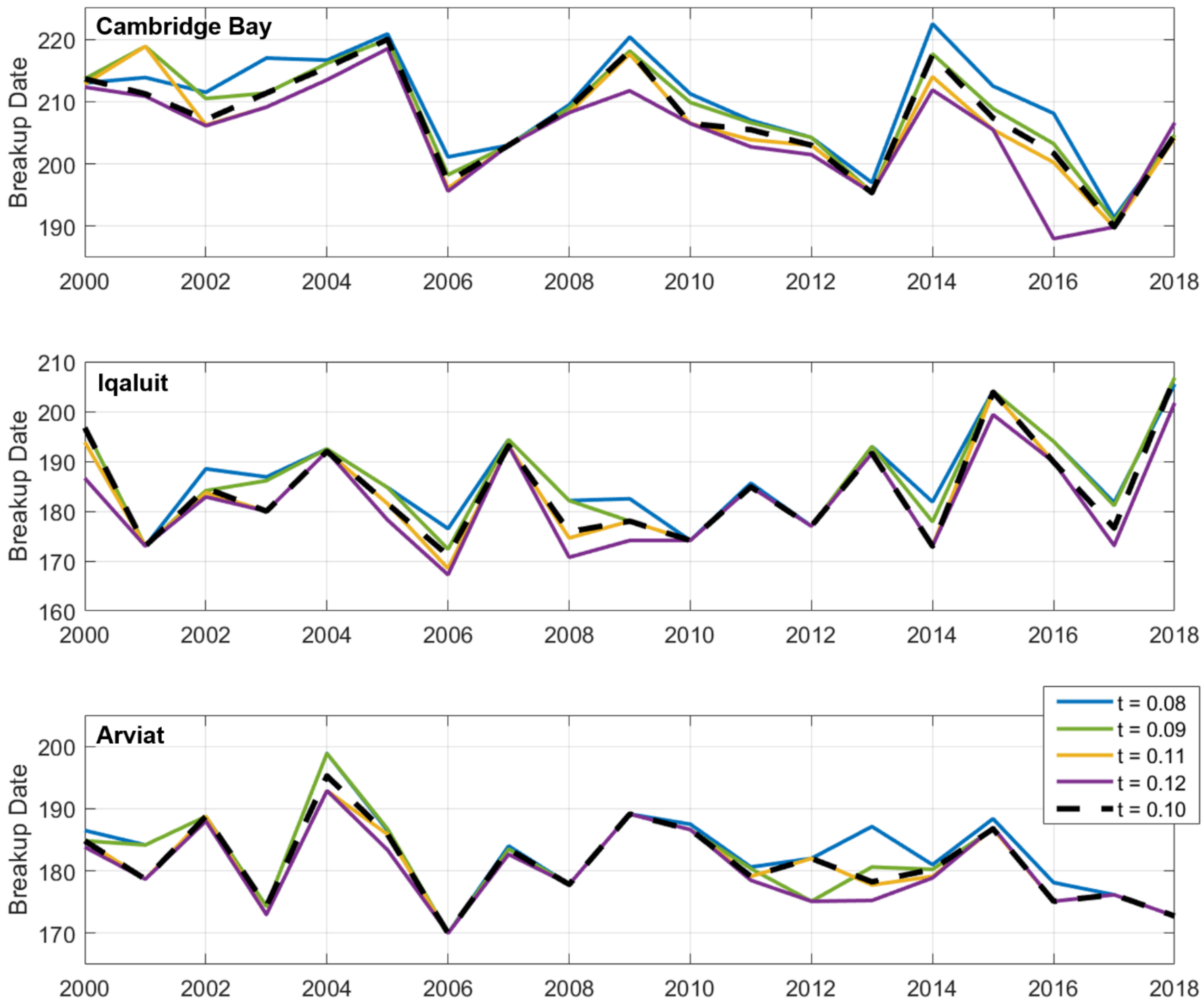

Figure S1.4. Time series of shorefast ice breakup timing for three communities (Cambridge Bay, Iqaluit and Arviat) using five different MODIS band 2 ice/water reflectance thresholds. The chosen threshold, t = 0.01, is shown as a dashed black line. Please note that the reflectance values are the MODIS digital numbers multiplied by 0.001.

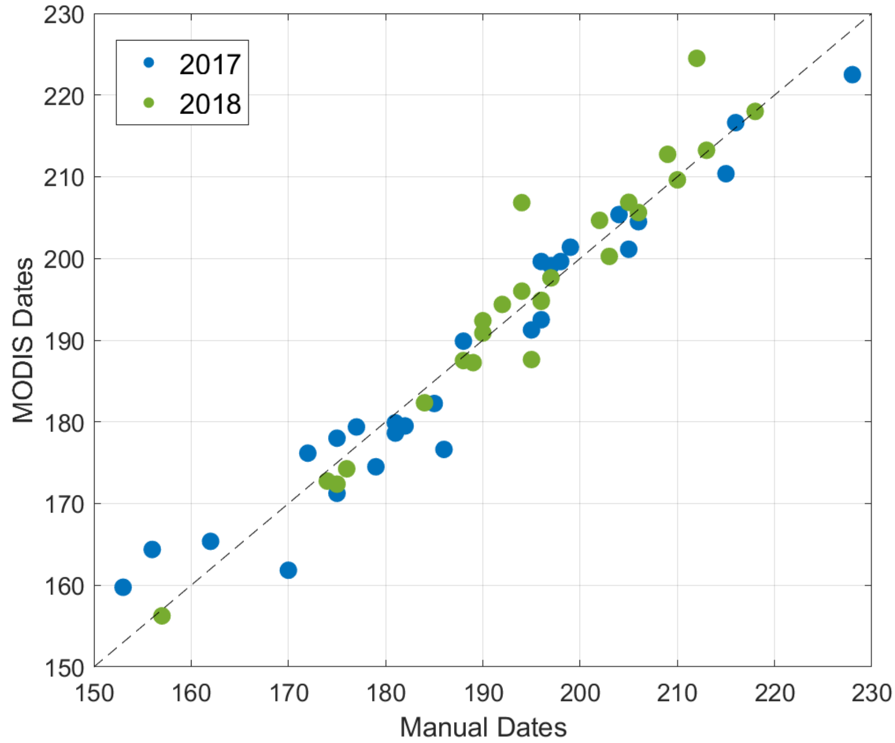

Figure S1.5. Scatter plot of breakup dates manually determined for each community using Planet Labs and Sentinel-2 imagery (x-axis) versus MODIS-derived dates (y-axis). 2017 dates are shown in blue (R^2 = 0.95) and 2018 dates (R^2 = 0.93) are shown in green.

Supplementary Tables

Table S1.1.

Summary of results for each community. MAAT refers to the mean annual air temperature (°C) in each community over 2000-2018. Region refers to the subregions shows in Figure 2, namely: NBB = Northern Baffin Bay, CNP = Central Northwest Passage, SBB = Southern Baffin Bay, WNP = Western Northwest Passage and HB = Hudson Bay. AWS R^2 and ERA R^2 are the Pearson's R^2 of the correlations between springtime air temperature and breakup timing using automated weather station data and ERA-Interim reanalysis, respectively. Bolded and italicized values indicates correlations at $p < 0.01$ and bolded values indicate correlations at $p < 0.05$. AWS and ERA slopes are the slope of the regression line between springtime air temperature and breakup timing; in other words, the sensitivity of breakup timing to air temperature (days/°C). Finally, Δ RCP8.5, Δ RCP4.5 and ΔRCP2.6 refer to change in breakup timing in 2099 as projected using modeled daily temperatures from eight CMIP5 models and the relationships between springtime air temperature and breakup timing for the three different emissions scenarios.

Community	Latitude	Longitude	MAAT	Region	Mean Breakup	Min Breakup	Max Breakup	STD Breakup	AWS R^2	AWS Slope	ERA R^2	ERA Slope	Δ RCP8.5	Δ RCP4.5	Δ RCP2.6
Arctic Bay	73.038	-85.148	-13.9	NBB	207	195	225	8	***0.60***	-6.34	***0.62***	-6.22	-33	-15	-10
Grise Fiord	76.419	-82.902	-13.2	NBB	213	193	231	11	**0.52**	-6.61	**0.28**	-7.48	-25	-13	-9
Pond Inlet	72.700	-77.959	-14.4	NBB	205	196	217	7	***0.37***	-5.61	**0.32**	-5.62	-23	-11	-8
Qaanaaq	77.467	-69.229	-15.6	NBB	192	179	205	7	0.14	NA	***0.39***	-4.93	-14	-7	-5
Resolute	74.697	-94.830	-13.0	NBB	206	180	237	13	0.06	NA	0.08	NA	NA	NA	NA
Cambridge Bay	69.117	-105.060	-12.4	CNP	207	190	220	8	***0.70***	-4.71	***0.62***	-4.76	-29	-11	-9
Gjoa Haven	68.636	-95.850	-11.8	CNP	210	199	225	7	***0.60***	-4.88	***0.56***	-5.12	-32	-13	-12
Igloolik	69.373	-81.825	-11.9	CNP	206	199	226	7	NA	NA	***0.37***	-6.15	-35	-14	-11
Kugaaruk	68.535	-89.825	-13.1	CNP	195	182	215	7	**0.32**	-2.57	***0.53***	-4.73	-27	-11	-10
Naujaat	66.528	-86.245	-10.9	CNP	200	188	216	6	NA	NA	**0.28**	-2.84	-17	-7	-6
Taloyoak	69.537	-93.527	-14.4	CNP	211	195	236	10	***0.77***	-7.10	***0.77***	-6.93	-44	-18	-15
Cape Dorset	64.230	-76.541	-7.6	SBB	184	166	199	9	0.04	NA	0.07	NA	NA	NA	NA
Clyde River	70.476	-68.601	-12.7	SBB	208	196	217	5	***0.38***	-4.23	***0.53***	-6.52	-23	-10	-7
Iqaluit	63.747	-68.517	-8.9	SBB	184	171	207	11	***0.56***	-5.20	***0.61***	-4.21	-16	-6	-6
Pangnirtung	66.147	-65.701	-11.4	SBB	182	167	200	9	**0.33**	-2.82	**0.24**	-2.82	-7	-4	-4
Qikiqtarjuaq	67.556	-64.026	-9.8	SBB	201	186	212	7	0.19	NA	**0.26**	-3.48	-13	-5	-4
Uummannaq	70.677	-52.131	-6.0	SBB	149	113	182	18	***0.45***	-3.42	***0.43***	-4.00	-15	-7	-5
Kugluktuk	67.825	-115.097	-9.2	WNP	187	171	198	7	***0.46***	-2.12	***0.50***	-2.24	-14	-5	-5
Paulatuk	69.351	-124.071	-10.5	WNP	184	173	195	6	***0.52***	-2.35	***0.59***	-2.31	-11	-5	-3
Sachs Harbour	71.985	-125.247	-11.6	WNP	188	164	224	15	***0.40***	-4.29	***0.37***	-4.49	-17	-8	-7
Tuktoyaktuk	69.445	-133.034	-8.8	WNP	167	159	177	4	***0.53***	-1.36	***0.41***	-1.11	-5	-3	-2
Ulukhaktok	70.737	-117.770	-9.6	WNP	182	140	216	24	0.20	NA	0.12	NA	NA	NA	NA
Arviat	61.108	-94.062	-8.2	HB	182	170	195	6	***0.56***	-2.21	***0.52***	-2.39	-11	-5	-3
Chesterfield Inlet	63.347	-90.737	-8.4	HB	183	172	194	6	NA	NA	***0.45***	-2.74	-14	-5	-4
Coral Harbour	64.139	-83.170	-9.8	HB	188	165	203	9	***0.57***	-3.25	***0.52***	-3.48	-15	-6	-5
Rankin Inlet	62.808	-92.085	-9.4	HB	186	174	199	7	***0.78***	-3.21	***0.76***	-3.48	-18	-7	-5
Sanikiluaq	56.541	-79.223	-4.5	HB	172	154	196	12	NA	NA	***0.62***	-5.26	-22	-9	-4
Whale Cove	62.243	-92.602	-7.9	HB	186	172	199	7	NA	NA	***0.70***	-3.27	-17	-7	-5

CHAPTER 2

Tracking Dynamic Northern Surface Water Changes with High-Frequency Planet CubeSat Imagery

Sarah W. Cooley[1,2,3*], Laurence C. Smith[1], Leon Stepan[4] and Joseph Mascaro[4]

[1]Department of Geography, University of California, Los Angeles, California, 90095
[2]Department of Earth, Environmental and Planetary Sciences, Brown University, Providence, Rhode Island, USA, 02912
[3]Institute at Brown for the Environment and Society, Brown University, Providence, Rhode Island, USA, 02912
[4]Planet Labs, Inc., San Francisco, CA, 94103, USA

Published in *Remote Sensing*

Citation: Cooley, S.W., Smith, L.C., Stepan, L. and Mascaro, J. (2017), Tracking dynamic northern surface water changes with high frequency Planet CubeSat imagery, *Remote Sensing 9*, 1309. doi.org/10.3390/rs9121306

Abstract

Recent deployments of CubeSat imagers by companies such as Planet may advance hydrological remote sensing by providing an unprecedented combination of high temporal and high spatial resolution imagery at the global scale. With approximately 170 CubeSats orbiting at full operational capacity, the Planet CubeSat constellation currently offers an average revisit time of <1 day for the Arctic and near-daily revisit time globally at 3 m spatial resolution. Such data have numerous potential applications for water resource monitoring, hydrologic modeling and hydrologic research. Here we evaluate Planet CubeSat imaging capabilities and potential scientific utility for surface water studies in the Yukon Flats, a large sub-Arctic wetland in north central Alaska. We find that surface water areas delineated from Planet imagery have a normalized root mean square error (NRMSE) of <11% and geolocation accuracy of <10 m as compared with manual delineations from high resolution (0.3–0.5 m) WorldView-2/3 panchromatic satellite imagery. For a 625 km^2 subarea of the Yukon Flats, our time series analysis reveals that roughly one quarter of 268 lakes analyzed responded to changes in Yukon River discharge over the period 23 June–1 October 2016, one half steadily contracted, and one quarter remained unchanged. The spatial pattern of observed lake changes is heterogeneous. While connections to Yukon River control the hydrologically connected lakes, the behavior of other lakes is complex, likely driven by a combination of intricate flow paths, underlying geology and permafrost. Limitations of Planet CubeSat imagery include a lack of an automated cloud mask, geolocation inaccuracies, and inconsistent radiometric calibration across multiple platforms. Although these challenges must be addressed before Planet CubeSat imagery can achieve its full potential for large-scale hydrologic research, we conclude that CubeSat imagery offers a powerful new tool for the study and monitoring of dynamic surface water bodies.

1. Introduction

Quantifying spatial and temporal variability in surface water area and storage is critical for effective water resource management, testing flood models, and assessing impacts of environmental and climatic change. In situ monitoring stations for lake water levels and river discharge are sparse and furthermore provide only one-dimensional point observations that acceptably characterize inundation and storage in well-defined, constrained bathymetries but not in complex floodplains and/or wetland environments (Alsdorf, Rodriguez, et al., 2007). In situ monitoring of shoreline boundaries is exceedingly rare, as are water level gauges in small lakes. While river gauges are common in cities and developed countries, they are sparse in other areas, particularly in the Arctic (Alsdorf, Rodriguez, et al., 2007; Fekete et al., 2012; Shiklomanov et al., 2002). Remotely sensed measurements of surface water are consequently an essential supplement to ground measurements for measuring, monitoring and modeling global water resources (Doug Alsdorf, Rodriguez, et al., 2007; Lettenmaier et al., 2015).

Although mapping surface water extent using optical imagery is well established (Alsdorf, Rodriguez, et al., 2007; Smith, 1997), a tradeoff between high spatial versus high temporal resolution sensors has traditionally prevented study of dynamic, fine-scale changes in surface water extent over short temporal scales. Surface water mapping has a long legacy with Landsat sensors (TM, ETM, OLI) due to their relatively high spatial resolution (30 m), high radiometric quality, and long term continuous record (Pekel et al., 2016), yet their historical 16-day revisit time, typically lower due to cloud cover, limits the applicability of Landsat for tracking sub-seasonal patterns in surface water extent. The twin Sentinel-2 satellites now offer more frequent returns (5–10 days) at 10 m resolution, but cloud obscuration still lowers the actual revisit frequency. MODIS imagery is often used to study large, dynamic hydrologic systems such as rivers (e.g. Smith & Pavelsky, 2008), wetlands (e.g. Pavelsky & Smith, 2008) and lakes (e.g. McCullough et al., 2012) due to its daily periodicity, but the coarse resolution of MODIS visible/NIR bands (250–500 m) means only coarse scale variability can be distinguished. Combining MODIS and Landsat observations can enable near-daily, 30 m land surface monitoring, though the results are sensitive to the blending algorithm used (Emelyanova et al., 2013; Gao et al., 2006; Jarihani et al., 2014). This compromise between high spatial and temporal resolution has thus limited the ability to track both fine-scale, sub-seasonal patterns in surface water extent.

High frequency observations of surface water extent are particularly critical for study of dynamic high latitude hydrologic processes. The high latitudes contain the highest proportion of small water bodies on Earth (Lehner & Döll, 2004; Smith et al., 2007), nearly all of which are unvisited and unstudied. Due to strong seasonality, northern lakes and rivers are highly dynamic. Spring river ice breakup and associated peak flow and flooding can lead to rapid changes in surface water extent (Goulding et al., 2009; Lesack et al., 2013). Such peak flow events are critical for recharging lakes and wetlands, transporting water through low-relief floodplains (Marsh & Lesack, 1996; Pavelsky & Smith, 2008; Prowse & Conly, 1998). Warming Arctic temperatures have increased interest in understanding how surface water extent responds to thawing permafrost (Jorgenson & Osterkamp, 2005; Smith et al., 2005). Permafrost acts as a barrier between the surface hydrologic system and the groundwater system, meaning that in discontinuous permafrost, the surface water and groundwater systems are connected where permafrost is absent but disconnected where permafrost is present (Jorgenson & Osterkamp, 2005; Walvoord & Kurylyk, 2016). In high latitude wetlands underlain by discontinuous permafrost, such as the Yukon Flats in central Alaska, decadal-scale analyses (>30 years) of interannual patterns in lake area have noted variable changes in surface water extent due to a combination of thawing permafrost, shortening spring duration of snow cover, changing water balance and underlying hydrogeology (Anderson et al., 2013; Chen et al., 2014; Jepsen et al., 2013; Riordan et al., 2006; Rover et al., 2012). Despite evidence that sub-seasonal cycles strongly influence patterns in surface water extent, potentially obscuring climate-related trends (Chen et al., 2014), little research has focused on fine-scale, sub-seasonal variability in these areas, due to the absence of sufficient high resolution, high frequency imagery.

Recent development of small, affordable satellites known as CubeSats opens new possibilities for studying fine-scale, temporally dynamic hydrological processes from space. CubeSats are typically about the size of a bread box (0.003 m^3), and contain little more than a four-band multispectral camera and power/downlinking equipment. Owing to their small size and low cost, CubeSat imagers can overcome the tradeoff between high spatial and high temporal resolution by deploying them in a multi-satellite constellation. This approach relies on both satellite mass production and declining launch costs, making CubeSats comparatively affordable for commercial satellite companies to launch and operate (McCabe et al., 2017). A notable example is Planet (formally known as Planet Labs; http://planet.com), a company that has successfully built and launched 281 CubeSats since 2013. With 148 CubeSats in sun-synchronous orbit, Planet currently images nearly all of the global land surface at 3–5 m resolution daily, providing near-real time imagery to paid and academic subscribers. This large volume of frequent, high resolution imagery holds potential value for hydrological applications because open water surfaces are among the simplest land covers to discriminate in visible/NIR imagery, and frequent observations are necessary to track dynamic hydrologic processes such as flood waves and river ice breakup. However, CubeSat imagery is acquired using inexpensive sensors which cannot achieve the same radiometric quality, consistency and signal-to-noise ratios of space agency-funded missions (Houborg & McCabe, 2016). Together with the newness of CubeSats, prevailing concerns about cross-sensor calibration, image quality, geolocation accuracy, and data availability have limited the advent of CubeSat-based hydrological research. Despite the strong potential of frequent, high-resolution CubeSat imagery to transform hydrological remote sensing, such data remain generally untested and unproven within the hydrologic community (McCabe et al., 2017).

Here, we present a first demonstration of the use of CubeSat imagery to track sub-seasonal changes in surface water extent. Using two types of Planet satellite imagery we tracked surface water inundation variations across a 625 km^2 study region in the Yukon Flats, north central Alaska during summer 2016 as follows: First, we developed a non-binary water classification method for Planet imagery (adapted from Olthof et al., 2015) and validated it with concurrent WorldView-2 satellite images; second, we analyzed sub-seasonal patterns in lake and river surface areas and their sensitivity to measured discharge variations in the Yukon River; finally, we assess Planet's anticipated future imaging capabilities and discuss some potential applications and limitations that must be addressed before CubeSat imagery can be widely used in hydrologic research.

2. Study Area and Data

2.1. Study Area

A 625 km^2 study area (centered at 66.3 N, −147.4 W) was selected within the Yukon Flats, a dynamic wetland system in north central Alaska surrounding an extended low-relief section of the

Yukon river (Figure 2.1). This defined area contains >450 lakes and a 30 km section of the Yukon river, as well as the small settlement of Beaver, AK (Figure 2.1, box a). We also performed lake area validation in two other subareas in the Yukon Flats (Figure 2.1, box b,c). The Yukon Flats are characterized by extremely cold winters (mean January air temperature of −23 °C) and warm, dry summers (mean July air temperature of 17 °C) with low annual precipitation (26.7 cm water equivalent on average) (Chen et al., 2014). The study area is primarily covered by spruce and birch forest and marshland and is underlain by discontinuous permafrost (Chen et al., 2014; Jorgenson et al., 2008; Minsley et al., 2012; Pastick et al., 2013). Lakes in the Yukon Flats typically depend on recharge from spring river ice breakup flooding events (Chen et al., 2014). In recent years several studies have analyzed long-term inter-annual trends in surface water extent to assess a potential role of thawing permafrost (Anderson et al., 2013; Chen et al., 2014; Jepsen et al., 2013; Riordan et al., 2006; Rover et al., 2012).

2.2. Remote Sensing Data

Planet currently distributes three types of imagery, RapidEye, PlanetScope, and SkySat, two of which are studied here (Table 2.1). RapidEye refers to a constellation of 5 satellites (dimensions 0.8 m × 0.94 m × 1.2 m) launched in 2008 by German company RapidEye AG and now acquired and operated by Planet. RapidEye imagery has 5 bands, blue (Band 1, 440–510 nm), green (Band 2, 520–590 nm), red (Band 3, 630–685 nm), red edge (Band 4, 690–730 nm) and near infrared (Band 5, 760–850 nm) and a ground spatial resolution of 6.5 m. PlanetScope is a constellation of 120 smaller CubeSats known as ‘doves’ (dimensions 10 cm × 10 cm × 30 cm) built and operated by Planet, and launched in groups called ‘flocks’. PlanetScope imagery has four bands, blue (Band 1, 455–515 nm), green (Band 2, 500–590 nm), red (Band 3, 590–670 nm) and near infrared (Band

4, 780–860 nm) and a ground spatial resolution of 3.7 m. Skysat imagery has four bands (blue, green, red and NIR) and a ground resolution of 0.8 m. As it is a constellation of 13 satellites, however, SkySat currently captures imagery only over tasked areas (typically urban and developed areas). It was not available to this study and therefore excluded from the analysis.

For both RapidEye and PlanetScope we analyzed the Planet Level 3A data product ("Analytic Ortho Tile Product") which is a mosaic of multiple images from the same swath aggregated into uniform 25 km × 25 km tiles. This product is projected to UTM coordinates and orthorectified using GCPs and fine-scale DEMs to a positional accuracy of <10 m RMSE (Planet Team, 2018). Planet Level 3A imagery is also converted to absolute radiometric values using calibration coefficients that are monitored and updated for each satellite (see Section 5.2). Following radiometric calibration (Planet Team, 2018), the Level 3A product has 16-bit spectral resolution. RapidEye and PlanetScope data availability was irregular in summer 2016, when Planet's multi-satellite flocks were in early stages of deployment. Therefore, the revisit rates presented in this study are irregular and less frequent than current revisit rates at full operational capacity. We examined all RapidEye and PlanetScope imagery in one Planet tile (No. 0669714) collected in summer 2016, which due to data availability limitations ranges from 23 June to 1 October (Table 2.2). To validate our water extraction method, we also used panchromatic WorldView-2 and WorldView-3 imagery operated by DigitalGlobe (Table 2.2). The panchromatic band (450–800 nm) has a ground resolution of 0.5 m (WorldView-2) and 0.3 m (WorldView-3).

2.3. River Discharge

In situ river discharge data for the Yukon River was obtained from the USGS station located in Eagle, Alaska, approximately 400 km upstream of our study area. We created a discontinuous time series of daily discharge measurements corresponding to each remotely sensed date of observation. While a simplification of the discharge time series, this approach facilitated a useful comparison between remotely sensed river width and in situ discharge.

3. Methods

3.1. Water Classification

To classify open water from surrounding land and vegetation, a 10-step procedure was used (Figure 2.2). First, Planet imagery were manually checked for clouds. Although Planet does provide a cloud index value indicating the percent of cloud-covered pixels for each image, the index performance is not consistent in snow and ice conditions at present and a cloud mask product is still unavailable. For every image where clouds were present, cloud cover and cloud shadow masks were manually digitized and masked out. We ignored all imagery with a solar zenith angle greater than 78 degrees or with cloud cover greater than 70%. We then calculated a Normalized Difference Water Index (NDWI) for each image, defined as the difference between the green and near-infrared reflectance (Band 2–Band 5 for RapidEye, Band 2–Band 4 for PlanetScope) divided by the sum of the green and near-infrared (Band 2 + Band 4/5) (McFeeters, 1996). This yields an *NDWI* index value between −1 and 1, where open-water pixels approach 1 and are more easily distinguishable from non-water pixels.

For water classification, we used a water fraction approach adapted from Olthof et al., (2015), who originally applied this method to shortwave infrared (1550–1750 nm) Landsat TM and ETM+ imagery. In complex floodplain environments such as the Yukon Flats where inundated vegetation and mixed land/water pixels are common, a multi-step, non-binary water classification enables more accurate water area extraction through accounting of fractionated water pixels (Olthof et al., 2015). First, Otsu adaptive thresholding (Otsu, 1979) was used to delineate potential water bodies in a maximum extent image to create an initial water mask (Figure 2.3a). All water bodies less than 2500 m^2 were removed from this initial mask. The water mask was then dilated using a 60 m disk object and converted to polygons, yielding an initial buffered polygon mask containing both the maximum extent of the water body and some surrounding land and vegetation (Olthof et al., 2015). These buffered lake polygons were then intersected with the NDWI for each image, generating a histogram of NDWI pixels within the buffered water mask (Figure 2.3b).

The water fraction of each pixel was then determined by applying dynamic land and water thresholds to each image (Olthof et al., 2015). The buffered water histograms typically have two peaks, one characteristic of land pixels (lower NDWI) and the other of water pixels (higher NDWI). We identified the 100% land threshold (*LL*) and 100% water threshold (*WL*) as:

$$LL = height_{lp} - 0.9 \times prom_{lp} \qquad (1)$$

$$WL = height_{wp} - 0.9 \times prom_{wp} \qquad (2)$$

where $height_{lp}$ and $height_{wp}$ are the heights of the land/water peak respectively and $prom_{lp}$ and $prom_{wp}$ are to the prominences of the land/water peaks. We then calculated the water fraction (*WF*) for each pixel as (Olthof et al., 2015):

$$WF = 100 \times \frac{NDWI - LL}{WL - LL} \qquad (3)$$

The water fraction is thus the percent of each pixel that is inundated or water covered and is particularly useful in this region where many pixels contain inundated vegetation. All NDWI pixels $\geq$ *WL* were considered 100% water and all NDWI pixels < *LL* were considered 100% land.

3.2. Time Series Analysis

Following generation of water fraction maps, we tracked lake and river surface area changes over the late summer season. Due to the presence of clouds and varying swaths and pixel sizes of Planet imagery, an object-based approach was used to track changes in lake and river extent, with each water body treated as an individual object. This approach is well-suited for time series analyses involving different sensors and ground resolutions and additionally limits the impact of potential geolocation error. To do this, we first reapplied the maximum extent buffered polygons to each water fraction map and calculated the total area of pixels within each polygon that are 100% water and greater than 75% water for each image. We also determined the total >50% fractionated water area within each polygon by summing the pixel values for all pixels greater than 50% water. This created a sub-seasonal time series consisting of three different lake areas for each lake observation (>50%, >75%, 100%). We primarily used >75% area for our time series analyses but observed temporal patterns are similar for all three metrics. We analyzed changes in river surface area by examining seven individual river reaches ranging from 2.5 to 3.5 km in length. To better facilitate comparison between reaches, river surface area was converted to effective width (W_e) (L. C. Smith et al., 1995, 1996; SMITH, 1997) by dividing by the length of each river reach. If multiple PlanetScope image acquisitions were acquired on the same day, we assigned the largest observed lake area or river W_e to that day. Finally, to illustrate large-scale changes in inundation extent, we produced pixel-based water fraction change maps between three cloud-free RapidEye images representing early (23 June), mid (17 August) and late (1 October) season.

3.3. Validation of Planet Water Fraction Maps

A key component of assessing the utility of Planet imagery for water mapping is determining whether surface water area can be reliably and automatically extracted from CubeSat imagery. We validated our Planet imagery water fraction maps by comparing them to lake shorelines delineated manually from one WorldView-2 and two WorldView-3 panchromatic images acquired on 30 August and 8 September 2016 (Table 2.1). WorldView-2 and WorldView-3 offer high radiometric stability and finer spatial resolution (0.5 m, 0.3 m respectively) than RapidEye and PlanetScope imagery, and have been previously demonstrated to yield high-quality mapping of surface water (Jawak & Luis, 2014; Wolf, 2012). We delineated 48 lakes from the September 8 image and 45 lakes from the 30 August image, and compared them to our water fraction classification of one 8 September RapidEye image (Figure 2.1 inset c) and three 2 September PlanetScope images (Figure 2.1 inset b), respectively. We compared 100% water area, >75% water area and >50% fractionated water area with the manually delineated WorldView area (Figures 2-4 and 2-5).

Geolocation error is also thought to affect CubeSat imagery due to the small size of the satellites and possible orbital drift. To assess image geolocation accuracy, we reprojected the manually delineated WorldView lakes to WGS84 UTM Zone 6N to correspond with Planet's gridding system. We then calculated the centroids of both the manually delineated WorldView lakes and RapidEye/PlanetScope-derived lakes and compared the centroids of the WorldView lakes to the centroids of the RapidEye/PlanetScope lake boundaries outlining >75% water area.

4. Results

4.1. Detection of Surface Water

We find strong agreement ($r^2 > 0.99$) between lake boundaries manually delineated in high-resolution WorldView-2 and WorldView-3 images and water fraction classifications derived from Planet RapidEye and PlanetScope imagery (Figure 2.4). The normalized root mean square errors (NRMSE) vary from 5.7% to 18.7% for RapidEye, with >75% area showing the best agreement (NRMSE = 5.7%) with WorldView images (Figure 2.4). The NRMSEs vary less for PlanetScope, ranging from 10.9% to 12.6%. While the WorldView and RapidEye images are contemporaneous (taken 2 minutes apart), the three days between WorldView and PlanetScope image acquisitions may be responsible for the higher RMSEs for PlanetScope. The mean Euclidean distance between Planet and WorldView lake centroids is 9.8 ± 4.1 m for RapidEye and 10.5 ± 3.2 m for PlanetScope, comparable with the <10 m ground location accuracy Planet claims for its imagery (Planet Team, 2018). This analysis was only performed for lakes where the classifications yielded similar lake geometry and thus the difference between the centroids primarily represents a geolocation offset rather than classification error. However, for all lakes, some of the offset may derive from classification differences, meaning our reported geolocation errors are conservative estimates of the actual offset. The direction of the offsets varies between different images but is generally consistent within a single image (Figure 2.5). For the 2 September PlanetScope image, the offset primarily trends northeast, with azimuths for individual lakes ranging from due north to due east. For RapidEye the offsets are more variable between lakes but generally trend within 45° of due north. In sum, combined, the ~10% NRMSEs and 10 m ground offsets suggest water area can be reliably extracted from Planet imagery within reasonable error.

4.2. Temporal Changes in Water Inundation Area

Over the course of the mid to late summer season (23 June to 1 October) we identified a total of 470 lakes >2500 m^2 within our 625 km^2 study area. These water bodies received between 4 and 9 cloud-free Planet observations over this period, with an average of 6.0 cloud-free observations. The maximum observed lake area is 1.23 km^2, and for all lakes >2500 m^2, the mean maximum lake size is 0.0735 km^2 or 73,470 m^2. On average, the studied lakes lost 0.028 km^2 of surface water area, or 63% of their maximum observed area over the summer season. However, not all water bodies followed this average trend, with some shrinking, some expanding, and others stable. Because a lake's areal change tends to scale with its area (Smith & Pavelsky, 2009), we divided lakes into two categories, i.e., 2500 m^2–10,000 m^2 and lakes >10,000 m^2. On average, lakes <10,000 m^2 lost 4280 m^2 or 79% of their maximum observed area as the summer progressed, whereas lakes >10,000 m^2 lost 42,900 m^2 or 52% of their maximum area. The normalized variability for each lake, which we defined as the mean change in lake area between each observation, decreased significantly with area. For all lakes >2500 m^2, the mean variability is 47%, but the mean variability is 67% for lakes between 2500 m^2 and 10,000 m^2, and 33% for lakes >10,000 m^2.

Yukon River effective width W_e varied most strongly on wide reaches surrounded by sediment bars and least on narrow constrictions (Figure 2.6a,b). Effective widths of Reach 3 and Reach 7 changed little over the observation period, whereas other reaches increased in mid-August (observations 4–6, Figure 2.6b,c) before decreasing to a seasonal low in October. Effective width is correlated with discharge (Ashmore & Sauks, 2006; Smith et al., 1995, 1996; Smith, 1997; Smith & Pavelsky, 2008) so to assess the validity of Planet W_e measurements we compared them with Yukon River discharge data from the USGS station at Eagle. We find that a daily discharge time series corresponding to our dates of observation correlates well with our effective width measurements, yielding an r^2 of 0.75 ($p < 0.01$) (Figure 2.6c,d).

While most of the Yukon Flats lakes studied here decreased in surface area over the observation period, heterogeneous patterns of lake area increase and stability are also evident (Figure 2.7). Overall, 83% of the studied lakes decreased in area between 23 June and 1 October 2016, with 22% losing at least half of their surface area. Between 23 June and 17 August, however, 56% of lakes increased in surface area, and 89% of lakes shrunk between 17 August and 1 October. This summertime peak in mid-August and subsequent decrease in surface extent exhibited by more than half of lakes is also reflected in the time series of river effective width (Figure 2.6), signifying hydrologic connectivity of these lakes to the main-stem Yukon River.

In low-relief wetland environments where a small change in water level can cause a large change in inundation extent, temporal correlations between changing river discharge and individual lake surface areas are indicative of floodplain connectivity (Pavelsky & Smith, 2008). To quantify these correlations, for each lake object with at least 5 satellite observations and an observed maximum area >10,000 m^2, we calculated Pearson's R between the Yukon River discharge at Eagle and Planet time series of surface water extent (Pavelsky & Smith, 2008). Of the 268 lakes meeting these requirements, 100 (37%) are correlated with Yukon River discharge at the 90% confidence level and 60 (22%) are correlated at the 95% confidence level.

Using a non-parametric Mann-Kendall test (Helsel & Hirsch, 1992) we also assessed how many of these 268 lakes display statistically significant trends over the summer season. We find 65 (24%)

of lakes have a statistically significant ($p < 0.1$) decreasing linear trend over the summer season, 2 (1%) display increasing trends, and 201 (75%) display no trend. As nearly all lakes decreased in extent, the percent of lakes with statistically significant trends reflects lakes which changed linearly with little bidirectional variability between observations.

Based on the observed correlation to river discharge, we characterized the 268 study lakes into three categories: connected, disconnected and stable, examples of which are shown in Figure 2.8. Connected lakes are interpreted as being hydrologically connected to the Yukon River (Pavelsky & Smith, 2008) and thus immediately responsive to changes in its discharge. Here we defined connected lakes as having a surface area standard deviation >10% and a statistically significantly ($p < 0.1$) correlation to river discharge. 77 lakes (28%) were classified as connected. In some cases, such as the example shown in Figure 2.8b, there may be a visible channel connecting the lake to the river system, but in many connected lakes no such channel is visible in the imagery. Disconnected lakes are uncorrelated with river discharge, but still experience substantial area changes over the summer season. These lakes typically steadily decrease in surface area throughout the summer season and do not respond to the summer high stage event. Here they were defined as lakes with a surface area standard deviation >10% and no correlation to Yukon river discharge, with 128 lakes (48%) classified as disconnected. Finally, stable lakes are interpreted as being hydrologically disconnected from the Yukon River water, possibly due to steep embankments, sills or other topographic controls, and/or sustained by connections to groundwater. They were defined in this study as lake objects having a surface area time series standard deviation of less than 10%, totaling 63 lakes (24%). There is no clear spatial pattern explaining the distribution of the different lake types, though we do observe some spatial clustering of lakes of the same type (Figure 2.9).

5. Discussion

5.1. Assessment of Planet Imagery

5.1.1. Utility of Planet CubeSat Imagery for Tracking Surface Water Dynamics

This study demonstrates that Planet imagery is suitable for mapping and tracking changing inundation extent of hundreds of small, heterogeneous water bodies in a complex, dynamic wetland region. We find the surface areas of small water bodies can be reliably and automatically extracted from both RapidEye and PlanetScope imagery, with a mean NRMSE of ~11%. While the nominal ~10 m geolocation error of Planet imagery (Planet Team, 2018) will likely cause difficulties for comparing Planet imagery to other fine-scale map products and/or field measurements, our treatment of water bodies as fuzzy-geolocation objects mitigates this error for time-series analysis purposes, and a geolocation offset of <10 m is sufficient for analysis of lakes >2500 m^2. Furthermore, this geolocation error is a systematic offset (though with inconsistent directions between images) and would thus be correctable through a simple transformation. The strong correlation between Yukon River effective width and discharge (Figure 2.6), further highlights Planet's utility for obtaining useful sub-seasonal hydrologic measurements from space.

5.1.2. Limitations and Challenges

Several important limitations remain to be addressed before CubeSat imagery can be fully implemented into larger-scale hydrological observing systems. Currently, a serious limitation is lack of a cloud mask or a regionally/globally applicable automated cloud masking algorithm derived from Planet imagery. Automated cloud detection in multi-temporal visible/near-infrared satellite imagery is non-trivial (Tseng et al., 2008) and will be particularly challenging with PlanetScope given only four bands and variable quality imagery. Until an automated cloud masking product or algorithm is developed, researchers must manually remove clouds which generally precludes broad-scale, high-resolution applications including surface water mapping. While minor, the observed geolocation error, combined with the narrow swath width of Planet CubeSat imagery, make differencing difficult at fine spatial scales (i.e., 50 m × 50 m lakes). Use of an object-based approach (Figures 2.3 and 2.7) mitigates but does not fully eliminate this problem.

Additional limitations associated with CubeSat imagery derive from its inexpensive sensors and multi-satellite constellation approach. PlanetScope imagery is calibrated to a radiometric uncertainty across satellites of 5–6% at 1-sigma (Wilson et al., 2017) and RapidEye is calibrated to 4% uncertainty (Naughton, 2011). These values compare reasonably to Landsat at-sensor calibration uncertainty, which ranges from 3% (OLI) to 5% (TM and ETM+) to 10% (MSS) (Chander et al., 2009; Markham et al., 2014; Markham & Barker, 1987). However, to enable daily or near-daily high resolution observations of the entire globe, Planet is presently operating 148 satellites in sun-synchronous orbit, meaning a collection of images of the same location likely come from many sensors. While all imagery is calibrated, Planet image quality, including signal to noise ratio and exposure, can vary between sensors, a non-trivial error source when time series analyses involve imagery from tens of sensors (Wilson et al., 2017). Figure 2.10 illustrates this variability in near infrared and NDWI for water bodies and surrounding wetlands in five

PlanetScope images taken within a 10-day period in 2016. Though some of the observed differences may be due to atmospheric scattering and absorption, the non-linearity of between-image offsets suggests radiometric calibration and/or sensor variability is likely the cause.

The lack of atmospherically corrected Planet imagery also complicates the interpretation of time series analyses, particularly those involving global radiance thresholds or complex land surface classifications (Houborg & McCabe, 2016). Fully automated time series analyses using Planet data may thus require dark body atmospheric correction (Chavez, 1988), adaptive thresholding as demonstrated here, or combination with other sensors (Houborg & McCabe, 2016). The narrow range of the electromagnetic spectrum sampled by Planet's sensors (455–860 nm) also limits utility of the resulting imagery. For example, variability in shortwave infrared (1400–3000 nm) is critically important for distinguishing between cloud, snow, ice and water surfaces (Hall et al., 2002), thus restricting the types of observations that can be made from Planet imagery in areas where snow occurs. Given these issues, hydrological applications of Planet imagery should presently be limited to relatively simple classifications, such as water mapping, which do not require atmospheric correction or rely on predefined radiance thresholds. All imagery classified in this analysis was visually checked and in general our automated classification method performed well for all imagery, suggesting image quality problems can be minor. However, further research is needed to examine radiance variability between different PlanetScope satellites and the effect this has on different types of classification. For example, combining PlanetScope imagery with Landsat-8 surface reflectance products may reduce cross-sensor calibration error (Houborg & McCabe, 2016). Furthermore, a PlanetScope surface reflectance product produced from tandem observations with other sensors is now being tested and available in Beta as of 1 October 2017 and may allow more rigorous analyses (Planet Team, 2018).

Despite the above issues, specific methodological considerations can overcome some of them to enable robust hydrological analyses. First, water classifications based on a band ratio index such as NDWI is better suited for Planet analyses as it precludes the need for atmospheric correction (Song et al., 2001). We also advise against the use of global/stable thresholds due to cross-sensor variability. Perhaps the most critical methodological step is object-based time series analysis. By assigning the water extent change as an attribute to the lake polygon, and ignoring small temporal changes in lake location, problems of small image offsets and mismatched water edge boundaries are avoided. This approach is particularly important for Planet analyses due to geolocation uncertainty, the use of multiple sensors and varying resolution and swath coverage of the imagery. We therefore still conclude that Planet imagery is valuable for tracking rapid, fine scale changes in surface water extent, particularly as observation frequencies reach the company's near-daily imaging capacity (Planet Team, 2017).

5.2. River-Floodplain Connectivity of the Yukon Flats

The high spatial and temporal resolution of Planet imagery, accompanied by the non-binary classification method's ability to detect water extent in the variable quality data make Planet imagery particularly useful for study of complex, dynamic surface water systems. Floodplains and wetland environments are dependent on hydrologic recharge from rivers, precipitation and groundwater flow. However, the relationship between floodplain inundation and changes in main stem discharge is not well understood due to the complexity of flow patterns and limited in situ observations of large wetland regions (Alsdorf, Bates, et al., 2007; Pavelsky & Smith, 2008). In high latitude wetlands such as the Yukon Flats, permafrost can further complicate these patterns by acting as a barrier between the surface and groundwater systems (Jepsen et al., 2013; Jorgenson & Osterkamp, 2005; Smith et al., 2005; 2007; Walvoord et al., 2012; Yoshikawa & Hinzman, 2003). While the summer 2016 Planet acquisitions lack sufficient temporal sampling to fully address these questions, the observed patterns nonetheless enable general characterization of floodplain connectivity across our Yukon Flats study area (Figures 2.8 and 2.9).

The divergent and spatially variable changes in lake surface area observed between 23 June and 17 August (Figure 2.7) suggest that surface water extent in the Yukon Flats is driven by a combination of the seasonal runoff cycle (i.e., spring snowmelt flooding and recharge, followed by summer drying), connections with the Yukon River main-stem, localized topography/bathymetry (Smith & Pavelsky, 2009) and substrate conditions (i.e., permafrost, geology). Previous analyses of hydrologic connectivity in other floodplain systems may help explain these patterns. While conceptual models commonly assume floodplains to have a uniform "bathtub" response to changing main-stem river stage, floodplain inundation is complex, driven by distributary channels, floodplain topography and storage in wetlands and lakes (Alsdorf, Bates, et al., 2007; Alsdorf et al., 2005). In their analysis of the relationship between lake levels and inundation extent in the Peace Athabaska Delta, Pavelsky and Smith (2008) find that water levels in the floodplain do not reflect water levels in the river. They observe a dichotomy between the distributary channel network and the surrounding lakes and wetlands wherein channels within the network respond to changes in river level but summertime peak flow events have little impact on the lakes and wetlands. In contrast, Alsdorf et al. (2005) present a diffusion model to explain how distance from the river channel controls the response of floodplain water levels to changes in main-stem river stage. Our findings do not support either a dichotomy between channel network and wetlands or a diffusion model; instead we observe larger scale variability wherein roughly one quarter of lakes respond to changes in river level, one half drain over the course of the season and one quarter are stable. The spatial patterns of this variability do not reveal any clear drivers of lake behavior (Figure 2.10). While a few lakes which respond strongly to August high stage events are clearly connected to the river system, in general there is no mechanism distinguishable in the imagery able to explain these differences. In their analysis of a flood-wave event in the Amazon basin, Alsdorf et al. (2007) observe a complex pattern of temporal changes in water level wherein variations in water height can be highly localized and the flow path cannot be predicted directly from bathymetry alone. Our observed patterns perhaps fit better with this result, where the spatiotemporal complexity of floodplain connectivity impedes characterizing or predicting individual lake response through a model or conceptual framework. An added contributor for the observed heterogeneity in lake area changes may be substrate geology, as recent work has shown lakes located farther from the floodplain, along permeable alluvial terraces or over coarser soils, are more likely to experience long-term shrinkage (Chen et al., 2014; Roach et al., 2011; 2013).

A regional mechanism for the observed pattern of stable and decreasing lakes co-existing in close proximity may be the influence of permafrost, which occurs discontinuously within our study area (Pastick et al., 2013). The presence of permafrost tends to impede infiltration of lake water to groundwater systems, plausibly contributing to lake stability in this area. Development of taliks (thaw bulbs) beneath lakes promotes infiltration, and permafrost research has identified through-talik formation and permafrost degradation around some lakes in the Yukon Flats (Jepsen et al., 2013; Minsley et al., 2012; Wellman et al., 2013). Lakes underlain by through-taliks are connected to the groundwater system, enabling water loss to the sub-surface (Jorgenson & Osterkamp, 2005; Walvoord & Kurylyk, 2016; Yoshikawa & Hinzman, 2003). The spatially heterogeneous patterns in surface water extent may thus be associated with discontinuous permafrost, though we observe no evidence of large lakes draining completely during the summer season.

In sum, we conclude that hydrologically connected lakes respond primarily to changing water levels in the main-stem Yukon River, whereas the sub-seasonal dynamics of other water bodies in the surrounding Yukon Flats wetlands are more complex, owing to a combination of intricate flow paths, underlying geology, and permafrost. According to the long-term (1951–2016) Yukon River discharge record at Eagle, the flow in 2016 was higher than average but well within normal variability, suggesting our observed results reflect sub-seasonal inundation patterns in wet years. Given the improving temporal frequency of Planet imagery, we anticipate future research can combine even denser time series of lake surface area with river discharge observations and maps of substrate geology and permafrost to improve scientific understanding of the controls on inundation in Arctic and sub-Arctic wetlands. Our observed variability further highlights that sub-seasonal patterns may obscure long-term trends in lake extent, the magnitude of which is often much smaller than sub-seasonal cycles driven by spring recharge, precipitation and late summer high discharge events (Plug et al., 2008; Rover et al., 2012). Considering the interest in understanding long-term temporal changes in surface water extent in the Yukon Flats (e.g. Anderson et al., 2013; Chen et al., 2014; Jepsen et al., 2013) and other high latitude environments (e.g. Prowse & Conly, 1998; Roach et al., 2011; 2013; Smith et al., 2005), this variability can critically impact reported trends in lake extent, especially when observed patterns are based on only a handful of images per year. We therefore also suggest that spatially heterogeneous intra-seasonal variability needs to be considered in long-term trend analyses.

5.3. Future Applications of Planet Imagery

5.3.1. Anticipated Growth in Planet CubeSat Image Acquisitions

Despite the limitations discussed here, the high temporal and spatial resolution of Planet imagery makes it a unique and valuable remote sensing resource. At the time of writing Planet currently operates 148 satellites in sun synchronous orbit, yielding <1 day revisit capacity globally. Owing to orbit convergence, imaging capacity is highest at high latitudes. Here, we simulated both revisit rate and the probability of cloud-free collection when all launched satellites have been phased into staggered sun synchronous orbit. When all satellites are operating at full capacity, the expected revisit time will be sub-daily at high latitudes, and the cloud-free collection probability for most high latitude locations is likely to be between one and three days (Figure 2.11). Planet plans to maintain a stable imaging capacity in sun synchronous orbits by regularly replenishing the constellation with new deployments.

5.3.2. Other Hydrological Applications

With daily or near-daily acquisitions, Planet CubeSat images therefore hold potential to substantially impact hydrologic research, for example in data assimilation, flood monitoring and prediction, and floodplain connectivity. Data assimilation is critical for driving hydrologic models and typically involves interpolating ground-based or remotely sensed observations to improve model performance, providing complete estimates of a poorly-measured geophysical parameter or organizing/removing valuable/redundant information (Reichle, 2008). For example, retrievals of surface water fraction and snow cover obtained from Planet CubeSat imagery could be assimilated into regional hydrologic models. Merging time-series of CubeSat inundation maps with water surface heights from satellite altimeters would create large-scale observations of surface water storage (Song et al., 2014). Finally, the fine spatial resolution and anticipated near-daily availability of Planet CubeSat data should facilitate downscaling of coarser resolution satellite observations for regional and local hydrologic models (Fluet-Chouinard et al., 2015). High frequency Planet CubeSat imagery should also prove valuable for refining and calibrating flood prediction models (Bates, 2012), and with near-time capability assist in disaster relief efforts (Joyce et al., 2009; Tralli et al., 2005).

Another clear application for Planet CubeSat imagery is remote estimation of river discharge from space. Deriving satellite retrievals of river discharge is an active research area within the hydrologic community, owing to the sparse network of in situ discharge gauges outside of the continental United States and Europe and the critical need for discharge measurements for global resource monitoring (Lettenmaier et al., 2015). A number of different methods have been developed to estimate discharge from optical satellite imagery, often building statistical relationships between river width/extent both with and without in situ measurements (Durand et al., 2016; Gleason et al., 2014; Gleason & Smith, 2014; Pavelsky, 2014; Smith, 1997; Tarpanelli et al., 2013). A major limitation of current remotely-sensed discharge estimates is the lack of sufficient temporal sampling of high resolution imagery due to revisit time or cloud cover (Pavelsky, 2014). While Planet imagery is still subject to cloud obscuration, its projected high imaging capabilities will enable more frequent cloud-free observations than traditional sensors and allow discharge estimation for more rivers than coarse-resolution MODIS.

Planet CubeSat imagery is particularly valuable at high latitudes where orbits converge, surface water is both dynamic and abundant, and in situ observations are sparse. Northern rivers are critical not only for Arctic ecosystems but also for the global climate system, as increasing runoff to the Arctic ocean can impact ocean circulation patterns (Peterson et al., 2002; White et al., 2007). However, rivers tend to be braided or anastomosing at these latitudes, making in situ monitoring especially difficult. Estimating discharge of large high latitude rivers such as the Yukon is therefore an obvious, critical application of Planet imagery. Planet imagery is also well-suited for mapping and tracking river ice breakup. Analyses of river ice breakup timing have typically relied on ground-based measurements (Magnuson et al., 2000; Smith, 2000) which do not enable understanding of how ice breakup progresses downstream through space and time. While satellite-based methods of identifying river ice breakup across entire river lengths have been developed, they are limited by the coarse resolution of daily available imagery (Cooley & Pavelsky, 2016; Pavelsky & Smith, 2004). Planet's 3–5 m resolution not only enables detection of river ice breakup at fine spatial scales, but the presence of minute-separated image pairs (due to orbital convergence at high latitudes) may allow ice tracking and therefore calculation of river velocity from space (Figure 2.12) (Beltaos & Kääb, 2014; Kääb & Prowse, 2011). Furthermore, the near-real time availability of Planet imagery provides large-scale observations of river ice breakup as it progresses downstream through remote areas and may therefore enable prediction of ice-jam flooding before it occurs, providing warning to communities located along northern rivers.

6. Conclusions

By providing near-daily high resolution imagery of large swaths of the world, Planet CubeSat imagery has the potential to transform many aspects of hydrologic remote sensing. The presented water fraction classification and object-based tracking approach performs well in both RapidEye and PlanetScope imagery, enabling tracking of sub-seasonal surface area changes in lakes and rivers, and identification of river-floodplain connections in a complex wetland environment. Other potential hydrological applications for near-daily, near real-time Planet data are numerous and include assimilation of inundation changes into hydrologic models, improvement of flood prediction models, estimation of river discharge from space, and studies of river ice breakup and flood hazards. To encourage scientific use of Planet CubeSat data, we recommend addressing the described limitations of automated cloud masking of Planet imagery, cross-sensor calibration and geolocation accuracy. With Planet imagery now available at sub-daily to weekly intervals globally, once these limitations are addressed, CubeSat imagery will be a valuable resource for studying dynamic water processes from space.

Acknowledgments

This research was funded by the NASA Terrestrial Ecology Program Arctic-Boreal Vulnerability Experiment (ABoVE) grant #NNX17AC60A. S. Cooley is also funded by a National Science Foundation Graduate Research Fellowship. Geospatial support for the WorldView data was provided by the Polar Geospatial Center under NSF OPP awards 1043681 & 1559691. We thank three anonymous reviewers for their constructive comments on this paper.

References

Alsdorf, D., Dunne, T., Melack, J., Smith, L., & Hess, L. (2005). Diffusion modeling of recessional flow on central Amazonian floodplains. *Geophysical Research Letters*, *32*(21), 1–4. https://doi.org/10.1029/2005GL024412

Alsdorf, D., Rodriguez, E., & Lettenmaier, D. P. (2007). Measuring surface water from space. *Reviews of Geophysics*, *45*(2), 1–24. https://doi.org/10.1029/2006RG000197.1.INTRODUCTION

Alsdorf, D., Bates, P., Melack, J., Wilson, M., & Dunne, T. (2007). Spatial and temporal complexity of the Amazon flood measured from space. *Geophysical Research Letters*, *34*(8), 1–5. https://doi.org/10.1029/2007GL029447

Anderson, L., Birks, J., Rover, J., & Guldager, N. (2013). Controls on recent Alaskan lake changes identified from water isotopes and remote sensing. *Geophysical Research Letters*, *40*(May 2013), 3413–3418. https://doi.org/10.1002/grl.50672

Ashmore, P., & Sauks, E. (2006). Prediction of discharge from water surface width in a braided river with implications for at-a-station hydraulic geometry. *Water Resources Research*, *42*(3), 1–11. https://doi.org/10.1029/2005WR003993

Bates, P. D. (2012). Integrating remote sensing data with flood inundation models: How far have we got? *Hydrological Processes*, *26*(16), 2515–2521. https://doi.org/10.1002/hyp.9374

Beltaos, S., & Kääb, A. (2014). Estimating river discharge during ice breakup from near-simultaneous satellite imagery. *Cold Regions Science and Technology*, *98*, 35–46. https://doi.org/10.1016/j.coldregions.2013.10.010

Chander, G., Markham, B. L., & Helder, D. L. (2009). Summary of current radiometric calibration coefficients for Landsat MSS, TM, ETM+, and EO-1 ALI sensors. *Remote Sensing of Environment*, *113*(5), 893–903. https://doi.org/10.1016/j.rse.2009.01.007

Chavez, P. S. (1988). An improved dark-object subtraction technique for atmospheric scattering correction of multispectral data. *Remote Sensing of Environment*, *24*(3), 459–479. https://doi.org/10.1016/0034-4257(88)90019-3

Chen, M., Rowland, J. C., Wilson, C. J., Altmann, G. L., & Brumby, S. P. (2014). Temporal and spatial pattern of thermokarst lake area changes at Yukon Flats, Alaska. *Hydrological Processes*, *28*(November 2012), 837–852. https://doi.org/10.1002/hyp.9642

Cooley, S. W., & Pavelsky, T. M. (2016). Spatial and temporal patterns in Arctic river ice breakup revealed by automated ice detection from MODIS imagery. *Remote Sensing of Environment*, *175*, 310–322. https://doi.org/10.1016/j.rse.2016.01.004

Durand, M., Gleason, C. J., Garabois, P. A., Bjerklie, D., Smith, L. C., Roux, H., et al. (2016). An intercomparison of remote sensing river discharge estimation algorithms from measurements of river height, width and slope, 7548–7555.

https://doi.org/10.1002/2016WR019285.Received

Emelyanova, I. V., McVicar, T. R., Van Niel, T. G., Li, L. T., & van Dijk, A. I. J. M. (2013). Assessing the accuracy of blending Landsat-MODIS surface reflectances in two landscapes with contrasting spatial and temporal dynamics: A framework for algorithm selection. *Remote Sensing of Environment*, *133*, 193–209. https://doi.org/10.1016/j.rse.2013.02.007

Fekete, B. M., Looser, U., Pietroniro, A., & Robarts, R. D. (2012). Rationale for Monitoring Discharge on the Ground. *Journal of Hydrometeorology*, *13*(6), 1977–1986. https://doi.org/10.1175/JHM-D-11-0126.1

Fluet-Chouinard, E., Lehner, B., Rebelo, L. M., Papa, F., & Hamilton, S. K. (2015). Development of a global inundation map at high spatial resolution from topographic downscaling of coarse-scale remote sensing data. *Remote Sensing of Environment*, *158*, 348–361. https://doi.org/10.1016/j.rse.2014.10.015

Gao, F., Masek, J., Schwaller, M., & Hall, F. (2006). On the blending of the landsat and MODIS surface reflectance: Predicting daily landsat surface reflectance. *IEEE Transactions on Geoscience and Remote Sensing*, *44*(8), 2207–2218. https://doi.org/10.1109/TGRS.2006.872081

Gleason, C. J., & Smith, L. C. (2014). Toward global mapping of river discharge using satellite images and at-many-stations hydraulic geometry. *Proceedings of the National Academy of Sciences*, *111*(13), 4788–4791. https://doi.org/10.1073/pnas.1317606111

Gleason, C. J., Smith, L. C., & Lee, J. (2014). Retrieval of river discharge solely from satellite imagery and at-many-stations hydraulic geometry: Sensitivity to river form and optimization parameters. *Water Resources Research*, *50*(12), 9604–9619. https://doi.org/10.1002/2014WR016109

Goulding, H. L., Prowse, T. D., & Beltaos, S. (2009). Spatial and temporal patterns of break-up and ice-jam flooding in the Mackenzie Delta, NWT Holly. *Hydrological Processes*, *23*, 2654–2670. https://doi.org/10.1002/hyp

Hall, D. K., Riggs, G. A., Salomonson, V. V, Digirolamo, N. E., & Bayr, K. J. (2002). MODIS snow-cover products, *83*, 181–194.

Helsel, D. R., & Hirsch, R. M. (1992). *Statistical Methods in Water Resources*. Amsterdam: Elsevier.

Houborg, R., & McCabe, M. F. (2016). High-Resolution NDVI from planet's constellation of earth observing nano-satellites: A new data source for precision agriculture. *Remote Sensing*, *8*(9). https://doi.org/10.3390/rs8090768

Jarihani, A. A., McVicar, T. R., van Niel, T. G., Emelyanova, I. V., Callow, J. N., & Johansen, K. (2014). Blending landsat and MODIS data to generate multispectral indices: A comparison of "index-then-blend" and "Blend-Then-Index" approaches. *Remote Sensing*, *6*(10), 9213–9238. https://doi.org/10.3390/rs6109213

Jawak, S. D., & Luis, A. J. (2014). A Semiautomatic Extraction of Antarctic Lake Features Using Worldview-2 Imagery, 33–46. https://doi.org/10.14358/PERS.80.10.000

Jepsen, S. M., Voss, C. I., Walvoord, M. A., Rose, J. R., Minsley, B. J., & Smith, B. D. (2013). Sensitivity analysis of lake mass balance in discontinuous permafrost: the example of disappearing Twelvemile Lake, Yukon Flats, Alaska (USA). *Hydrogeology Journal*, *21*(1), 185–200. https://doi.org/10.1007/s10040-012-0896-5

Jorgenson, M. T., & Osterkamp, T. E. (2005). Response of boreal ecosystems to varying modes of permafrost degradation. *Canadian Journal of Forest Research*, *35*(9), 2100–2111. https://doi.org/10.1139/x05-153

Jorgenson, M. T., Yoshikawa, K., Kanevskiy, M., Shur, Y., Romanovsky, V. E., Marchenko, S., et al. (2008). Permafrost characteristics of Alaska (map). Institute of Northern Engineering, Univ. Alaska, Fairbanks, AK.

Joyce, K. E., Belliss, S. E., Samsonov, S. V., McNeill, S. J., & Glassey, P. J. (2009). A review of the status of satellite remote sensing and image processing techniques for mapping natural hazards and disasters. *Progress in Physical Geography*, *33*(2), 183–207. https://doi.org/10.1177/0309133309339563

Kääb, a., & Prowse, T. (2011). Cold-regions river flow observed from space. *Geophysical Research Letters*, *38*, 1–5. https://doi.org/10.1029/2011GL047022

Lehner, B., & Döll, P. (2004). Development and validation of a global database of lakes, reservoirs and wetlands. *Journal of Hydrology*, *296*(1–4), 1–22. https://doi.org/10.1016/j.jhydrol.2004.03.028

Lesack, L. F. W., Marsh, P., Hicks, F. E., & Forbes, D. L. (2013). Timing, duration, and magnitude of peak annual water-levels during ice breakup in the Mackenzie Delta and the role of river discharge. *Water Resources Research*, *49*, 8234–8249. https://doi.org/10.1002/2012WR013198

Lettenmaier, D. P., Alsdorf, D., Dozier, J., Huffman, G. J., Pan, M., & Wood, E. F. (2015). Water Resources Research, 7309–7342. https://doi.org/10.1002/2015WR017616.Received

Magnuson, J., Robertson, D., Benson, B., Wynne, R., Livingstone, D., Arai, T., et al. (2000). Historical trends in lake and river ice cover in the northern hemisphere. *Science*, *289*, 1743–6. https://doi.org/10.1126/science.289.5485.1743

Markham, B., Barsi, J., Kvaran, G., Ong, L., Kaita, E., Biggar, S., et al. (2014). Landsat-8 operational land imager radiometric calibration and stability. *Remote Sensing*, *6*(12), 12275–12308. https://doi.org/10.3390/rs61212275

Markham, B. L., & Barker, J. L. (1987). Radiometric properties of U.S. processed landsat MSS data. *Remote Sensing of Environment*, *22*(1), 39–71. https://doi.org/10.1016/0034-4257(87)90027-7

Marsh, P., & Lesack, L. F. W. (1996). The hydrologic regime of perched lakes in the Mackenzie Delta: Potential responses to climate change. *Limnology and Oceanography*, *41*(5), 849–856. https://doi.org/10.4319/lo.1996.41.5.0849

McCabe, M. R., Alsdorf, D. E., Miralles, D. G., Uijlenhoet, R., Wagner, W., Lucieer, A., et al. (2017). The Future of Earth Observation in Hydrology. Hydrology and Earth System Sciences (under review). *Hydrology and Earth System Sciences (under Review)*, 3879–3914.

McCullough, I. M., Loftin, C. S., & Sader, S. A. (2012). High-frequency remote monitoring of large lakes with MODIS 500m imagery. *Remote Sensing of Environment*, *124*(November 2011), 234–241. https://doi.org/10.1016/j.rse.2012.05.018

McFEETERS, S. K. (1996). The use of the Normalized Difference Water Index (NDWI) in the delineation of open water features. *International Journal of Remote Sensing*, *17*(7), 1425–1432. https://doi.org/10.1080/01431169608948714

Minsley, B. J., Abraham, J. D., Smith, B. D., Cannia, J. C., Voss, C. I., Jorgenson, M. T., et al. (2012). Airborne electromagnetic imaging of discontinuous permafrost. *Geophysical Research Letters*, *39*(2), 1–8. https://doi.org/10.1029/2011GL050079

Naughton, D. (2011). Absolute radiometric calibration of the RapidEye multispectral imager using the reflectance-based vicarious calibration method. *Journal of Applied Remote Sensing*, *5*(1), 53544. https://doi.org/10.1117/1.3613950

Olthof, I., Fraser, R. H., & Schmitt, C. (2015). Landsat-based mapping of thermokarst lake dynamics on the Tuktoyaktuk Coastal Plain, Northwest Territories, Canada since 1985. *Remote Sensing of Environment*, *168*, 194–204. https://doi.org/http://dx.doi.org/10.1016/j.rse.2015.07.001

Otsu, N. (1979). A Threshold Selection Method from Gray-Level Histograms. *IEEE Transactions on Systems, Man, and Cybernetics*, *9*(1), 62–66. https://doi.org/10.1109/TSMC.1979.4310076

Pastick, N. J., Jorgenson, M. T., Wylie, B. K., Minsley, B. J., Ji, L., Walvoord, M. A., et al. (2013). Extending airborne electromagnetic surveys for regional active layer and permafrost mapping with Remote Sensing and Ancillary Data, Yukon Flats Ecoregion, Central Alaska. *Permafrost and Periglacial Processes*, *24*(3), 184–199. https://doi.org/10.1002/ppp.1775

Pavelsky, T. M. (2014). Using width-based rating curves from spatially discontinuous satellite imagery to monitor river discharge. *Hydrological Processes*, *28*(6), 3035–3040. https://doi.org/10.1002/hyp.10157

Pavelsky, T. M., & Smith, L. C. (2004). Spatial and temporal patterns in Arctic river ice breakup observed with MODIS and AVHRR time series. *Remote Sensing of Environment*, *93*, 328–338. https://doi.org/10.1016/j.rse.2004.07.018

Pavelsky, T. M., & Smith, L. C. (2008). Remote sensing of hydrologic recharge in the Peace-

Athabasca Delta, Canada. *Geophysical Research Letters*, *35*(8), 1–5. https://doi.org/10.1029/2008GL033268

Pekel, J.-F., Cottam, A., Gorelick, N., & Belward, A. S. (2016). High-resolution mapping of global surface water and its long-term changes. *Nature*, *540*(7633), 418–422. https://doi.org/10.1038/nature20584

Peterson, B. J., Holmes, R. M., McClelland, J. W., Vörösmarty, C. J., Lammers, R. B., Shiklomanov, A. I., et al. (2002). Increasing river discharge to the Arctic Ocean. *Science*, *298*(December), 2171–2173. https://doi.org/10.1126/science.1077445

Planet Team. (2018). Planet Application Program Interface: In Space for Life on Earth. San Francisco, CA. Retrieved from https://api.planet.com

Plug, L. J., Walls, C., & Scott, B. M. (2008). Tundra lake changes from 1978 to 2001 on the Tuktoyaktuk Peninsula, western Canadian Arctic. *Geophysical Research Letters*, *35*(December 2007), L03502. https://doi.org/10.1029/2007GL032303

Prowse, T. D., & Conly, F. M. (1998). Effects of climatic variability and flow regulation on ice-jam flooding of a northern delta, *1610*(March), 1589–1610.

Reichle, R. H. (2008). Data assimilation methods in the Earth sciences. *Advances in Water Resources*, *31*(11), 1411–1418. https://doi.org/10.1016/j.advwatres.2008.01.001

Riordan, B., Verbyla, D., & McGuire, a. D. (2006). Shrinking ponds in subarctic Alaska based on 1950-2002 remotely sensed images. *Journal of Geophysical Research: Biogeosciences*, *111*(December 2005), G04002. https://doi.org/10.1029/2005JG000150

Roach, J., Griffith, B., Verbyla, D., & Jones, J. (2011). Mechanisms influencing changes in lake area in Alaskan boreal forest. *Global Change Biology*, *17*, 2567–2583. https://doi.org/10.1111/j.1365-2486.2011.02446.x

Roach, J. K., Griffith, B., & Verbyla, D. (2013). Landscape influences on climate-related lake shrinkage at high latitudes. *Global Change Biology*, *19*, 2276–2284. https://doi.org/10.1111/gcb.12196

Rover, J., Ji, L., Wylie, B. K., & Tieszen, L. L. (2012). Establishing water body areal extent trends in interior Alaska from multi-temporal Landsat data. *Remote Sensing Letters*, *3*(January), 595–604. https://doi.org/10.1080/01431161.2011.643507

Shiklomanov, A. I., Lammers, R. B., & Vorosmarty, C. J. (2002). Widespread decline in hydrological monitoring threatens pan-Arctic research. *EOS*, *83*(2).

Smith, L. C. (2000). Trends in Russian Arctic river-ice formation and breakup, 1917 to 1994. *Physical Geography*.

Smith, L. C., & Pavelsky, T. M. (2008). Estimation of river discharge, propagation speed, and hydraulic geometry from space: Lena River, Siberia. *Water Resources Research*, *44*(3), 1–

11. https://doi.org/10.1029/2007WR006133

Smith, L. C., & Pavelsky, T. M. (2009). Remote sensing of volumetric storage changes in lakes. *Earth Surface Processes and Landforms*, *34*, 1343–1358. https://doi.org/10.1002/esp

Smith, L. C., Isacks, B. L., Forster, R. R., Bloom, A. L., & Preuss, I. (1995). Estimation of Discharge From Braided Glacial Rivers Using ERS 1 Synthetic Aperture Radar: First Results. *Water Resources Research*, *31*(5), 1325–1329. https://doi.org/10.1029/95WR00145

Smith, L. C., Isacks, B., Bloom, A., & Murray, A. B. (1996). Estimation of discharge from three braided rivers using synthetic aperture radar satellite imagery: Potential application to ungauged basins. *Water Resources Research*, *32*(7), 2021–2034. https://doi.org/10.1029/96WR00752

Smith, L. C., Sheng, Y., MacDonald, G. M., & Hinzman, L. D. (2005). Disappearing Arctic lakes. *Science (New York, N.Y.)*, *308*, 1429. https://doi.org/10.1126/science.1108142

Smith, L. C., Sheng, Y., & MacDonald, G. M. (2007). A First Pan-Arctic Assessment of the Influence of Glaciation, Permafrost, Topography and Peatlands on Northern Hemisphere Lake Distribution. *Permafrost and Periglacial Processes*, *18*, 2910297. https://doi.org/10.1002/ppp.581

Smith, L. C. (1997). Satellite remote sensing of river inundation area, stage, and discharge: a review. *Hydrological Processes*, *11*(10), 1427–1439. https://doi.org/10.1002/(SICI)1099-1085(199708)11:10<1427::AID-HYP473>3.0.CO;2-S

Song, C., Woodcock, C. E., Seto, K. C., Lenney, M. P., & Macomber, S. A. (2001). Classification and change detection using Landsat TM data: When and how to correct atmospheric effects? *Remote Sensing of Environment*, *75*(2), 230–244. https://doi.org/10.1016/S0034-4257(00)00169-3

Song, C., Huang, B., & Ke, L. (2014). Inter-annual changes of alpine inland lake water storage on the Tibetan Plateau: Detection and analysis by integrating satellite altimetry and optical imagery. *Hydrological Processes*, *28*(4), 2411–2418. https://doi.org/10.1002/hyp.9798

Tarpanelli, A., Brocca, L., Lacava, T., Melone, F., Moramarco, T., Faruolo, M., et al. (2013). Toward the estimation of river discharge variations using MODIS data in ungauged basins. *Remote Sensing of Environment*, *136*, 47–55. https://doi.org/10.1016/j.rse.2013.04.010

Tralli, D. M., Blom, R. G., Zlotnicki, V., Donnellan, A., & Evans, D. L. (2005). Satellite remote sensing of earthquake, volcano, flood, landslide and coastal inundation hazards. *ISPRS Journal of Photogrammetry and Remote Sensing*, *59*(4), 185–198. https://doi.org/10.1016/j.isprsjprs.2005.02.002

Tseng, D.-C., Tseng, H.-T., & Chien, C.-L. (2008). Automatic cloud removal from multi-temporal SPOT images. *Applied Mathematics and Computation*, *205*(2), 584–600. https://doi.org/10.1016/j.amc.2008.05.050

Walvoord, M. A., & Kurylyk, B. L. (2016). Hydrologic Impacts of Thawing Permafrost—A Review. *Vadose Zone Journal*, *15*(6), 0. https://doi.org/10.2136/vzj2016.01.0010

Walvoord, M. A., Voss, C. I., & Wellman, T. P. (2012). Influence of permafrost distribution on groundwater flow in the context of climate-driven permafrost thaw: Example from Yukon Flats Basin, Alaska, United States. *Water Resources Research*, *48*(7), 1–17. https://doi.org/10.1029/2011WR011595

Wellman, T. P., Voss, C. I., & Walvoord, M. A. (2013). Impacts of climate, lake size, and supra- and sub-permafrost groundwater flow on lake-talik evolution, Yukon Flats, Alaska (USA). *Hydrogeology Journal*, *21*(1), 281–298. https://doi.org/10.1007/s10040-012-0941-4

White, D., Hinzman, L., Alessa, L., Cassano, J., Chambers, M., Falkner, K., et al. (2007). The arctic freshwater system: Changes and impacts. *Journal of Geophysical Research: Biogeosciences*, *112*(4), 1–21. https://doi.org/10.1029/2006JGO00353

Wilson, N., Greenberg, J., Jumpasut, A., Collison, A., & Weichelt, H. (2017). *Absolute Radiometric Calibration of Planet Dove Satellites , Flocks 2p & 2e*. Planet.

Wolf, A. F. (2012). Using WorldView-2 Vis-NIR multispectral imagery to support land mapping and feature extraction using normalized difference index ratios, 83900N–83900N–8. https://doi.org/10.1117/12.917717

Yoshikawa, K., & Hinzman, L. D. (2003). Shrinking thermokarst ponds and groundwater dynamics in discontinuous permafrost near Council, Alaska. *Permafrost and Periglacial Processes*, *14*(January 2016), 151–160. https://doi.org/10.1002/ppp.451

Figures

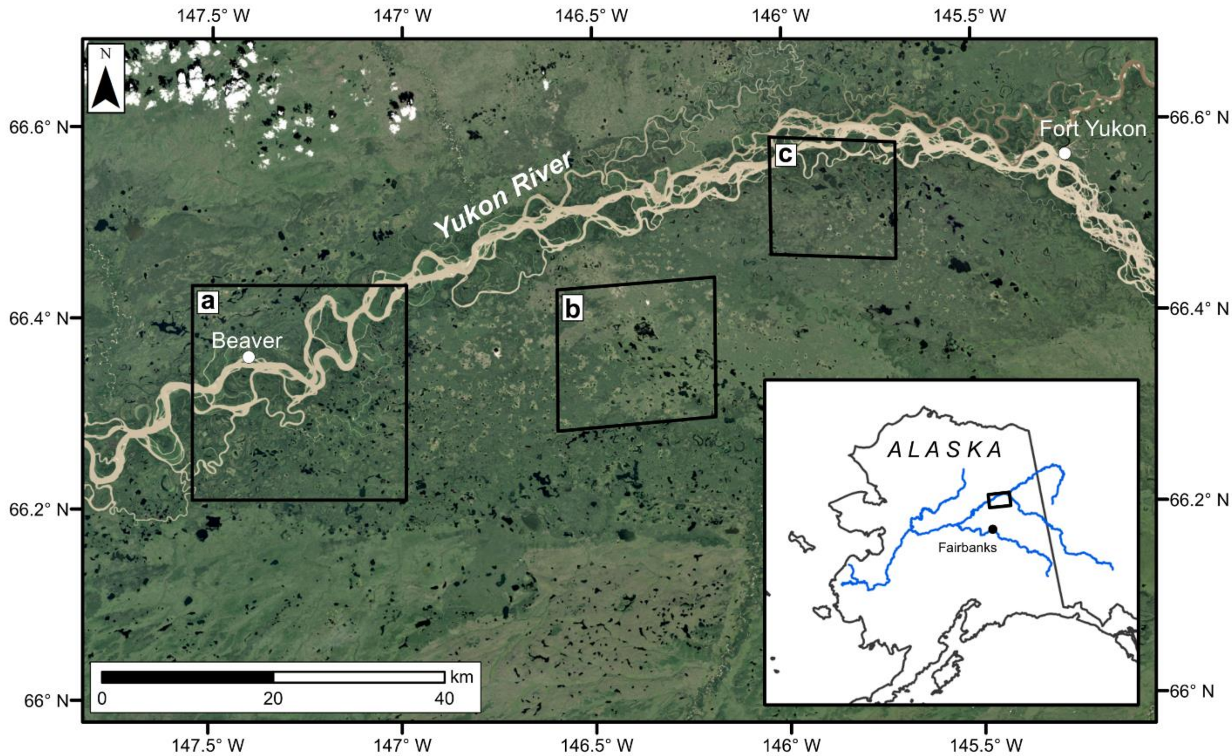

Figure 2.1. Map of the Yukon Flats, Alaska. Box (a) is the primary study area (Planet tile No. 669714); (b,c) are the location of concurrent WorldView/Planet images used to validate our lake extraction method. Background is an RGB Landsat-8 image from 12 July 2016. Inset shows location within Alaska.

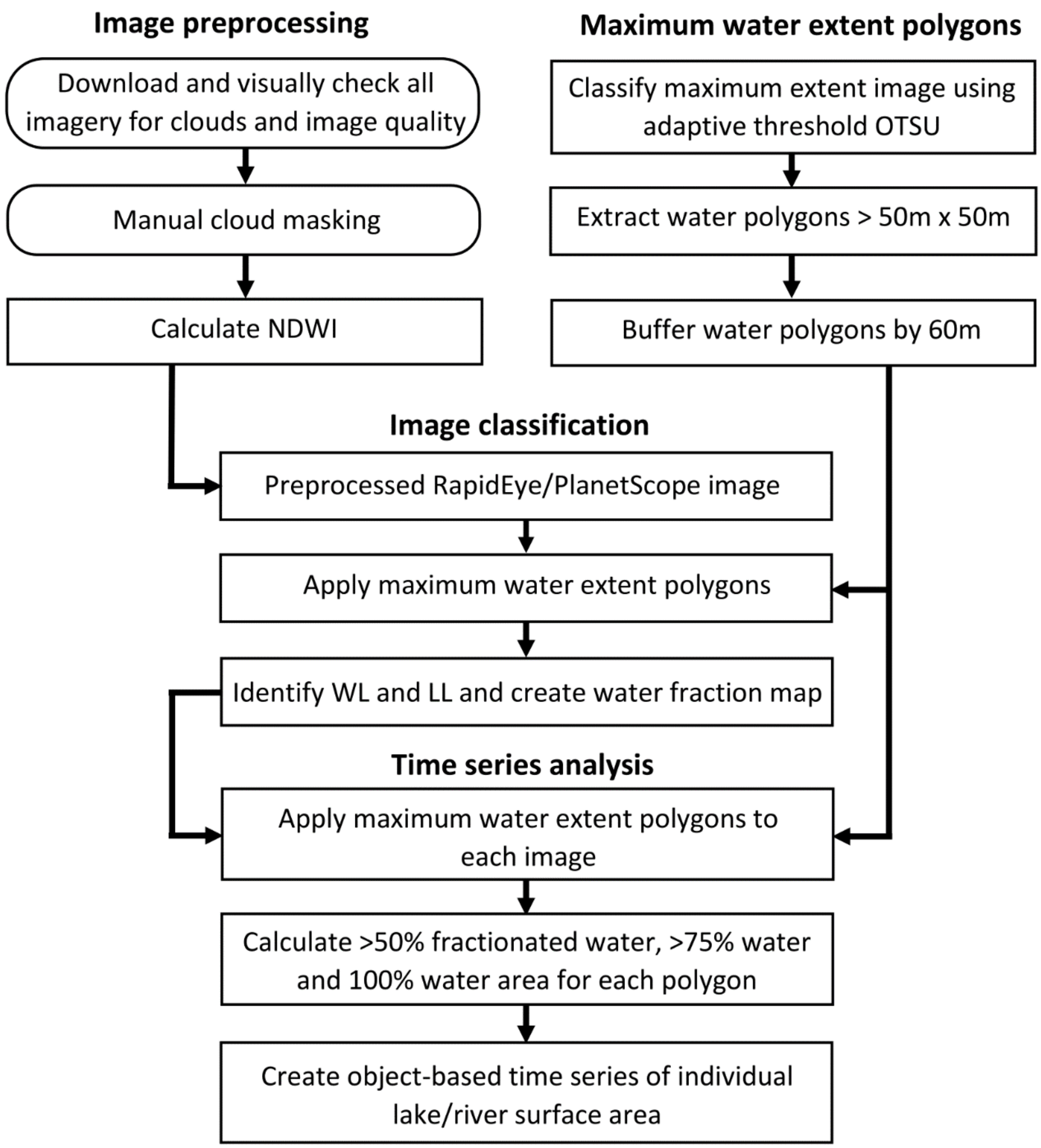

Figure 2.2. Water fraction classification workflow for Planet imagery. Rounded boxes represent manual steps and rectangles are fully automated steps.

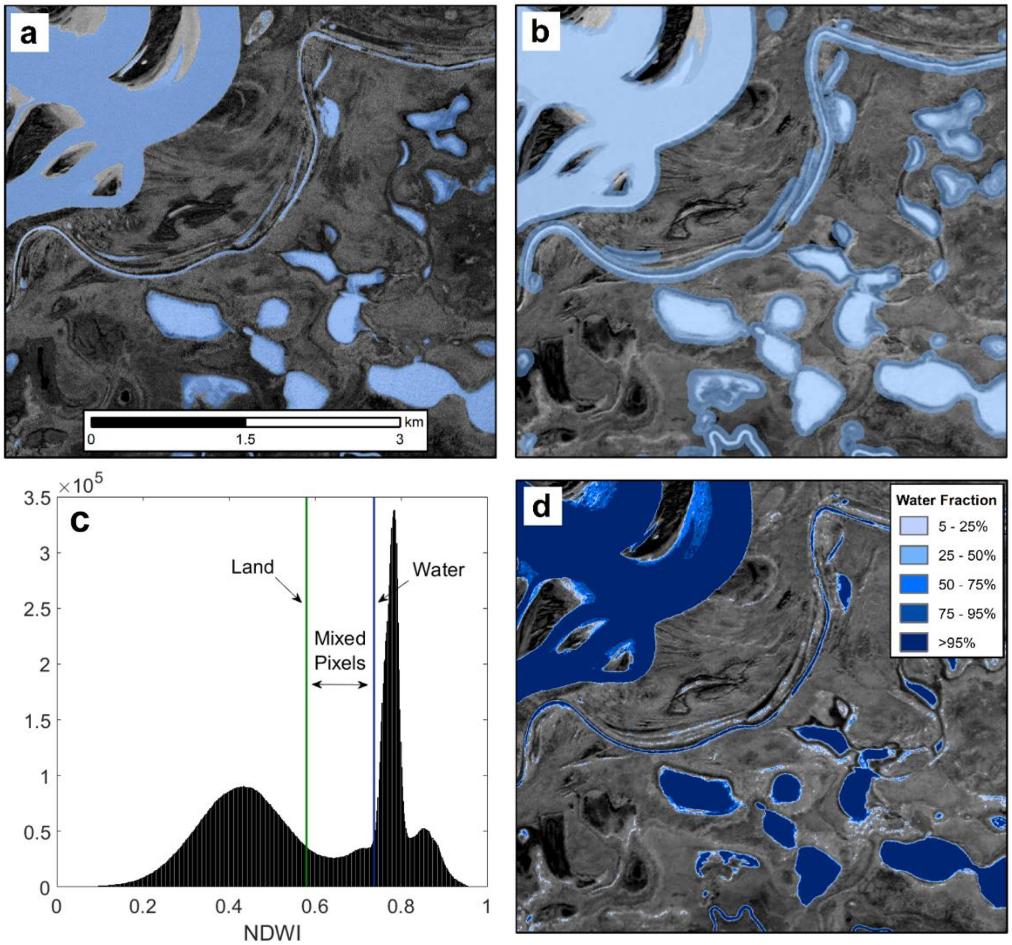

Figure 2.3. Demonstration of classification method: (**a**) the initial adaptive OTSU classification; (**b**) the buffered maximum lake polygons; (**c**) the histogram classification from the buffered lake polygons with land level (*LL*) and water level (*WL*) labeled; (**d**) the final water fraction map generated by applying the land and water levels to the NDWI image.

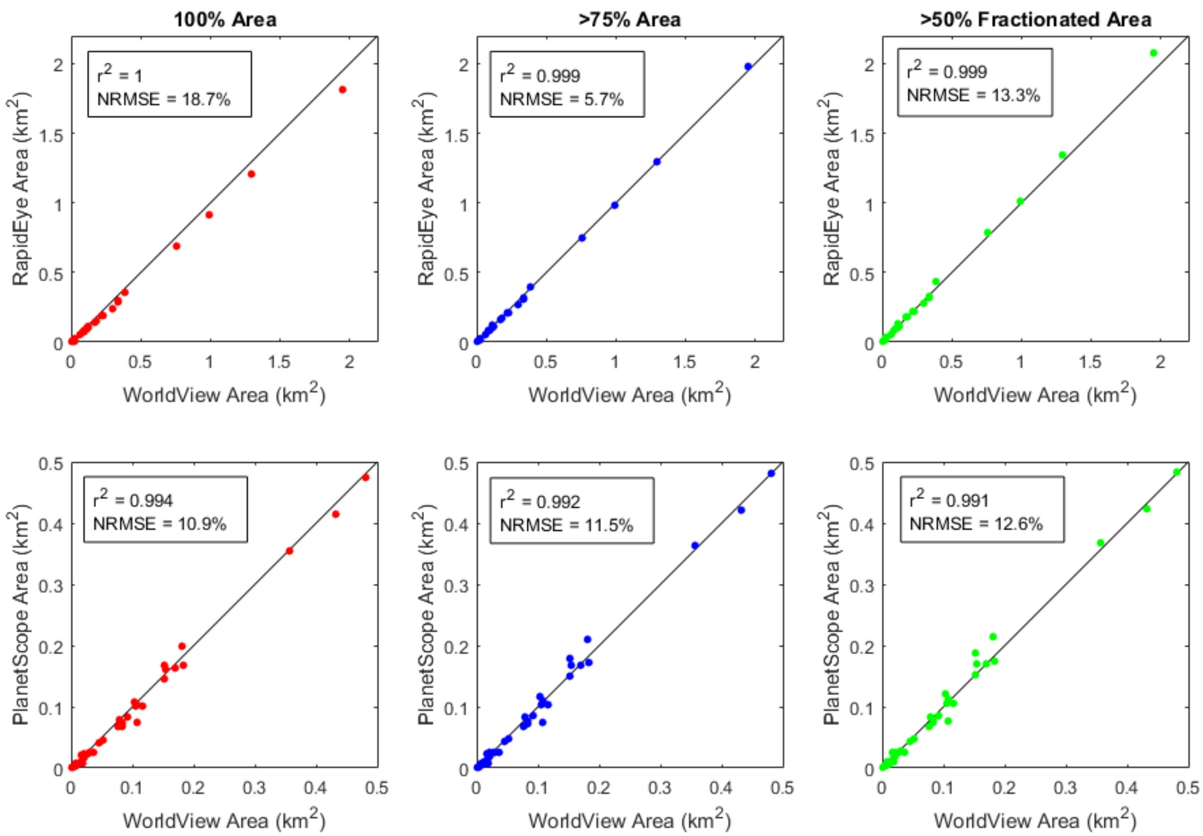

Figure 2.4. RapidEye (**top row**) and PlanetScope (**bottom row**) lake area vs. manually delineated WorldView lake area. Column 1 shows 100% water area, column 2 shows >75% water area and column 3 shows >50% fractionated area.

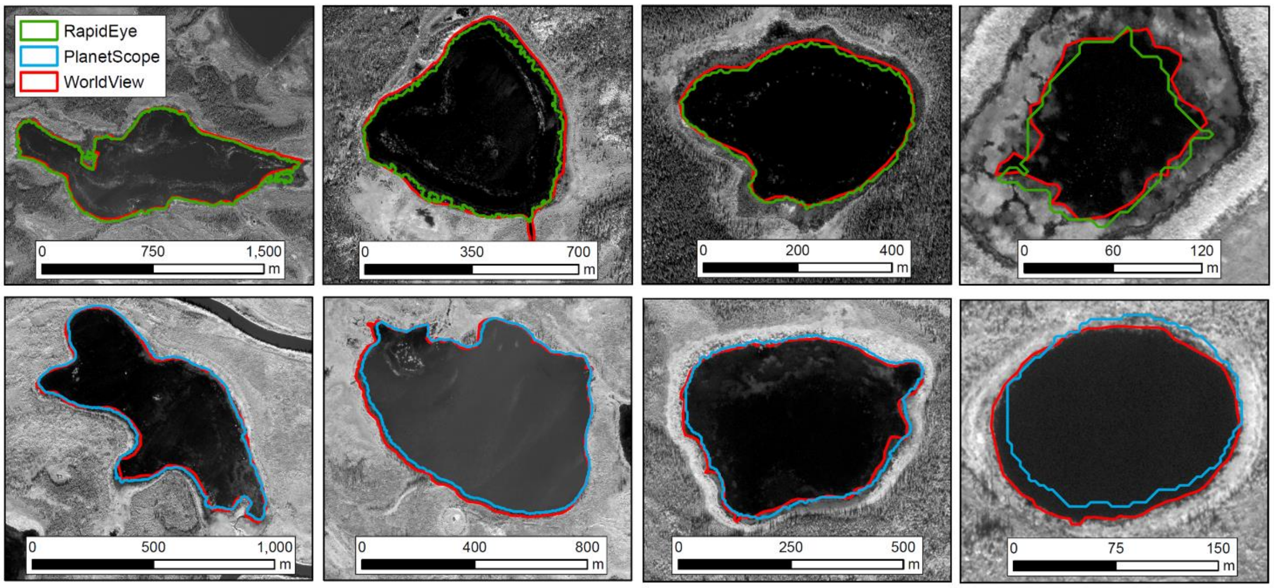

Figure 2.5. Lake shorelines delineated from PlanetScope (blue), RapidEye (green) and WorldView (red) imagery. PlanetScope and RapidEye shorelines shown represent automated extraction of >75% water area. WorldView shorelines are manually delineated. Imagery © 2016, DigitalGlobe, Inc.

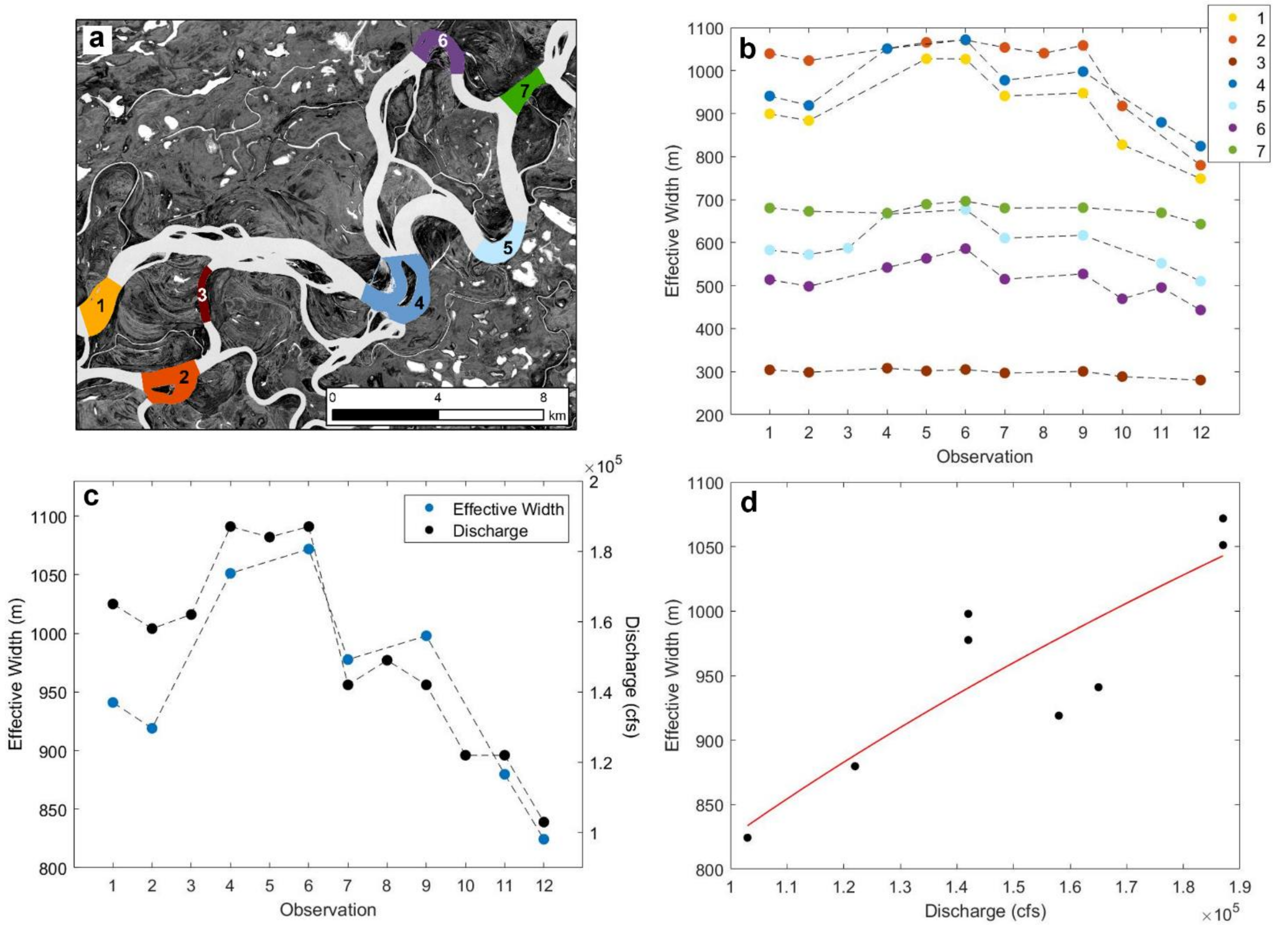

Figure 2.6. (**a**) Map of seven river reach segments and (**b**) time series of corresponding river effective width. Color and number of time series in (**a**) corresponds to color and number of reach in (**b**); (**c**) Time series of effective width for river reach #4 and corresponding Yukon river discharge at Eagle and (**d**) scatter between effective width and Yukon river discharge (Q) at Eagle The equation of the best fit curve in panel (**d**) (shown in red) is $W_e = 10.9Q^{0.38}$ ($R^2 = 0.75$).

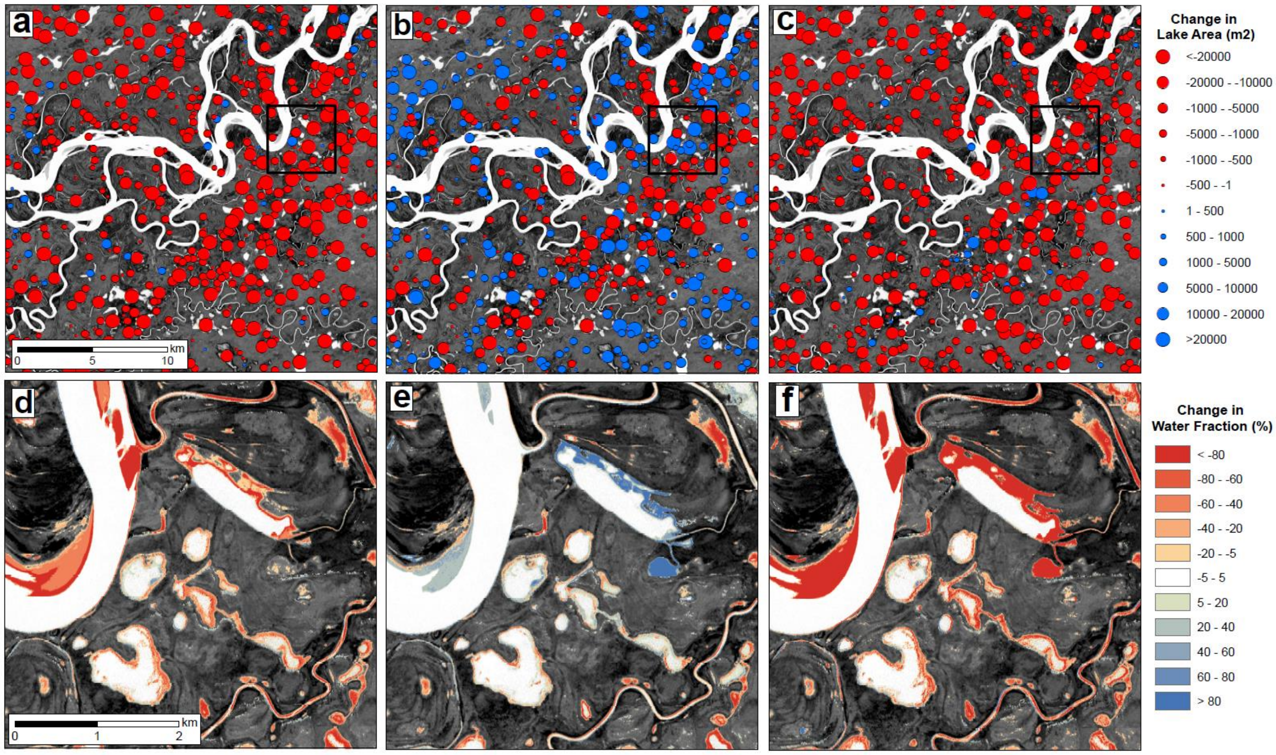

Figure 2.7. Changes in lake surface areas between (column 1, (**a**,**d**)) 23 June and 1 October, (column 2, (**b**,**e**)) 23 June and 17 August and (column 3, (**c**,**f**)) 17 August and 1 October. In the top row individual water bodies are represented as circles with the sizes of the circles scaled by the area of the change. Bottom row shows the pixel-based change in water fraction. Location of inset shown in top row. Red represents water loss, blue represents water gain.

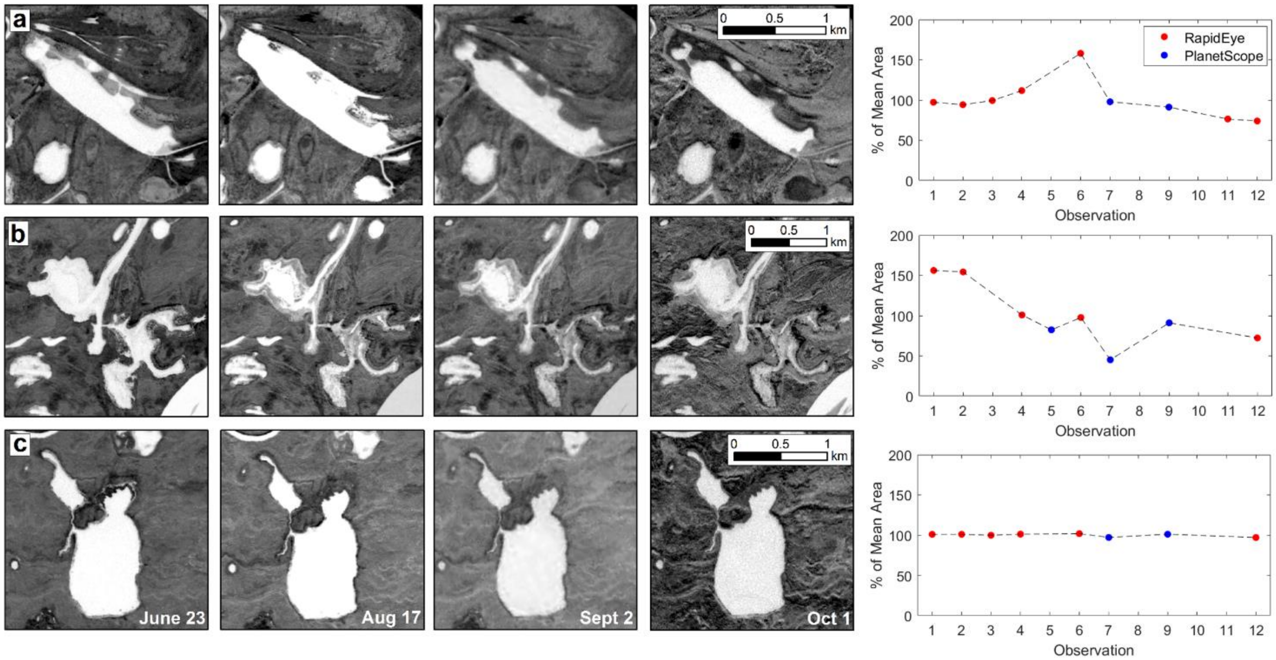

Figure 2.8. Examples of lake area time series categorized as: (**a**) connected; (**b**) disconnected and (**c**) stable. The time series of lake area is shown on the right. Column 1 is NDWI imagery from 6/23 (observation 1), column 2 from 8/17 (observation 5), column 3 from 9/02 (observation 9) and column 4 from 10/01 (observation 12).

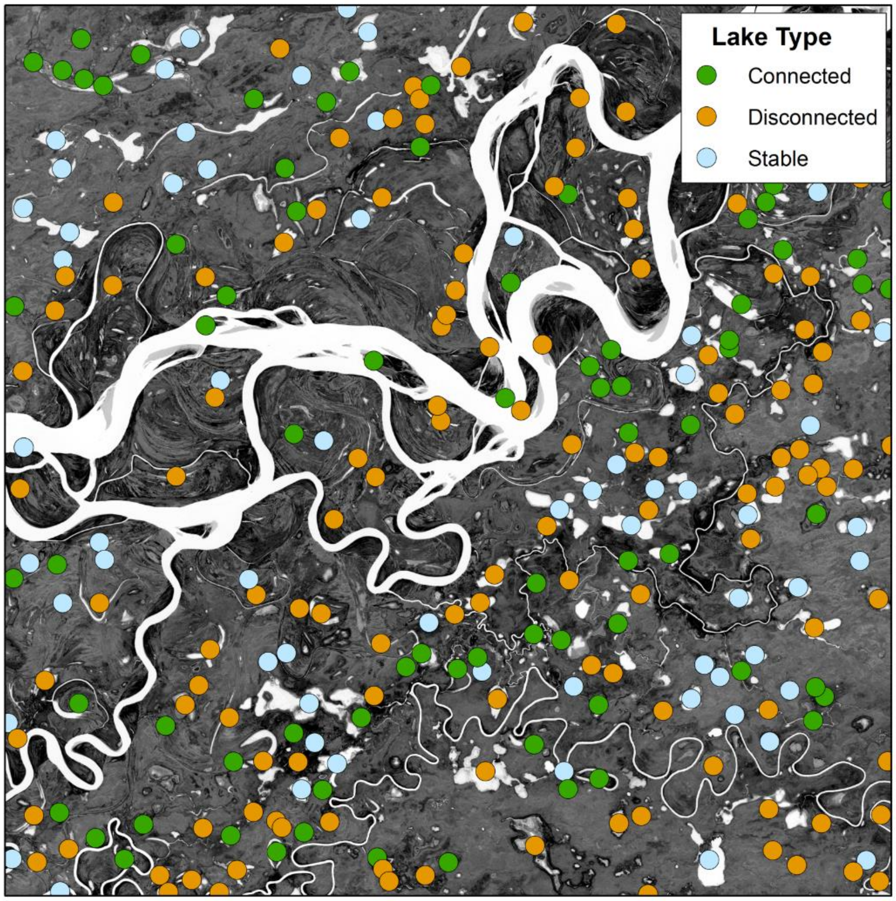

Figure 2.9. Temporal correlation between Planet time series of lake surface area and Yukon River discharge reveal connected (green), disconnected (orange) and stable (light blue) lakes. Green dots are connected lakes (surface area standard deviation >10%, correlated to Yukon river discharge at $p < 0.1$), orange are disconnected (surface area std >10%, not correlated to Yukon river discharge) and light blue are stable (surface area std <10%).

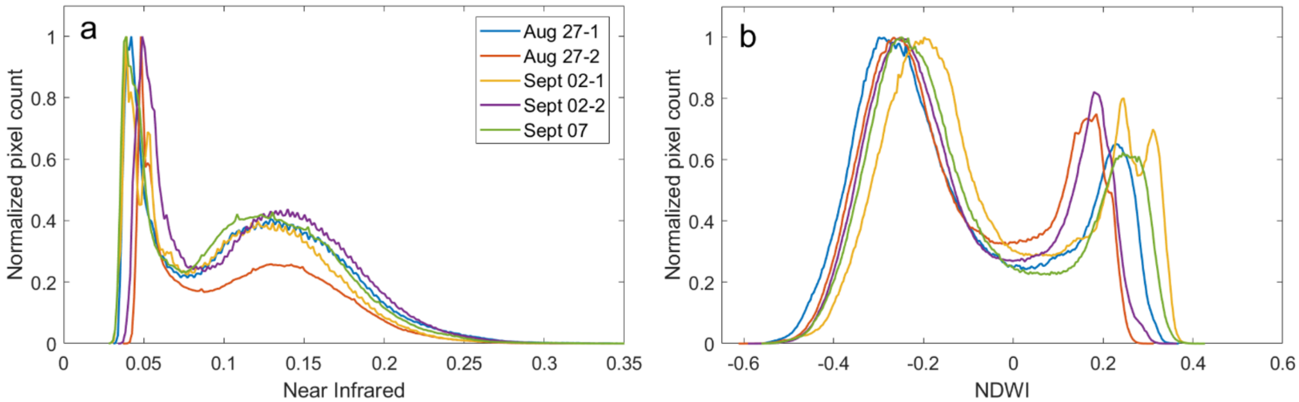

Figure 2.10. Normalized distribution of (**a**) top of atmosphere near infrared reflectance and (**b**) NDWI for Yukon Flats water bodies and surrounding vegetation in five different PlanetScope images. In the near infrared (**a**), water pixels are the left peak (lower band values) and in the NDWI (**b**), the second peak represents water pixels.

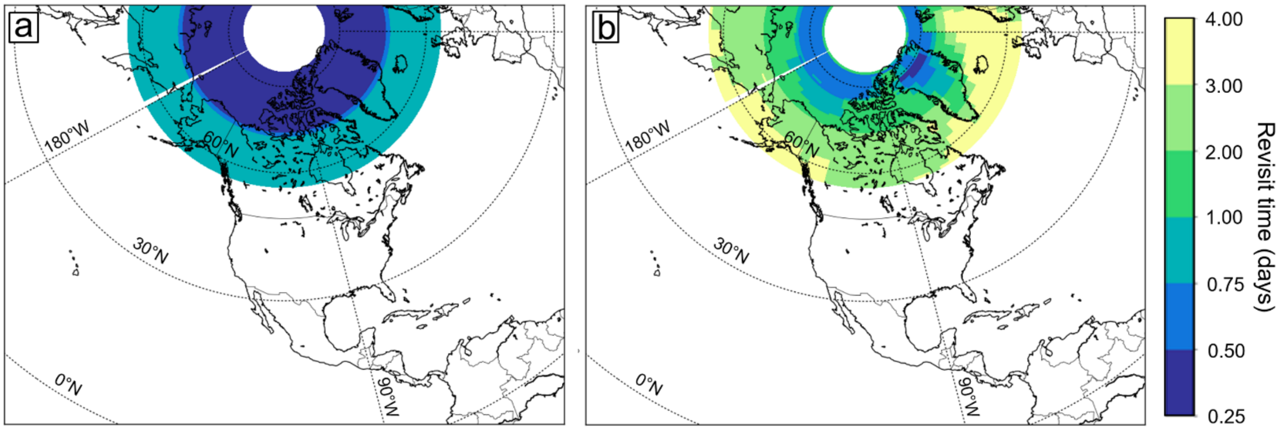

Figure 2.11. (**a**) Geometric revisit time and (**b**) average time in days between cloud-free revisits for PlanetScope imagery north of 55° N when satellite constellation is at full operational capacity.

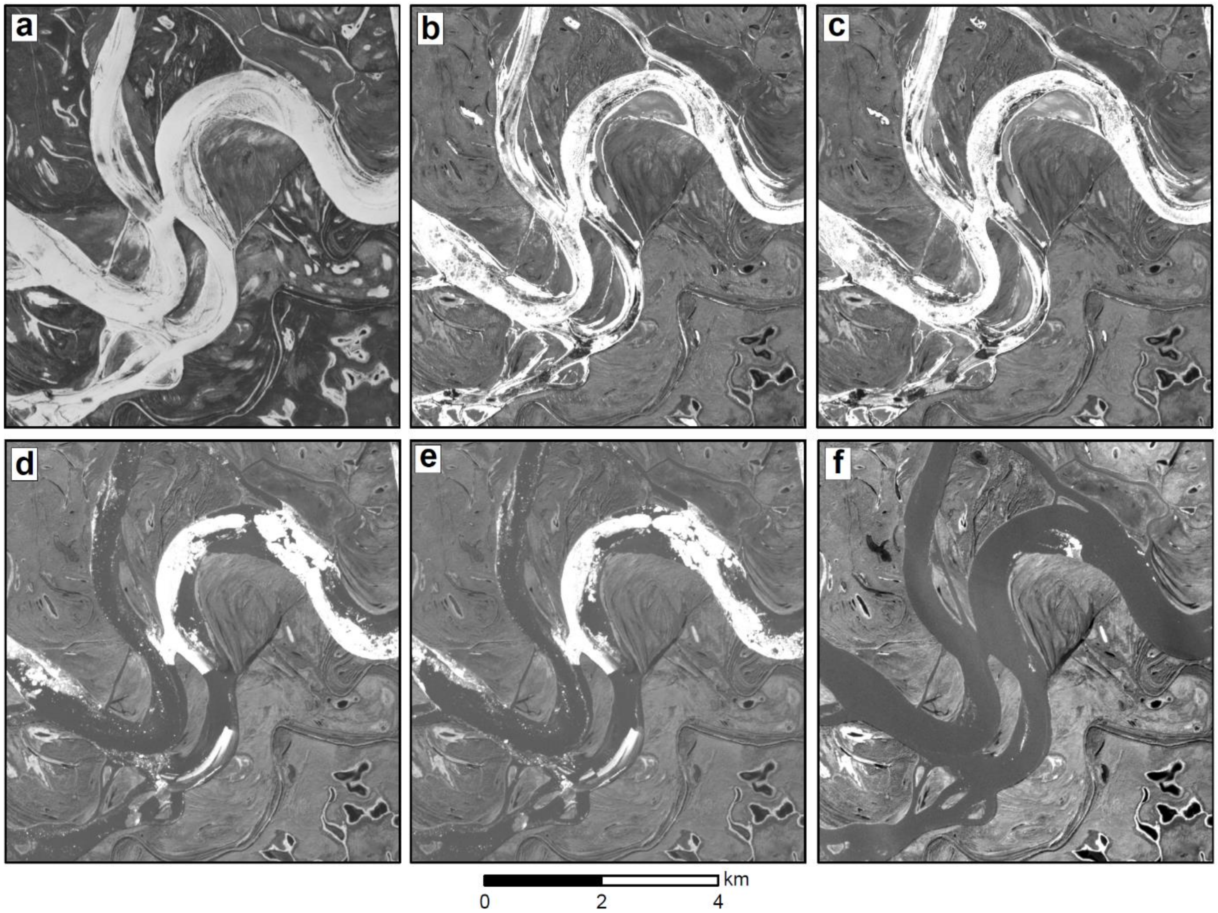

Figure 2.12. Time series of river ice breakup on the Yukon shown in the near infrared band of PlanetScope imagery. Panels show (**a**) 2 May, (**b**) 6 May, (**c**) 7 May, (**d**) 12 May, (**e**) 12 May (7 min later) and (**f**) 15 May.

Tables

Table 2.1. Specifications of the three satellite sensors operated by Planet. Information is correct as of December 2017.

Sensor	Number of Satellites	Bands	Spatial Resolution	Temporal Resolution
RapidEye	5	5 (Blue, Green, Red, Far-Red, NIR)	6.5 m	~5.5 days
PlanetScope	~170	4 (Blue, Green, Red, NIR)	3.7 m	Daily
SkySat	13	4 (Blue, Green, Red, NIR)	0.8 m	Variable, with multiple opportunities per day

Table 2.2. List of images.

Image ID	Sensor	Date	Observation
20160623_220215_669714_RapidEye-4	RapidEye	23 June	1
20160624_220552_669714_RapidEye-5	RapidEye	24 June	2
20160725_215412_669714_RapidEye-3	RapidEye	25 July	3
20160813_215232_669714_RapidEye-3	RapidEye	13 August	4
222535_0669714_2016-08-16_0e0d	PlanetScope	16 August	5
20160817_220351_669714_RapidEye-2	RapidEye	17 August	6
229647_0669714_2016-08-27_0e14	PlanetScope	27 August	7
229821_0669714_2016-08-27_0e20	PlanetScope	27 August	7
20160901_215044_669714_RapidEye-3	RapidEye	1 September	8
232753_0669714_2016-09-02_0e19	PlanetScope	2 September	9
232785_0669714_2016-09-02_0e30	PlanetScope	2 September	9
20160907_215525_669714_RapidEye-4	RapidEye	7 September	10
236414_0669714_2016-09-07_0e26	PlanetScope	7 September	11
20161001_215759_669714_RapidEye-4	RapidEye	1 October	12
234040_0669715_2016-09-02_0e0e	PlanetScope	2 September	Validation
234040_0669716_2016-09-02_0e0e	PlanetScope	2 September	Validation
238490_0669716_2016-09-02_0e26	PlanetScope	2 September	Validation
20160908_215904_669817_RapidEye-5	RapidEye	8 September	Validation
20160908_215905_669816_RapidEye-5	RapidEye	8 September	Validation
WV02_20160830213545_103001005A6E6600 _16AUG30213545-P1BS	WorldView-2	30 August	Validation
WV03_20160908220049_1040010021B5F000_ 16SEP08220049-P1BS	WorldView-3	8 August	Validation
WV03_20160908220050_1040010021B5F000_ 16SEP08220050-P1BS	WorldView-3	8 August	Validation

CHAPTER 3

Arctic-Boreal Lake Dynamics Revealed using CubeSat Imagery

Sarah W. Cooley[1,2*], Laurence C. Smith[3], Jonathan C. Ryan[2], Lincoln H. Pitcher[3] and Tamlin M. Pavelsky[4]

[1]Department of Earth, Environmental and Planetary Sciences, Brown University, Providence, Rhode Island, USA, 02912

[2]Institute at Brown for the Environment and Society, Brown University, Providence, Rhode Island, USA, 02912

[3]Department of Geography, University of California, Los Angeles, California, 90095

[4]Department of Geological Sciences, University of North Carolina at Chapel Hill, North Carolina, USA, 27599.

Published in *Geophysical Research Letters*

Citation: Cooley, S.W., Smith, L.C., Ryan, J.C., Pitcher, L.H and Pavelsky, T.M. (2019), Arctic-Boreal lake dynamics revealed using CubeSat imagery, *Geophysical Research Letters,* 46, https://doi.org/10.1029/2018GL081584

Abstract

Fine scale, sub-seasonal fluctuations in Arctic-Boreal surface water reflect regional water balance and modulate trace gas emissions to the atmosphere, but have eluded detection using traditional satellite remote sensing. We use high resolution (~3-5 m), high-frequency CubeSat sensors to measure near-daily changes in lake surface area through an object-based tracking method that incorporates machine learning to overcome notable limitations of CubeSat imagery. From ~76,000 images we obtain >2.2 million individual observations of changing surface areas for 85,358 lakes in Northern Canada and Alaska between May 1 and Oct 1, 2017. We find broad-scale lake area declines across diverse climatic, hydrologic and physiographic terrains. Localized exceptions reveal lowland flooding and aquatic vegetation phenology cycles. Cumulative small shoreline changes of abundant lakes on the Canadian Shield exceed total inundation variations of better-studied lowland environments, revealing a surprisingly dynamic landscape with respect to sub-seasonal variations in surface water extent and trace gas emissions.

1. Introduction

The Arctic-Boreal region contains the highest density of lakes on Earth (Lehner & Döll, 2004; Pekel et al., 2016; Verpoorter et al., 2014). Their areal extents fluctuate seasonally and inter-annually in response to regional water balance, fluvial inundation and surface-groundwater interactions. Variability in lake extent is thus a useful indicator of diverse climatic and physiographic processes (Tranvik et al., 2009). Furthermore, because Arctic-Boreal lakes are net sources of CO_2 and CH_4 (Hastie et al., 2018), fluctuations in lake area impact freshwater trace gas emissions to the atmosphere (Bastviken et al., 2011; Raymond et al., 2013). Lake shoreline variability is especially important because shallow water, vegetation, and CO_2 supersaturation intensify trace gas emissions along seasonally inundated lake perimeters (Bastviken et al., 2004, Tranvik et al., 2009). Quantifying the sub-seasonal variability of Arctic-Boreal lake areas is therefore critical for improving estimates of trace gas flux (Kirschke et al., 2013; Stackpoole et al., 2017) and understanding the hydrological sensitivity of lakes to geological substrate, water balance, fluvial activity, thawing permafrost, landscape disturbance and climatic change (Bring et al., 2016).

Despite the importance of sub-seasonal variations in Arctic-Boreal lakes, their temporal dynamics are poorly constrained due to a classic tradeoff between high spatial versus high temporal resolution in satellite remote sensing. Most previous studies have analyzed inter-annual changes in lake abundance and/or area using medium-to-high resolution (~30 m) imagery (e.g. Chen et al., 2014; Jepsen et al., 2013; Jones et al., 2011; Lyons et al., 2013; Olthof et al., 2015; Plug et al., 2008; Roach et al., 2013; Smith et al., 2005; Yoshikawa & Hinzman, 2003). More recently, the now-dense Landsat archive has been used to detect seasonal to interannual trends in lake area

(Nitze et al., 2017, 2018; Nitze & Grosse, 2016; Pastick et al., 2018). These studies reveal contrasting trends in lake extent variously attributed to thawing permafrost, changing water balance, hydrologic connectivity, underlying hydrogeology, shortening duration of spring snow-cover, and allometric properties such as lake area. To track sub-seasonal changes, some studies have obtained more frequent observations using very coarse resolution sensors (~25 km) (Mialon et al., 2005; Schroeder et al., 2010; Watts et al., 2014), but these analyses cannot resolve individual lakes or lake margins. Moreover, most remote sensing studies have focused on thermokarst and/or lowland wetland terrains, notably Alaska's North Slope (e.g. Frohn et al., 2005), Yukon Flats (e.g. Chen et al., 2014) and Tuktoyaktuk Peninsula (e.g. Plug et al., 2008), whereas comparatively little research has examined much larger upland, bedrock-controlled environments in Canada. Consequently, sub-seasonal variability in lake area remains one of the largest uncertainties in estimates of the freshwater carbon budget (Bastviken et al., 2011; Holgerson & Raymond, 2016; Riley et al., 2011) and its drivers are poorly understood, particularly in little-studied lake-dense upland regions (Lehner & Döll, 2004; Pekel et al., 2016).

This study quantifies sub-seasonal dynamics in lake surface water area across four study areas in Arctic-Boreal regions of Alaska and Canada using CubeSat imagery provided by Planet Labs (Planet Team, 2018). Through deployment of hundreds of satellites in a constellation, Planet CubeSats offer both high spatial (3-5m) and high temporal (near-daily) resolution. However, the imagery is acquired with inexpensive multi-spectral cameras that lack the radiometric quality, cross-sensor consistency, and geolocation accuracy of national space agency-funded missions (Cooley et al., 2017; Houborg & McCabe, 2016, 2018). To overcome these quality limitations that have, until now, prevented large-scale analyses using CubeSats, we present a novel object-based lake tracking method that incorporates machine learning. We apply this method to >75,000 CubeSat images to produce near-daily time series of surface water area for ~85,000 lakes, yielding >2.2 million individual lake observations. These observations are obtained within four strategically located study areas to capture large-scale climatic gradients, varying permafrost extent and distinctly different physiographic regions. We use this novel dataset to explore the importance of permafrost presence, topography, precipitation minus evaporation, distance from rivers, mean annual air temperature and lake allometry in controlling seasonal surface water variability. Finally, we discuss the implications of our results for freshwater inundation dynamics and carbon cycling across the Arctic-Boreal region.

2. Study Area

We track changes in lake extent across four diverse study areas spanning a range of physiographic and geological environments, namely: 1) Yukon Flats Basin (YFB), Alaska; 2) Mackenzie River Valley (MRV), Canada; 3) Canadian Shield Transect (CST) near Yellowknife, Canada; and 4) Hudson Bay Lowland (HBL), Canada. In total, these four study areas cover 226,553 km^2 of the western Arctic-Boreal region of North America (Figure 3.1 inset), and span Arctic tundra, boreal forest, peat plateau, lowland wetland and upland shield terrains. The 33,383 km^2 YFB study area is characterized by fluvially-disconnected wetlands surrounding a wide low-gradient reach of the Yukon River in north central Alaska (e.g. Anderson et al., 2013; Pitcher et al., 2018). The 82,200 km^2 MRV study area includes the Mackenzie River Delta, a vast, fluvially-connected wetland, the Tuktoyaktuk Peninsula, a polar desert with continuous permafrost and thousands of thermokarst lakes, and boreal forest and plateaus further south along the Mackenzie and Peel Rivers (Burn & Kokelj, 2009; Plug et al., 2008). The 32,107 km^2 CST is a 350 x 90 km corridor extending from

Yellowknife to the Northwest Territories-Nunavut border. It spans a lake-rich upland region consisting of exposed Precambrian bedrock surrounded by soil-filled valley bottoms (Spence & Woo, 2002, 2003, 2006). The 78,863 km^2 HBL is a 610 x 135 km transect spanning bedrock-controlled shield terrain north of Lake Winnipeg to extensive peat plateaus near the Hudson Bay coast south of Churchill, Manitoba (Wolfe et al., 2011). Taken collectively, these four study areas are broadly representative of the diverse terrains found across non-mountainous regions of Arctic-Boreal North America.

3. Methods

3.1 Data

Our primary data source is PlanetScope CubeSat satellite imagery from Planet Labs (see SI, Planet Team, 2018). PlanetScope imagery has red, blue, green and near-infrared (NIR) bands with 3.125 m spatial resolution. Given its near-daily revisit time, PlanetScope accounts for 95% of all imagery analyzed. We also use RapidEye CubeSat satellite imagery from Planet Labs, which has red, blue, green, far red and NIR bands at 5m resolution and an approximate revisit time of 5 days. No cloud mask exists for either product, but Planet Labs provides a cloud index estimating the cloud-obscured fraction of each image. We analyze all imagery with less than 20% cloud obscuration and greater than 20° solar elevation angle acquired between May 1 and October 1, 2017, a collection of ~76,000 images and ~25 TB of data across our four study areas spanning the active Arctic-Boreal hydrological season.

3.2 Water Classification and Lake Tracking Method

CubeSat imagery remains underused within academic research largely due to its lack of automated cloud mask and atmospheric correction, inconsistency in cross-sensor radiometric calibration, and geolocation error (Cooley et al., 2017). To overcome these issues, we develop a novel method that incorporates object-based lake tracking and machine learning-derived observation filtering. This method is similar to that described in Cooley et al. (2017) but adapted for automation across large spatial scales. Full details of the method are described in the supplementary information (SI), and the main steps are summarized here.

The first step entails creation of a buffered lake mask used both to seed the water classification algorithm and to track changes in lake area. This mask is built through a multi-step process involving initial water classification of early-season, cloud-free images which are summed and buffered by 60m to produce a conservative lake mask containing both the maximum seasonal extent of lakes and the surrounding land (see SI). To prevent double-counting of lake area changes, lakes whose 60m buffer zones overlap are considered to be a singular water body for lake tracking (see SI). We classify pixels as either land or water based on Normalized Difference Water Index (NDWI; McFeeters, 1996) thresholds, chosen for each image based on the shape of the buffered lake mask NDWI histogram (see SI, Cooley et al., 2017).

Next, to track seasonal changes in lake area, we calculate the total water area contained within each lake object in the 60m-buffered lake mask, recording an individual observation for each lake for every image (Cooley et al., 2017). This object-based lake tracking method is necessary because CubeSat imagery has a 10 m geolocation uncertainty (Cooley et al., 2017). By allowing lake boundaries to change over time, this tracking method minimizes the impact of geolocation inaccuracy on reported patterns in lake area and allows efficient change detection over our >2.2 million lake observations.

Finally, since the raw time series of lake areas include many erroneous data points caused by clouds, ice-cover or poor classification performance on images with a low signal to noise ratio, we use a supervised machine learning algorithm to flag poor individual lake area retrievals. For each study area, we create a manually validated training dataset and use it to seed a random forests classifier (Breiman, 2001) which categorizes all lake observations as valid/invalid based on 14 predictor variables (see SI). The best valid lake observation per day, defined as closest to the 5-day median, is then selected, and a 10-day median filter is applied to produce the final lake area time series. Through our observation filtering process, lakes only receive valid observations once they are ice-free, and therefore the start dates of the lake area time series vary between early May and late June (see SI, Fig S3.5).

To facilitate comparison between lake area time series, we produce a daily time series for all lakes > 0.01 km^2 by interpolating between near-daily satellite observations. From the lake area time series, we calculate each lake's hydrological "dynamism," defined here as its seasonal maximum area minus seasonal minimum lake area (km^2), and percent dynamism, defined as dynamism divided by seasonal maximum lake area (%, km^2/km^2). For visualization and analysis of spatial patterns, we also sum lake dynamism to a 5 x 5 km grid for each study area (see SI).

3.3 Validation and Error Analysis

We assess the accuracy of our method through both bootstrapping analyses of the manual training data and comparison with in situ pressure transducer water level measurements we collected in 15 lakes during summer 2017 (Figures S3.6 and S3.7) (see SI). The bootstrapping analysis of our observation filtering process yields RMSEs of 1,248-3,904 m^2 for mean lake area, 2,997-15,409 m^2 for maximum area, 973-22,978 m^2 for minimum area and 5,660-23,135 m^2 for seasonal dynamism (see SI, Table S3.1). As lake area is typically highly correlated with lake level, we also compare the lake area time series to our 15 in situ water level records collected in the YFB and CST. 13 of 15 CubeSat lake area time series are significantly correlated with water level at $p < 0.05$, with 12 correlated at $p < 0.01$, and all 15 lakes experience seasonal declines in both water level and lake area (see SI, Figs. S3.6 and S3.7). While a small sample size, these simultaneous in situ measurements confirm that our remotely sensed lake area changes are both real and accurate. Furthermore, this result suggests that the dominant source of area change is lake level decline rather than vegetation growth along lake margins (see SI).

3.4 Allometric and Environmental Controls on Lake Area Changes

A key challenge of interpreting temporal and spatial patterns in lake extent is the strong relationship between lake size, seasonal dynamism and percent dynamism. Dynamism is positively correlated to lake size whereas percent change is negatively correlated to lake size (see SI). To control for this effect, we develop a new lake metric, termed R_Δ, which represents the mean lateral distance (in meters) between each lake's maximum and minimum observed shoreline boundaries (see SI, Fig. S3.11). Because R_Δ is independent of lake area, this metric facilitates comparison of spatial patterns in surface water seasonality across different lake sizes.

Finally, we use generalized multivariable regression to analyze drivers of seasonal dynamism. We calculate gridded lake allometric variables, namely water fraction (Fig. S3.8), perimeter (Fig. S3.9), number of lakes and mean lake area from our lake area time series. We also test distance from river network, permafrost state (Brown et al., 2002), mean annual air temperature (GISTEMP Team, 2018) and precipitation minus evaporation (P – E) (Fig. S3.10; Vimal et al., 2018) and mean elevation and topographic roughness (Yamazaki et al., 2017). All variables are summed or averaged to a 5 x 5 km grid and regressions are performed using each grid cell as an individual data point (see SI).

4. Results

We identify 85,358 lakes (> 0.01 km^2) across our four study areas, with 8,854 in the YFB, 37,957 in the MRV, 21,560 in the CST and 16,987 in the HBL. Lake size approximately follows a Pareto distribution, similar to previous lake mapping estimates (Downing et al., 2006; Lehner & Döll, 2004; Verpoorter et al., 2014). The mean lake size within each of the four study areas ranges from 0.11 ($\pm$0.25) km^2 (YFB) to 0.31 ($\pm$1.82) km^2 (CST) with an average value of 0.26 ($\pm$1.45) km^2 across all four. Over the course of the study period, the mean total lake areas are 802 (YFB), 9,336 (MRV), 6,479 (CST) and 5,082 (HBL) km^2. Converted to units of water fraction (lake surface area divided by total study area), the highest water fraction is found on the CST (20.2%), followed by the MRV (11.4%), HBL (6.4%) and YFB (2.4%).

On average, Arctic-Boreal lakes receive a valid, cloud-free observation once every 5.2 ($\pm$1.9) days, varying from 4.1 ($\pm$1.0) for the YFB to 6.2 ($\pm$1.8) for the MRV. We find a near-universal decline in lake extent during the study period, which is widespread across all four study areas, including lowland wetland and upland bedrock terrains (Figure 3.1). These declines are consistent with in situ observations of water level (Figures S3.6 and S3.7) and reflect broadly negative summer P – E over Northern North America in 2017 (Fig. S3.10). The YFB, MRV and CST show remarkable similarity in their sub-seasonal progression, decreasing steeply from the start of the open water season until the end of July, and then remaining mostly stable or increasing slightly through the end of September (Figure 3.2). In contrast, the HBL declines gradually and is more stable overall, perhaps due to its lack of well-developed river networks, low water fraction and high water storage in its peatland terrain (Smith et al., 2012) (Fig. 3.2).

Gridded maps of lake dynamism reveal loci of spring flooding in the YFB and MRD as well as substantial, dispersed dynamism throughout the CST (Fig. 3.1). The percent dynamism is 29% (dynamism = 279 km^2) for YFB, 9% (907 km^2) for MRV, 7% (439 km^2) for CST and 5% (247 km^2) for HBL (Figure 3.2b). The mean individual lake percent change is comparable for the MRV, CST and HBL (17%, 18% and 15%), but higher in the YFB where, on average, lakes change by 39%. However, when lake dynamism is considered at the landscape scale, the change in surface water extent per unit land area is 0.8%, 1.1%, 1.4% and 0.3%, for the four study areas, respectively. In other words, the greatest change in lake water fraction is found in the CST, where 1.4% of the total landscape is seasonally inundated, nearly double that of the YFB.

The high spatial resolution and dense temporal sampling afforded by CubeSats also reveals distinct localized exceptions to the broader seasonal decline, as exemplified by local concentrations of lake dynamism within the MRV (Fig. 3.2c). The Mackenzie River Delta undergoes a steep decline (~8%) in lake area until mid-July, after which lake areas stabilize, a progression likely associated with floodplain inundation following ice breakup and peak river discharge. In contrast, the thermokarst-dominated Tuktoyaktuk Peninsula experiences a small, gradual seasonal decline (~3%) in total lake area, and the Lower Mackenzie Plain declines sharply through July (~12%) before rebounding in August and September (Fig. 3.2c). Visual inspection reveals that this distinct signal in the Lower Mackenzie Plain is primarily driven by a high incidence of lakes that experience a large change in area due to rapid emergence and then decline of aquatic vegetation and/or algae at their surface. When mapped across the four study areas, we find these 'vegetation-impacted' lakes account for 1-2% of all lakes studied and 7-13% of the observed dynamism across the YFB, MRV and CST, with particular concentration in the Lower Mackenzie Plain and the southern tip of the CST (see SI, Fig. S3.12).

CubeSat observations of R_Δ (i.e. mean lateral distance between maximum and minimum lake boundaries) reveal that most Arctic-Boreal lake dynamism is driven by small shoreline fluctuations of $\leq$ 10 m (Figure 3.3). Across all study areas, the mean R_Δ is 6.6 ($\pm$8.6) m, varying from 5.0 ($\pm$5.0) m in the HBL to 13.0 ($\pm$13.0) m in the YFB. Large R_Δ values are primarily associated with floodplains and vegetation-impacted lakes, whereas low R_Δ values predominate in upland regions (Fig. 3). For the YFB, lakes with a $R_\Delta \leq 10$ m account for just 28% of the observed dynamism, whereas they account for 54% in the MRV and 76% in both the CST and HBL. This suggests that landscape-scale lake dynamism is dominated by fewer highly dynamic lakes in the YFB versus many comparatively stable lakes in the CST and HBL, with the CST displaying the greatest overall dynamism due to the cumulative small shoreline fluctuations of many more lakes (Fig. 3.2a, white asterisk in Fig. 3.3).

Multivariable regression of gridded lake dynamism with allometric (water fraction, lake perimeter, number of lakes, mean lake size) and environmental (elevation, topographic roughness, permafrost presence, MAAT, distance to river, and P – E) variables indicates that total seasonal dynamism strongly depends on lake allometry. The regression models built using these 10 variables explain 74%, 65%, 58% and 55% of the total variance in seasonal dynamism for the four study areas, respectively (Fig S3.13, Table S3.2). Between 87% (CST) and 99% (YFB and MRV) of the explanatory power is associated with perimeter and water fraction alone. In contrast, environmental variables explain only 2-16% of the observed dynamism, with permafrost and MAAT the strongest predictors, suggesting little detectable environmental control on lake dynamism over the study period (see SI).

5. Discussion

Our object-based CubeSat lake tracking method allows us to monitor fine-scale changes in surface water with high temporal frequency across large spatial scales. The combination of 3-5 m spatial resolution and ~5-day average cloud-free revisit time yielded >2.2 million observations of lakes as small as 0.01 km^2 in just five months. By using machine learning to filter out low quality observations, some critical limitations of CubeSat imagery are overcome, enabling scientific analysis of thousands of images and millions of individual lake observations. Consequently, our analysis of ~85,000 lakes reveals both broad-scale similarities and novel fine-scale anomalies in sub-seasonal inundation dynamics of Arctic-Boreal lakes.

Broadly, we observe a universal, synchronous seasonal draw-down in surface water extent across our four study areas throughout the 2017 open-water season. This finding differs from most studies of surface water dynamics in Arctic-Boreal regions, which tend to focus on dynamic, flood-prone lowlands such as the Yukon Flats (Anderson et al., 2013; Chen et al., 2014; Jepsen et al., 2016), Mackenzie River Delta (Goulding et al., 2009; Lesack et al., 2013; Marsh & Lesack, 1996), and Peace-Athabasca Delta (Pavelsky & Smith, 2008). While our study confirms that lakes in such environments are hydrologically dynamic, it also shows that their relatively small areas and comparatively low water fractions may make them less important to continental-scale surface water variability than the outsized attention they receive might suggest. Indeed, in absolute terms we identify more *total* lake dynamism elsewhere. Lake percent area changes and R_Δ values are lower in upland regions like the CST and southeastern HBL, likely due to higher topographic variability and poorly developed fluvial drainage. However, when multiplied across large, lake-rich areas, these small shoreline changes cumulatively produce large absolute changes in lake surface area across the landscape.

This effect is exemplified by the contrast between the Canadian Shield Transect and the heavily studied Yukon Flats Basin, which are similar in size (32,107 km^2 and 33,383 km^2) yet display vastly different sub-seasonal dynamics in lake area. Despite containing few highly dynamic lakes and a smaller percent dynamism (7% vs. 29%), the CST experiences significantly more *absolute* lake dynamism than the YFB (439 km^2 vs. 279 km^2) due to its much larger water fraction (20% vs. 2%). Previous surface water studies have largely ignored this landscape-scale effect. Coarse-resolution global/pan-Arctic analyses do include the Canadian Shield but have difficulty resolving the fine-scale changes that dominate sub-seasonal lake dynamics in this area. For example, a comparison of our CubeSat results with a recent global Landsat-based seasonality product (GWSO; Pekel et al., 2016) finds that even the 30m, ~16-day revisit time of this high-quality product likely underestimates total seasonal dynamism by up to 50% (Fig. S3.14), especially in the CST, where small shoreline fluctuations (low R_{Δ}s) dominate. While some of this difference may be due to inter-annual variability (see SI), this improved quantification of lake dynamism in the CST is likely an outcome of the high spatial resolution of CubeSat imagery, which enables mapping of numerous small, previously undetectable lake shoreline changes that sum to large areas of intermittently inundated land.

Our quantification of substantial, widespread dynamism accrued from small shoreline fluctuations of many lakes is consequential for estimates of trace gas emissions from freshwater bodies. In contrast to the relatively 'static' view of upland lakes commonly assumed by CH_4 and CO_2 emission models (Bastviken et al., 2011; Matthews & Fung, 1987; Raymond et al., 2013; Ringeval et al., 2010; Watts et al., 2014) our results suggest that all Arctic-Boreal landscapes are dynamic, and often at fine spatial scales missed by coarse-resolution products. This finding is inherently conservative as we consider only open-water lake shorelines in this study, whereas Arctic-Boreal lake fluctuations commonly recharge surrounding wetlands as well. Furthermore, littoral, seasonally inundated shorelines and wetlands are known "hotspots" of freshwater CO_2 and CH_4 production and emission (Bastviken et al., 2004; Tranvik et al., 2009), suggesting that 1 km^2 of intermittently inundated land comprised of numerous small shoreline fluctuations likely emits more trace gas than 1 km^2 of permanently inundated land owing to shallow water, vegetation, and CO_2 supersaturation. Lastly, because Shield landscapes have both high water fractions and high lake densities, they typically have a very high lake perimeter to land surface area ratio (2.3 km/km^2 for CST versus 0.6 km/km^2 for YFB) and thus the total area of intermittently inundated lake shorelines potentially contributing to CO_2 emission in upland regions is large.

Finally, our analysis of potential drivers of sub-seasonal surface water dynamism identifies an outsized importance of lake allometry (Lyons et al., 2013; Smith & Pavelsky, 2009), and particularly lake perimeter, on spatiotemporal patterns in lake area change. Other variables commonly cited as drivers of inter-annual lake surface area change, such as water balance (Anderson et al., 2013; Chen et al., 2014; Plug et al., 2008; Riordan et al., 2006), permafrost presence (Jepsen et al., 2013; Smith et al., 2005; Walvoord et al., 2012) and distance from river networks (Roach et al., 2013) appear to have a negligible effect on intra-annual lake dynamism compared to lake allometry. Better ancillary datasets could produce different results, and we suggest future work to confirm or refute this finding, but a clear conclusion of our study is that any broad-scale study seeking to attribute lake area changes to permafrost, climate, or other external factors must first control for lake allometry. Given that these factors influence lake allometry themselves (Smith et al., 2007), future work should also consider the interactions between lake allometry and environmental variables.

6. Conclusion

Our Arctic-Boreal lake tracking analysis advances the utility of CubeSat imagery for hydrologic research. At the local scale, the high temporal and spatial resolutions of CubeSat imagery reveal short-lived phenomena such as floodplain inundation and aquatic vegetation phenology, observations that can inform a wide range of applications including carbon cycling (Bastviken et al., 2004; Tranvik et al., 2009), water quality (Palmer et al., 2015) and hydrologic connectivity (Pavelsky & Smith, 2008). At the broad scale, we identify a ubiquitous drawdown of surface water across northern North America during summer 2017, including substantial water loss caused by fine-scale lake shoreline contractions on the lake-dense Canadian Shield, which coarser-resolution sensors miss. This finding suggests that current models of CO_2 and CH_4 trace gas emission from inland waters underestimate the importance of sub-seasonal lake area dynamics.

Acknowledgements

This research was funded by the NASA Terrestrial Ecology Program Arctic-Boreal Vulnerability Experiment (ABoVE) grant #NNX17AC60A. S. Cooley is also funded by a National Science Foundation Graduate Research Fellowship. We thank Planet Labs Education and Research Program Director Joseph Mascaro and the Planet Labs Ambassador Program for providing access to all PlanetScope and RapidEye imagery. We thank David Butman (University of Washington), Simon Topp (University of North Carolina at Chapel Hill), Mark Bertram and Heather Bartlett (Yukon Flats National Wildlife Refuge) for their assistance in collecting in situ lake level records in the Yukon Flats Basin. We thank the Gwichyaa Zhee Gwich'in Tribal Government and Doyon Limited along with the Yukon Flats National Wildlife Refuge and the US Fish and Wildlife Service for access to the lands and waterways of the Yukon Flats. We thank Bruce Hanna (Government of the Northwest Territories Environment and Natural Resource Division), and Dave Olesen for their assistance in collecting lake level records in the Canadian Shield Transect. Finally, we thank Henry Johnson (Brown University) for support with computing and data storage. The CubeSat-derived lake area time series and associated metadata are archived at the Oak Ridge National Laboratory Distributed Active Archive Center (ORNL DAAC) and are can be accessed here: https://doi.org/10.3334/ORNLDAAC/1667. We thank Ben Jones and an anonymous reviewer for their insightful feedback on an earlier version of this manuscript.

References

Anderson, L., Birks, J., Rover, J., & Guldager, N. (2013). Controls on recent Alaskan lake changes identified from water isotopes and remote sensing. *Geophysical Research Letters*, *40*(May 2013), 3413–3418. https://doi.org/10.1002/grl.50672

Bastviken, D., Cole, J., Pace, M., & Tranvik, L. (2004). Methane emissions from lakes: Dependence of lake characteristics, two regional assessments, and a global estimate. *Global Biogeochemical Cycles*, *18*(4), 1–12. https://doi.org/10.1029/2004GB002238

Bastviken, D., Tranvik, L. J., Downing, J. A., Crill, P. M., & Enrich-Prast, A. (2011). Freshwater methane emissions offset the continental carbon sink. *Science*, *331*(6013), 50. https://doi.org/10.1126/science.1196808

Breiman, L. (2001). Random Forests. *Machine Learning*, *45*, 5–32. https://doi.org/10.1023/A:1010933404324

Bring, A., Fedorova, I., Dibike, Y., Hinzman, L., Mård, J., Mernild, S. H., et al. (2016). Arctic terrestrial hydrology: A synthesis of processes, regional effects, and research challenges. *Journal of Geophysical Research G: Biogeosciences*, *121*(3), 621–649. https://doi.org/10.1002/2015JG003131

Brown, J., Ferrians, J., Heginbottom, A., & Melnikov, E. (2002). Circum-Arctic Map of Permafrost and Ground-Ice Conditions, Version 2. Boulder, Colorado, USA: NSIDC: National Snow and Ice Data Center.

Burn, C. R., & Kokelj, S. V. (2009). The Environment and Permafrost the Mackenzie Delta Area. *Permafrost and Periglacial Processes*, *20*(April), 83–105. https://doi.org/10.1002/ppp

Chen, M., Rowland, J. C., Wilson, C. J., Altmann, G. L., & Brumby, S. P. (2014). Temporal and spatial pattern of thermokarst lake area changes at Yukon Flats, Alaska. *Hydrological Processes*, *28*(November 2012), 837–852. https://doi.org/10.1002/hyp.9642

Cooley, S. W., Smith, L. C., Stepan, L., & Mascaro, J. (2017). Tracking dynamic northern surface water changes with high-frequency planet CubeSat imagery. *Remote Sensing*, *9*(12), 1–21. https://doi.org/10.3390/rs9121306

Downing, J. A., Prairie, Y. T., Cole, J. J., Duarte, C. M., Tranvik, L. J., Striegl, R. G., et al. (2006). The global abundance and Size Distribution of Lakes, Ponds and Impoundments. *Limnol. Oceanogr*, *51*(5), 469–478. https://doi.org/http://dx.doi.org/10.1016/B978-012370626-3.00025-9

Frohn, R. C., Hinkel, K. M., & Eisner, W. R. (2005). Satellite remote sensing classification of thaw lakes and drained thaw lake basins on the North Slope of Alaska, *97*, 116–126. https://doi.org/10.1016/j.rse.2005.04.022

GISTEMP Team. (2018). GISS Surface Temperature Analysis (GISTEMP). *NASA Goddard Institute for Space Studies*.

Goulding, H. L., Prowse, T. D., & Beltaos, S. (2009). Spatial and temporal patterns of break-up and ice-jam flooding in the Mackenzie Delta, NWT Holly. *Hydrological Processes*, *23*, 2654–2670. https://doi.org/10.1002/hyp

Holgerson, M. A., & Raymond, P. A. (2016). Large contribution to inland water CO2and CH4emissions from very small ponds. *Nature Geoscience*, *9*(3), 222–226. https://doi.org/10.1038/ngeo2654

Houborg, R., & McCabe, M. F. (2016). High-Resolution NDVI from planet's constellation of earth observing nano-satellites: A new data source for precision agriculture. *Remote Sensing*, *8*(9). https://doi.org/10.3390/rs8090768

Houborg, R., & McCabe, M. F. (2018). A Cubesat enabled Spatio-Temporal Enhancement Method (CESTEM) utilizing Planet, Landsat and MODIS data. *Remote Sensing of Environment*, *209*(July 2017), 211–226. https://doi.org/10.1016/j.rse.2018.02.067

Jepsen, S. M., Voss, C. I., Walvoord, M. A., Rose, J. R., Minsley, B. J., & Smith, B. D. (2013). Sensitivity analysis of lake mass balance in discontinuous permafrost: the example of disappearing Twelvemile Lake, Yukon Flats, Alaska (USA). *Hydrogeology Journal*, *21*(1), 185–200. https://doi.org/10.1007/s10040-012-0896-5

Jepsen, S. M., Walvoord, M. A., Voss, C. I., & Rover, J. (2016). Effect of permafrost thaw on the dynamics of lakes recharged by ice-jam floods: Case study of Yukon Flats, Alaska. *Hydrological Processes*, *30*(11), 1782–1795. https://doi.org/10.1002/hyp.10756

Jones, B. M., Grosse, G., Arp, C. D., Jones, M. C., Walter Anthony, K. M., & Romanovsky, V. E. (2011). Modern thermokarst lake dynamics in the continuous permafrost zone, northern Seward Peninsula, Alaska. *Journal of Geophysical Research: Biogeosciences*, *116*, 1–13. https://doi.org/10.1029/2011JG001666

Kirschke, S., Bousquet, P., Ciais, P., Saunois, M., Canadell, J. G., Dlugokencky, E. J., et al. (2013). Three decades of global methane sources and sinks. *Nature Geoscience*, *6*(10), 813–823. https://doi.org/10.1038/ngeo1955

Lehner, B., & Döll, P. (2004). Development and validation of a global database of lakes, reservoirs and wetlands. *Journal of Hydrology*, *296*(1–4), 1–22. https://doi.org/10.1016/j.jhydrol.2004.03.028

Lesack, L. F. W., Marsh, P., Hicks, F. E., & Forbes, D. L. (2013). Timing, duration, and magnitude of peak annual water-levels during ice breakup in the Mackenzie Delta and the role of river discharge. *Water Resources Research*, *49*, 8234–8249. https://doi.org/10.1002/2012WR013198

Lyons, S. R., Sheng, Y., Smith, L. C., Li, J., Hinkel, K. M., Lenters, J. D., & Wang, J. (2013). Quantifying sources of error in multitemporal multisensor lake mapping. *International Journal of Remote Sensing*, *23*(22), 7887–7905. https://doi.org/10.1080/01431161.2013.8273432013

Marsh, P., & Lesack, L. F. W. (1996). The hydrologic regime of perched lakes in the Mackenzie Delta: Potential responses to climate change. *Limnology and Oceanography*, *41*(5), 849–856. https://doi.org/10.4319/lo.1996.41.5.0849

Matthews, E., & Fung, I. (1987). Methane emission from natural wetlands: Global distribution, area, and environmental characteristics of sources. *Global Biogeochemical Cycles*, *1*(1), 61–86. https://doi.org/10.1029/GB001i001p00061

McFeeters, S. K. (1996). The use of the Normalized Difference Water Index (NDWI) in the delineation of open water features. *International Journal of Remote Sensing*, *17*(7), 1425–1432. https://doi.org/10.1080/01431169608948714

Mialon, A., Royer, A., & Fily, M. (2005). Wetland seasonal dynamics and interannual variability over northern high latitudes, derived from microwave satellite data. *Journal of Geophysical Research D: Atmospheres*, *110*(17), 11–19. https://doi.org/10.1029/2004JD005697

Nitze, I., & Grosse, G. (2016). Detection of landscape dynamics in the Arctic Lena Delta with temporally dense Landsat time-series stacks. *Remote Sensing of Environment*, *181*, 27–41. https://doi.org/10.1016/j.rse.2016.03.038

Nitze, I., Grosse, G., Jones, B. M., Arp, C. D., Ulrich, M., Fedorov, A., & Veremeeva, A. (2017). Landsat-based trend analysis of lake dynamics across Northern Permafrost Regions. *Remote Sensing*, *9*(7), 1–28. https://doi.org/10.3390/rs9070640

Nitze, I., Grosse, G., Jones, B. M., Romanovsky, V. E., & Boike, J. (2018). Remote sensing quantifies widespread abundance of permafrost region disturbances across the Arctic and Subarctic. *Nature Communications*, *9*(1), 5423. https://doi.org/10.1038/s41467-018-07663-3

Olthof, I., Fraser, R. H., & Schmitt, C. (2015). Landsat-based mapping of thermokarst lake dynamics on the Tuktoyaktuk Coastal Plain, Northwest Territories, Canada since 1985. *Remote Sensing of Environment*, *168*, 194–204. https://doi.org/http://dx.doi.org/10.1016/j.rse.2015.07.001

Palmer, S. C. J., Kutser, T., & Hunter, P. D. (2015). Remote sensing of inland waters: Challenges, progress and future directions. *Remote Sensing of Environment*, *157*, 1–8. https://doi.org/10.1016/j.rse.2014.09.021

Pastick, N. J., Jorgenson, M. T., Goetz, S. J., Jones, B. M., Wylie, B. K., Minsley, B. J., et al. (2018). Spatiotemporal remote sensing of ecosystem change and causation across Alaska. *Global Change Biology*, (January). https://doi.org/10.1111/gcb.14279

Pavelsky, T. M., & Smith, L. C. (2008). Remote sensing of hydrologic recharge in the Peace-Athabasca Delta, Canada. *Geophysical Research Letters*, *35*(8), 1–5. https://doi.org/10.1029/2008GL033268

Pekel, J.-F., Cottam, A., Gorelick, N., & Belward, A. S. (2016). High-resolution mapping of global surface water and its long-term changes. *Nature*, *540*(7633), 418–422.

https://doi.org/10.1038/nature20584

Pitcher, L. H., Pavelsky, T. M., Smith, L. C., Moller, D. K., Altenau, E. H., Allen, G. H., et al. (2018). AirSWOT InSAR mapping of surface water elevations and hydraulic gradients across the Yukon Flats Basin, Alaska. *Water Resources Research*. https://doi.org/10.1029/2018WR023274

Planet Team. (2018). Planet Application Program Interface: In Space for Life on Earth. San Francisco, CA. Retrieved from https://api.planet.com

Plug, L. J., Walls, C., & Scott, B. M. (2008). Tundra lake changes from 1978 to 2001 on the Tuktoyaktuk Peninsula, western Canadian Arctic. *Geophysical Research Letters*, *35*(December 2007), L03502. https://doi.org/10.1029/2007GL032303

Raymond, P. A., Hartmann, J., Lauerwald, R., Sobek, S., McDonald, C., Hoover, M., et al. (2013). Global carbon dioxide emissions from inland waters. *Nature*, *503*(7476), 355–359. https://doi.org/10.1038/nature12760

Riley, W. J., Subin, Z. M., Lawrence, D. M., Swenson, S. C., Torn, M. S., Meng, L., et al. (2011). Barriers to predicting changes in global terrestrial methane fluxes: Analyses using CLM4Me, a methane biogeochemistry model integrated in CESM. *Biogeosciences*, *8*(7), 1925–1953. https://doi.org/10.5194/bg-8-1925-2011

Ringeval, B., De Noblet-Ducoudré, N., Ciais, P., Bousquet, P., Prigent, C., Papa, F., & Rossow, W. B. (2010). An attempt to quantify the impact of changes in wetland extent on methane emissions on the seasonal and interannual time scales. *Global Biogeochemical Cycles*, *24*(2), 1–12. https://doi.org/10.1029/2008GB003354

Riordan, B., Verbyla, D., & McGuire, a. D. (2006). Shrinking ponds in subarctic Alaska based on 1950-2002 remotely sensed images. *Journal of Geophysical Research: Biogeosciences*, *111*(December 2005), G04002. https://doi.org/10.1029/2005JG000150

Roach, J. K., Griffith, B., & Verbyla, D. (2013). Landscape influences on climate-related lake shrinkage at high latitudes. *Global Change Biology*, *19*, 2276–2284. https://doi.org/10.1111/gcb.12196

Schroeder, R., Rawlins, M. A., McDonald, K. C., Podest, E., Zimmermann, R., & Kueppers, M. (2010). Satellite microwave remote sensing of North Eurasian inundation dynamics: Development of coarse-resolution products and comparison with high-resolution synthetic aperture radar data. *Environmental Research Letters*, *5*(1). https://doi.org/10.1088/1748-9326/5/1/015003

Smith, L. C., & Pavelsky, T. M. (2009). Remote sensing of volumetric storage changes in lakes. *Earth Surface Processes and Landforms*, *34*, 1343–1358. https://doi.org/10.1002/esp

Smith, L. C., Sheng, Y., MacDonald, G. M., & Hinzman, L. D. (2005). Disappearing Arctic lakes. *Science (New York, N.Y.)*, *308*, 1429. https://doi.org/10.1126/science.1108142

Smith, L. C., Sheng, Y., MacDonald, G. M., & Hinzman, L. D. (2005). Disappearing Arctic lakes. *Science*, *308*(5727), 1429. https://doi.org/10.1126/science.1108142

Smith, L. C., Sheng, Y., & MacDonald, G. M. (2007). A First Pan-Arctic Assessment of the Influence of Glaciation, Permafrost, Topography and Peatlands on Northern Hemisphere Lake Distribution. *Permafrost and Periglacial Processes*, *20*, 173–184. https://doi.org/10.1002/ppp

Smith, L. C., Beilman, D. W., Kremenetski, K. V., Sheng, Y., MacDonald, G. M., Lammers, R. B., et al. (2012). Influence of permafrost on water storage in West Siberian peatlands revealed from a new database of soil properties. *Permafrost and Periglacial Processes*, *23*(1), 69–79. https://doi.org/10.1002/ppp.735

Spence, C., & Woo, M. K. (2002). Hydrology of subarctic Canadian shield: Bedrock upland. *Journal of Hydrology*, *262*(1–4), 111–127. https://doi.org/10.1016/S0022-1694(02)00010-0

Spence, C., & Woo, M. K. (2003). Hydrology of subarctic Canadian shield: Soil-filled valleys. *Journal of Hydrology*, *279*(1–4), 151–166. https://doi.org/10.1016/S0022-1694(03)00175-6

Spence, C., & Woo, M. K. (2006). Hydrology of subarctic Canadian Shield: Heterogeneous headwater basins. *Journal of Hydrology*, *317*(1–2), 138–154. https://doi.org/10.1016/j.jhydrol.2005.05.014

Stackpoole, S. M., Butman, D. E., Clow, D. W., Verdin, K. L., Gaglioti, B. V., Genet, H., & Striegl, R. G. (2017). Inland waters and their role in the carbon cycle of Alaska: *Ecological Applications*, *27*(5), 1403–1420. https://doi.org/10.1002/eap.1552

Tranvik, L. J., Downing, J. A., Cotner, J. B., Loiselle, S. A., Striegl, R. G., Ballatore, T. J., et al. (2009). Lakes and reservoirs as regulators of carbon cycling and climate. *Limnology and Oceanography*, *54*(6part2), 2298–2314. https://doi.org/10.4319/lo.2009.54.6_part_2.2298

Verpoorter, C., Kutser, T., Seekell, D. A., & Tranvik, L. J. (2014). A global inventory of lakes based on high-resolution satellite imagery. *Geophysical Research Letters*, *41*(18), 6396–6402. https://doi.org/10.1002/2014GL060641

Vimal, S., Lettenmaier, D. P., & Smith, L. C. (2018). Hydrological Fluxes from 1979-2018 for Canada and Alaska. Oak Ridge National Laboratory (ORNL) Distributed Active Archive Center (DAAC) for Biogeochemical Dynamics.

Walvoord, M. A., Voss, C. I., & Wellman, T. P. (2012). Influence of permafrost distribution on groundwater flow in the context of climate-driven permafrost thaw: Example from Yukon Flats Basin, Alaska, United States. *Water Resources Research*, *48*(7), 1–17. https://doi.org/10.1029/2011WR011595

Watts, J. D., Kimball, J. S., Bartsch, A., & McDonald, K. C. (2014). Surface water inundation in the boreal-Arctic: Potential impacts on regional methane emissions. *Environmental Research Letters*, *9*(7). https://doi.org/10.1088/1748-9326/9/7/075001

Wolfe, B. B., Light, E. M., MacRae, M. L., Hall, R. I., Eichel, K., Jasechko, S., et al. (2011). Divergent hydrological responses to 20th century climate change in shallow tundra ponds, western Hudson Bay Lowlands. *Geophysical Research Letters*, *38*(23), 1–6. https://doi.org/10.1029/2011GL049766

Yamazaki, D., Ikeshima, D., Tawatari, R., Yamaguchi, T., O'Loughlin, F., Neal, J. C., et al. (2017). A high-accuracy map of global terrain elevations. *Geophysical Research Letters*, *44*(11), 5844–5853. https://doi.org/10.1002/2017GL072874

Yoshikawa, K., & Hinzman, L. D. (2003). Shrinking thermokarst ponds and groundwater dynamics in discontinuous permafrost near Council, Alaska. *Permafrost and Periglacial Processes*, *14*(January 2016), 151–160. https://doi.org/10.1002/ppp.451

Figures

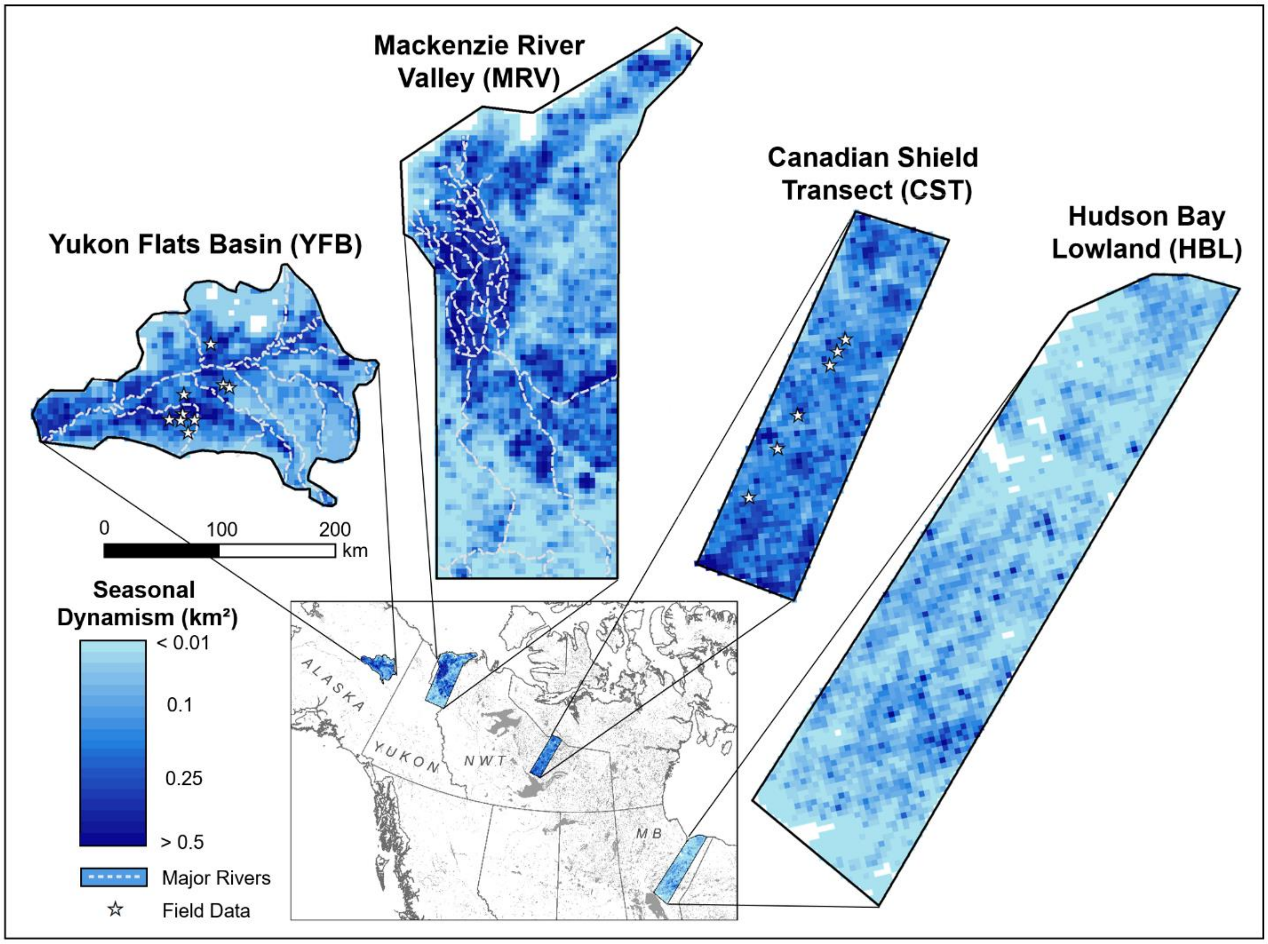

Figure 3.1. Gridded maps of lake dynamism (seasonal maximum minus seasonal minimum lake area, km^2) for our YFB, MRV, CST and HBL study areas derived from CubeSat satellite imagery and machine learning. White dashed lines show major river systems (Yukon and Mackenzie Rivers and their tributaries). High dynamism is dispersed across the CST, as well as concentrated in the central YFB along the Yukon River and Mackenzie River Delta (northwest MRV). Stars indicate locations of in-situ lake level measurements.

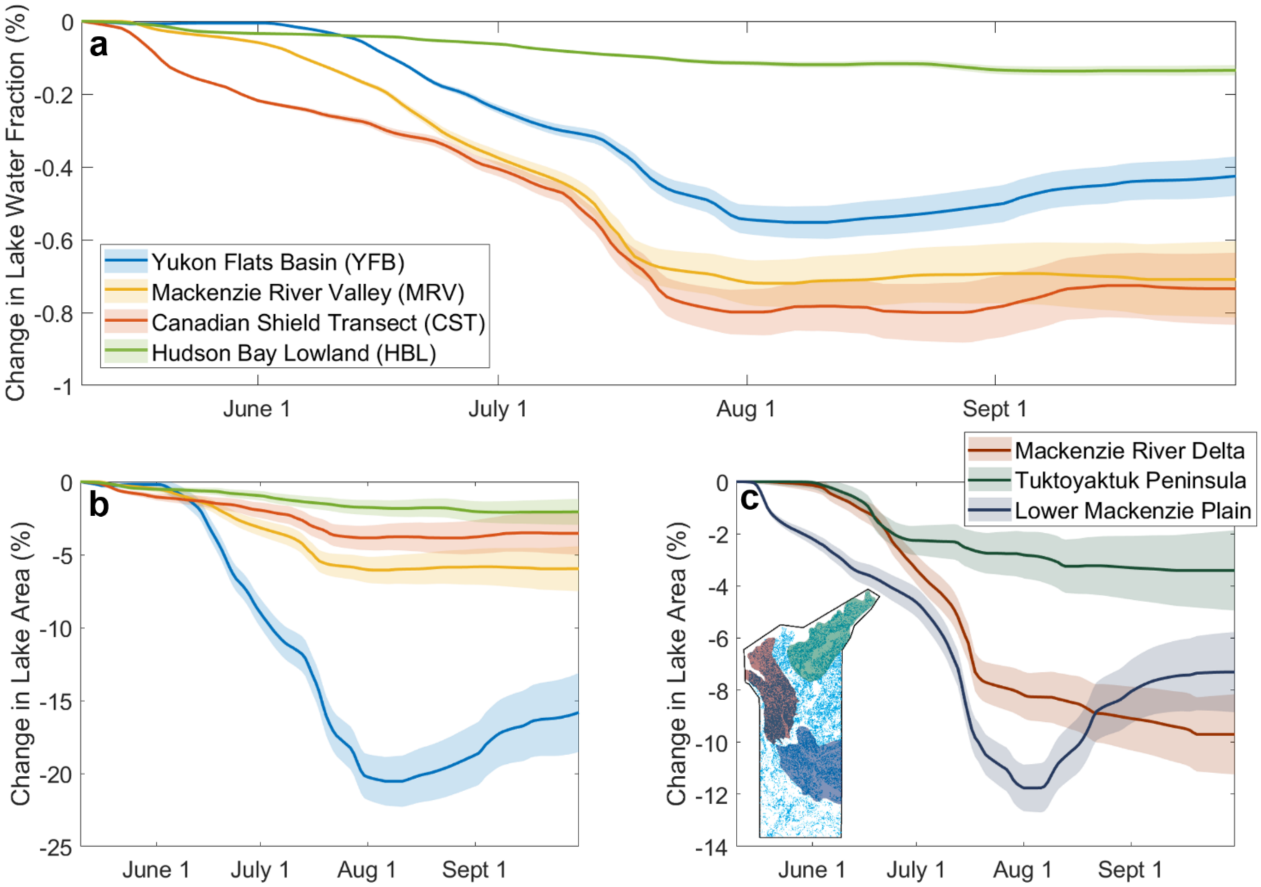

Figure 3.2. Temporal progression of area changes in 85,358 lakes summed across the YFB, MRV, CST and HBL study areas calculated from >2.2 million CubeSat observations of lake area. Shaded areas are uncertainty bounds determined from RMSE values. Summed lake area changes are shown as both (a) percent of total study area (33,383, 82,200, 32,107 and 78,863 km^2, respectively), and (b) percent of maximum observed lake area (952, 9,845, 6,723 and 5,217 km^2, respectively). While YFB lakes are highly variable (blue line in 2b), the CST is most dynamic at the landscape scale (red line in 2a). Panel (c) splits the MRV (yellow line in 2b) into three sub-regions, revealing contrasting sub-seasonal progressions between relatively stable lakes of Tuktoyaktuk Peninsula (dark green), dynamic lakes of the fluvial-deltaic Mackenzie River Delta (maroon), and sub-seasonal phenological cycles in aquatic vegetation in lakes of the Lower Mackenzie Plain (navy blue).

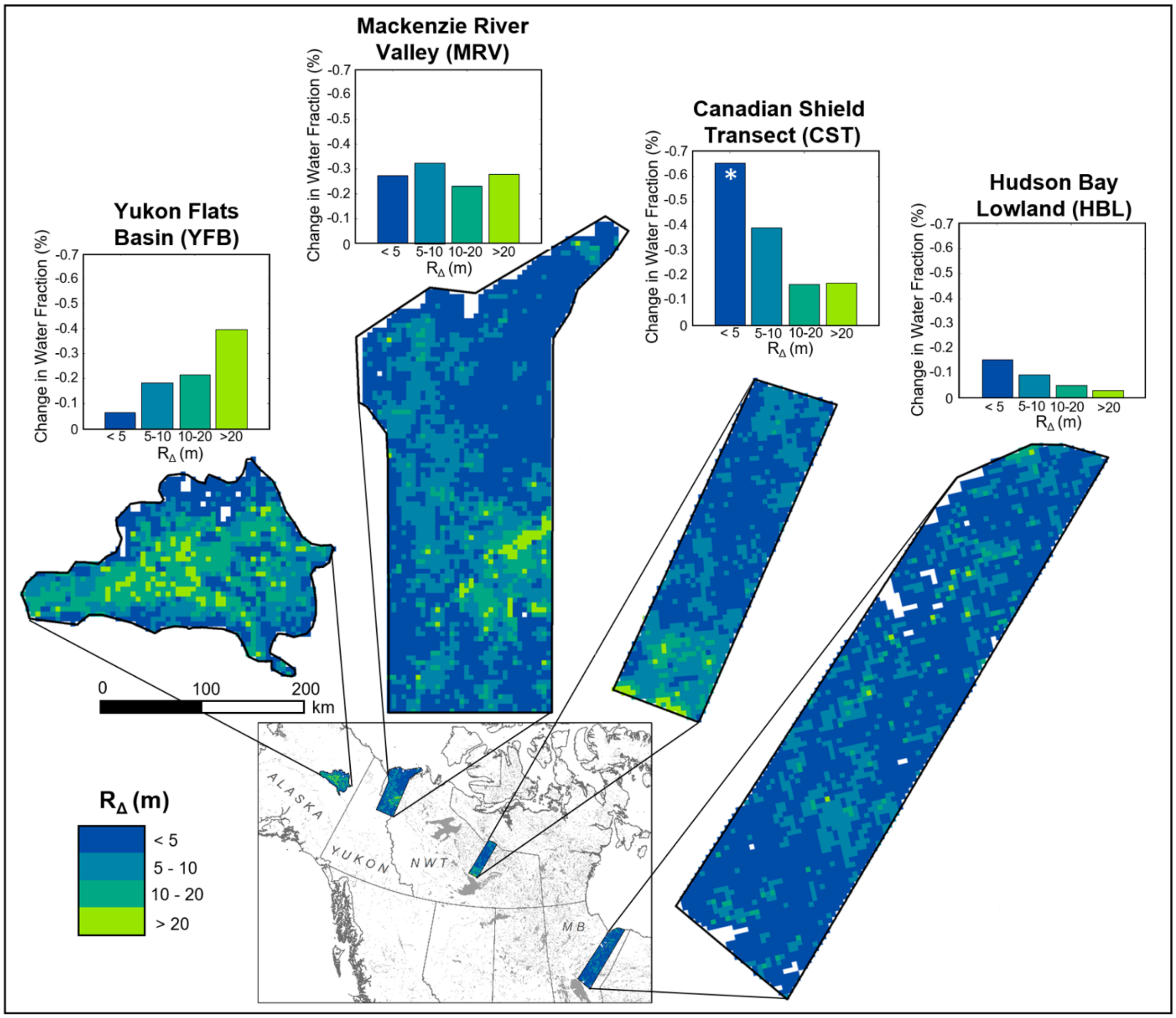

Figure 3.3. Gridded maps of mean lateral distance between maximum and minimum observed lake boundaries (R_Δ, m) for YFB, MRV, CST, and HBL. Bar graphs quantify the change in lake water fraction (%) associated with lakes within specified R_Δ ranges. The CST displays the highest overall change in lake water fraction, dominated especially by small shoreline fluctuations ($R_\Delta \leq 5$, white asterisk).

Supplementary Information

Text S1. Data Selection and Preprocessing

Two sources of Planet Labs CubeSat imagery were used to track changes in lake extent across the Arctic-Boreal region between May 1 and October 1, 2017. The first source, PlanetScope, is collected by a constellation of 120 CubeSats known as ‘Doves’, which are 10 cm x 10 cm x 30 cm in size. PlanetScope Doves contain a split-frame imager which captures four bands, blue (Band 1, 455-515 nm), green (Band 2, 500-590 nm), red (Band 3, 590-670 nm) and near infrared (Band 4, 780-860 nm), at 3.7 m pixel resolution. Due its near-daily availability, PlanetScope accounts for 95% of all imagery analyzed in this study. Where available, we also use RapidEye imagery, which is a constellation of 5 satellites with a ground resolution of 6.5m and a revisit time of ~5 days. RapidEye imagery has five bands: blue (Band 1, 440-510 nm), green (Band 2, 520-590 nm), red (Band 3, 630-685 nm), red edge (Band 4, 690-730 nm) and near infrared (Band 5, 760-850 nm). For both PlanetScope and RapidEye we use Planet Labs’ Level 2 Ortho Product, which grids all imagery to consistent 25 x 25 km tiles at 3.125 m resolution for PlanetScope and 5 m resolution for RapidEye. While no automated cloud mask product exists for either PlanetScope or RapidEye imagery, Planet Labs does provide a cloud index for each image which approximates the percent of pixels in the image that are cloud-obscured. In this study, we examine all images with less than 20% cloud cover and with a sun illumination angle > 20°. In total, 75,999 images (72,414 PlanetScope and 3,585 RapidEye) are analyzed, totaling ~25 TB of data.

Text S2. Lake Classification and Tracking Method

Our lake tracking method is specifically developed to overcome known limitations of CubeSat imagery. These limitations include cross-sensor radiometric calibration inconsistency, lack of atmospheric correction, lack of an automated cloud mask and ~10m geolocation error (Cooley et al. 2017). The method is adapted from Cooley et al. (2017) but improved to enable automated classification at large spatial scales. Broadly, the method involves three main steps: (1) creation of a buffered lake mask which is used both to seed classification and to track changes in lake extent, (2) histogram-based thresholding of water (3) time-series filtering using machine-learning (Fig. S3.1). The entire method is implemented in Matlab R2018b and described as follows.

Creation of Buffered Lake Mask

Our method begins with the creation of a buffered lake mask which includes every lake in the study region. This mask is created through a multi-step process for each 25x25km tile. First, an Otsu classification is used to classify water on a cloud-free early season image. This water classification is then buffered by 60 m to create an initial water mask containing both lakes and surrounding land. Water bodies where the 60 m buffer zone overlaps with the buffer zone of adjacent water bodies are counted as one singular water body for lake tracking. In other words, water bodies whose maximum extent is less than 120 m apart are tracked as a singular water body (Fig. S3.2). While this effect likely reduces the number of lakes and increases the mean lake size, it enables efficient lake tracking and accurate detection of dynamism without "double counting" changes in water bodies occurring less than 120 m apart.

Next, we use the initial water mask to seed water classification of all images with less than 5% cloud cover between June 1 and July 15, using the classification method described below. All the classified images are then summed to create a new water mask including all pixels classified as water in at least 30% of these images. Rivers are removed from the mask and each water body is again buffered by 60 m to produce the final buffered lake mask. Given the importance of this mask for both water classification and lake tracking, we manually check all final buffered lake masks to ensure the maximum extent of lakes is captured and no false water bodies are included.

Water Classification

We use the water classification method described in Cooley et al. (2017) which was initially adapted from Olthof et al. (2015) who applied this method to shortwave infrared Landsat TM and ETM+ imagery. A brief summary is as follows: First, we calculate the normalized difference water index (NDWI; (green – NIR)/(green + NIR), McFeeters, 1996) for each image (Fig. 3-S3a). Next, the buffered lake mask is intersected with the NDWI image to produce a histogram of NDWI pixels contained within the buffered mask (Fig. S3.3b). The buffered water histograms typically have two peaks, one representing water (higher NDWI) and one representing land (lower NDWI). We identify dynamic land and water NDWI threshold values based on the relative height of these two peaks, with all NDWI pixels lower than the land threshold considered to be 100% land and all pixels greater than the water threshold considered to be 100% water (Fig. S3.3b). Pixels in between these two peaks are assigned a fractional water value between 0 and 100 based on their relative distance between the two peaks (Olthof et al., 2015), resulting in a fractional water classification for every image (Fig. S3.3c). Validation of the automated water classification method was performed by manually digitizing the perimeters of 52 lakes in coincident (i.e. within 3 days), higher resolution (1 m) WorldView imagery. By comparing the areas of manually and automatically mapped lakes, we found our classification method had an average RMSE of 11% with no systematic bias towards over- or under-estimation of lake area (Cooley et al., 2017). Furthermore, as our machine learning filtering (described below) removes lakes with poor classification performance, the cumulative impact of water classification error on reported large scale patterns is likely to be minimal.

Lake Area Tracking

Due to the 10 m geolocation uncertainty of CubeSat imagery, traditional pixel-based change detection methods lead to inaccurate results. We therefore track changes in lake area using the 60 m buffered lake mask. For each image, we calculate the total amount of water contained within each individual lake object in the buffered mask, producing a seasonal time series of surface water extent for all lake objects. All pixels with a fractional water value greater than 75% are counted as water this threshold performed best in comparison with higher spatial resolution WorldView imagery (Cooley et al., 2017). The use of the buffered lake mask for lake tracking allows lake boundaries to change over time, minimizing the impact of geolocation error. We only track lake extent for lakes > 0.01 km^2 as below this threshold, the geolocation uncertainty and high signal-to-noise ratio of CubeSat imagery prohibit accurate detection of seasonal variability.

Observation Filtering using Machine Learning

Due to the variable quality of CubeSat imagery and lack of a cloud mask, the raw time series of lake area contain many erroneous data points (Fig. S3.4). We therefore use a machine learning-derived observation filtering process to separate valid and invalid lake observations. The first step of the filtering process is the creation of manual training datasets containing 2-4% of all lakes in each study area, chosen randomly within each 25 x 25 km tile. For each lake observation, we display the NDWI image and the corresponding water classification, as well as the observed lake area in the context of the complete lake area time series. Each observation is then manually marked as valid or invalid based on (a) whether is the image is cloud-free and sufficiently high quality, and (b) whether the classification appears to accurately represent the lake area as it appears in the NDWI image. The training datasets are created separately for each study area, resulting in 4 training datasets each containing 400-600 manually validated lake time series, approximately 28,000-39,200 manually validated lake observations.

For every lake area observation, we calculate 14 predictor variables, namely the day of year, the seasonal median area, the image's cloud index, the type of image (PlanetScope or RapidEye), percent of lake pixels which are marked as 'no data', area as a percent of the seasonal maximum area, as a percent of the seasonal median area, as a percent of the 5-day median area and as a percent of the 10-day median area, the standard deviation of the lake area time series, the 5-day standard deviation, 10-day standard deviation, and finally the perimeter as a percent of the 5-day median perimeter and as a percent of the 10-day median perimeter. These 14 predictor variables calculated for all 28,000-39,200 validated lake observations are used to train a random forest classifier for each study area. By randomly removing a sub-sample of the training dataset, we find that the random forest classifier accurately filters 94-96% of all lake area observations. The most important predictor variables are area as a percent of 10-day median area, cloud index and perimeter as a percent of 10-day median perimeter. We then classify all lake observations as valid/invalid using these random forest classifiers (Fig. S3.4). As a final step, for days where multiple valid lake observations are available, we select the observation closest to the 5-day median, and then apply a 10-day median filter over the entire time series (Fig. S3.4).

While the random forest classifier performs at 94-96% accuracy, we analyze the accuracy of the complete observation filtering method and resulting metrics through a bootstrapping analysis of the manual training dataset. For each study area, 10 lakes are randomly removed from the manual training dataset. Lake area observations from these 10 lake time series are then classified as valid or invalid using a random forest classifier created from the remaining manual training data. As described above, the best observation per day is then selected and a 10-day filter is applied over the entire time series. For each lake, the mean area, maximum area, minimum area and seasonal dynamism (maximum – minimum lake area) are then calculated from both the machine learning-filtered and the manually validated time series. This process is repeated until all lakes in the training dataset have been validated both manually and through machine learning.

Given these 400-600 manually validated and classified lake time series, we then calculate the error associated with the difference between the manually validated and machine-learning filtered results for each study area (Table S3.1). For mean area, the root mean square error (RMSE) ranges from 1,248 – 3,904 m^2, maximum area from 2,997 – 15,409 m^2, minimum area from 973 – 22,978 m^2 and dynamism from 5,660 – 23,135 m^2. For reference, these RMSE values range from 0.2 – 3.6% of the maximum lake area. The Yukon Flats Basin generally has the largest error of all four study areas, likely due to the higher mean percent changes and the greater difficulty in distinguishing lake boundaries in vegetated wetland environments compared to upland shield environments.

Final Products

The process above results in a seasonal lake area time series for every lake in our study areas. Before filtering, lakes receive 66 (+/- 20) observations on average between May 1 and Oct 1, ranging from 48 (+/- 8) in the Mackenzie River Valley (MRV) to 98 (+/- 12) in the Yukon Flats Basin (YFB). These observations cover 42 (+/- 11) unique days on average, ranging from 33 (MRV) to 57 (YFB). Of these daily observations, 64-67% are classified as valid by our filtering method, yielding 37, 21, 32 and 31 observations per lake on average for each study area, respectively. This corresponds to a total of 2.2 million valid individual lake area observations across all four study areas. As these lake area observations are unevenly spread between May to October, we interpolate between lake area observations to produce daily lake area time series that enable summation across many lakes. Finally, we also grid dynamism (seasonal maximum minus seasonal minimum lake area) to a standard 5 km x 5 km grid.

Treatment of ice cover

The chosen study window, May 1 to October 1, was chosen to precede ice-off in order to capture the full seasonal progression of lake area. We do not specifically classify ice from water due to the difficult of distinguishing ice from cloud given the lack of atmospheric correction and radiometric calibration consistency issues in Planet imagery (Cooley et al., 2017). However, ice-covered lake observations are nearly always removed from our analysis through two key steps of the method. First, our water classification requires a characteristic two-peaked NDWI histogram (Fig. S3.5). Images with significant ice cover generally do not have distinguishable "land" and "water" peaks. These ice-impacted images thus fail our classification criteria and are not included in the analysis, therefore automatically removing most of the ice-impacted imagery. Second, if an image with lake ice cover does pass our initial classification criteria, it nearly always leads to an anomalous lake area observation and is therefore removed by the machine learning observation filtering process.

As a result, the timing of first valid lake observation broadly follows spatial gradients in temperature and ice-off timing (Fig. S3.5). While there is significant local variability, associated with differing satellite paths as well as lake size, the broad-scale patterns in timing of first observation clearly reflect large-scale patterns in ice-off. The timing of first observation varies from early May for small lakes in the Yukon Flats Basin to late June/early July for lakes along the Arctic Coast in the Mackenzie River Valley. While not an exact measurement of ice-off timing, as differing satellites paths also influence spatial patterns, the locally variable start dates significantly reduce uncertainty caused by ice presence and allow us to capture the full seasonal progression of lakes.

Text S3. Comparison with In Situ Water Level Data

A critical step of assessing the validity of our results is determining whether the patterns of lake change we document from CubeSat imagery are corroborated by field measurements. To do this, we compare our lake area time series to in situ lake level data we collected in summer 2017 as part of the NASA Arctic-Boreal Vulnerability Experiment (http://above.nasa.gov) (Figures S3.6 and S3.7). We installed pressure transducers at the bottom of nine lakes in the Yukon Flats Basin and along the margins of six lakes in the Canadian Shield Transect using the protocol described in Pitcher et al. (2018). The locations of these lakes are shown in Figure 1 in the main text. Five barometric pressure loggers were also installed in the YFB and CST to correct the lake level records for atmospheric pressure variability. The pressure transducer data is available from June 2 to September 2 in the Yukon Flats Basin and July 7 to September 13 in the Canadian Shield Transect.

We calculate the R^2 between our CubeSat-derived discrete time series observations and in situ lake level over this period for every lake and find that 13 of 15 lakes are correlated at $p < 0.05$, with 12 correlated at $p < 0.01$ (Figures S3.6 and S3.7). All 15 instrumented lakes experience substantial seasonal declines in both water level and lake area. The two lakes whose areas are not significantly correlated to lake level experience very small area variability (~1%, Figure S3.6 and S3.7), likely causing the lack of correlation. Notably, Crossover Lake, Buddy Lake and Lake YF18, all in the YFB, experience transient periods of increases in lake level that correspond well to transient increases in lake area (Fig. S3.6). The slopes of the regression lines between lake area and lake level vary significantly, between 3% change in area per meter water level decline (%/m) (for Thumb Lake) and 140 %/m (for Canvasback Lake) (Fig. S3.7). While there is no significant correlation between slope of regression line and lake size (as found in Smith and Pavelsky, 2009), we do identify a topographic influence on the relationship between lake level and lake area. Lakes located close to the Yukon River in its floodplain experience a larger percent change per meter (e.g. Canvasback Lake at 140%/m, Buddy Lake at 96%/m, Scotor Lake at 46%/m) than lakes located in upland terrain such as the White Mountain Foothills in the YFB and all of the CST (e.g. Thumb Lake at 3%/m, CST #9 and #11 at 8%/m). Overall, the pressure transducer data illustrate seasonal declines in surface water level consistent with our observation of a broad-scale decline in surface water extent, suggesting our CubeSat-derived observations of lake area declines are real, and that the findings of this study are robust.

Text S4. Analysis of Drivers

To evaluate drivers of seasonal dynamism, we perform generalized multivariate linear regression. Generalizable multivariate linear regression is a form of linear regression used when the input and response variables are not assumed to be normally distributed (Liang & Zeger, 1986). We test water fraction (Figure S3.8), total perimeter (Figure S3.9), number of lakes, mean lake size, mean elevation, topographic roughness (calculated as standard deviation of elevation), precipitation minus evaporation (P – E) (Vimal et al., 2018; Figure S3.10), permafrost presence (Brown et al., 2002), mean annual air temperature (GISTEMP) and mean distance from the river network as predictor variables. All variables are standardized to the same 5km x 5km grid, with each individual grid cell considered to be a data point. Given the wide variability in the magnitude and distribution of these variables, we standardize all the variables by calculating their z-score ($z = [x - \text{mean}(x)] / \sigma(x)$, where σ = standard deviation). For each study area, we perform three regression analyses predicting seasonal dynamism: (1) using all predictor variables, (2) using only lake allometric variables (water fraction, total perimeter, number of lakes and mean lake size) and (3) using only environmental variables (elevation, topographic roughness, permafrost presence, mean annual air temperature, P – E, and distance from river). ANOVA (analysis of variance) is used to calculate the amount of dynamism than can be explained by each regression model and by the individual variables.

Text S5. Calculation of R_Δ

A key challenge of attributing patterns in lake extent is the strong relationship between lake size, dynamism and percent change. Simply put, large lakes typically lose more water (i.e. have greater dynamism) than small lakes, as, for example, a 5% change in lake area would result in a much larger total change for a 2 km^2 lake (0.1 km^2) than for a 0.5 km^2 lake (0.025 km^2). Conversely, small lakes typically experience a greater percent change (dynamism divided by maximum lake area) than large lakes, as, for example, a 0.2 km^2 change in surface water area is a 10% change for a 2 km^2 lake but a 40% change for a 0.5 km^2 lake. These two effects combined mean that the observed spatial patterns of dynamism are positively correlated to lake size (larger lakes = higher dynamism, Pearson's $R = 0.60$, $p < 0.001$) whereas percent change is negatively correlated to lake size (larger lakes = smaller percent change, Pearson's $R = -0.11$, $p < 0.001$).

Given the wide variability in water fraction and lake density within the four study areas, these relationships strongly impact the observed spatial patterns of dynamism. Separating lake dynamism from lake size is thus helpful for better understanding the spatial patterns observed independent of lake area. Consequently, we develop a new lake metric we term R_Δ which represents the mean lateral distance between the maximum and minimum lake boundaries (in meters; Fig S3.11). In other words, it represents the mean lateral change along lake shorelines. It is independent of lake area because lateral shrinkage generally does not depend on lake size, and both large and small lakes experience a wide range of R_Δ values. We note that R_Δ is not the exact ground distance between the maximum and minimum lake margins, as it is very difficult to accurately measure this difference given the 10m geolocation accuracy and the differing pixel sizes of the images. Instead, we calculate R_Δ by first resampling the maximum extent of each lake to 1 m x 1 m resolution. We then erode the lake at 1 m increments (i.e. remove 1 m from the lake margin equally in all directions) and calculate the resulting lake area, stopping when the eroded size of the lake is approximately equal to the minimum lake area. The R_Δ value is therefore the amount of erosion (in 1 m increments) which produces a loss of lake area closest to the observed seasonal dynamism; in other words, approximately the mean lateral change along the lake margin. While this method is only accurate to 1 m, the resulting values are independent of lake area and therefore valuable for comparing spatial patterns in dynamism across landscapes with widely varying water fractions.

Text S6. Identification of Vegetation-Impacted Lakes

Upon manual inspection, we find that many of the most dynamic lakes in our study region exhibit a sharp decline from May to late July followed by a gradual increase in lake area in August and September. Closer inspection of the imagery reveals that this characteristic pattern is likely caused by the growth and disappearance of vegetation at the lake's surface. Identification of these "vegetation-impacted lakes" is potentially interesting for research on freshwater carbon cycling (Bastviken et al., 2004; Tranvik et al., 2009) and lake water quality (Palmer et al., 2015). Therefore, to understand the scale and spatial imprint of this phenomenon, we identify all lakes experiencing these "vegetation events" through a combination of automated classification and manual verification. First, we identify candidate vegetation-impacted lakes which meet the following three criteria: (1) a seasonal dynamism greater than 25,000 m^2, (2) a percent change greater than 25% and (3) a positive late summer rebound that is at least 25% of the dynamism. We then visually examine raw CubeSat imagery showing each candidate vegetation-impacted lake's maximum and minimum extents and label those whose seasonal decline and rebound appears to be primarily associated with the growth and decline of vegetation as opposed to hydrologic activity.

We identify 165 vegetation-impacted lakes (1.8% of all lakes) in the Yukon Flats Basin, 425 (1.1%) in the Mackenzie River Valley, 249 (1.2%) in the Canadian Shield Transect and 7 (< 0.1%)

in the Hudson Bay Lowland. These lakes account for 13.2%, 10.8%, 7.1% and 0.4% of the total observed dynamism in each study area, respectively. In total, vegetation-impacted lakes represent 1.0% of all lakes and account for 8.9% of all dynamism across all four study areas. Mapping of these lakes reveals that they tend to occur in clusters, with particular concentration in the Lower Mackenzie Plain (southeast portion of the Mackenzie River Valley) and the southern Canadian Shield Transect (Figure S3.12). While our analysis of vegetation-impacted lakes involved manual verification, future work could use our time series approach to develop automated identification of these events. Future research could also distinguish between vegetation events caused by floating vegetation mats, emergent vegetation or algal blooms, all of which occur within our study areas.

These 1% of lakes we term "vegetation-lakes" represent only lakes where vegetation growth or algal activity occurs over a large portion of the lake. It is possible that some of the other observed lake area time series may be impacted by subtler vegetation changes along lake margins. Quantifying the uncertainty introduced by this effect is challenging and therefore not included in the uncertainty analysis in this paper. However, small vegetation changes along lake margins are unlikely to impact our overall conclusions. Lakes impacted by vegetation typically experience a sharp area decline followed by a late-season rebound. The vast majority of lakes experience peak water extent at the start of the open water season followed by a gradual decline with little-to-no August-September rebound, which suggests that vegetation changes are not a primary driver of this signal, as evidenced by the summed seasonal time series of lake area (Figure 3.2) and the in situ lake level time series. Secondly, there is no evidence to suggest that marginal lake vegetation changes are significantly different in one or another region.

Text S7. Comparison with Global Surface Water Occurrence Product

The Landsat-derived Global Surface Water Occurrence (GSWO) product is perhaps the highest resolution global lake change product currently available (Pekel et al., 2016). GSWO's water occurrence and water change products are built from the entire Landsat record (1977 to 2015). Most relevant to our analysis though is their water seasonality product indicating the number of months water is present in each pixel which is created using only Landsat imagery acquired between 2014 and 2015. Along with the different time periods of the analyses (2014-15 vs. 2017), a key difference between GSWO and our CubeSat analysis is that GSWO is purely pixel-based and thus includes both rivers and their adjacent floodplains as well as areas that may only be water-covered briefly during ice breakup and the subsequent peak river flow. These are all excluded in our analysis as we only track dynamism in lakes > 0.01 km^2 that are present for at least one month.

Consequently, to compare GSWO's seasonality product with our CubeSat product, we apply the same buffered water mask used to track lake extent in CubeSat imagery to the GSWO seasonality product. We then calculate the comparable GSWO seasonal dynamism as the sum of all pixels which are inundated for less than 6 months (the approximate length of the open water season) contained within our buffered lake mask. Using this approach, we find that the coarser resolution (30m, ~16-day revisit time) GSWO product underestimates total seasonal dynamism nearly everywhere except the Mackenzie River Delta (Fig. S3.14). The underestimation is largest in the Canadian Shield Transect (52%) where small marginal changes (low R_{Δ}s) are responsible for the greatest proportion of overall changes. It is important to note that GSWO and our CubeSat product were not acquired over the same time period, and therefore some of the observed differences may derive from inter-annual variability in lake seasonality. However, the differences are greater than any previous estimates of inter-annual variability (e.g. Chen et al., 2014), particularly in areas typically thought to be stable such as the Canadian Shield Transect. Therefore, while we acknowledge the potential influence of inter-annual variability on this comparison, GSWO's underestimation of seasonal dynamism relative to CubeSats suggests that the high spatial resolution of CubeSat imagery allows observation of previously undetected lake marginal changes using remote sensing.

Supplementary Figures

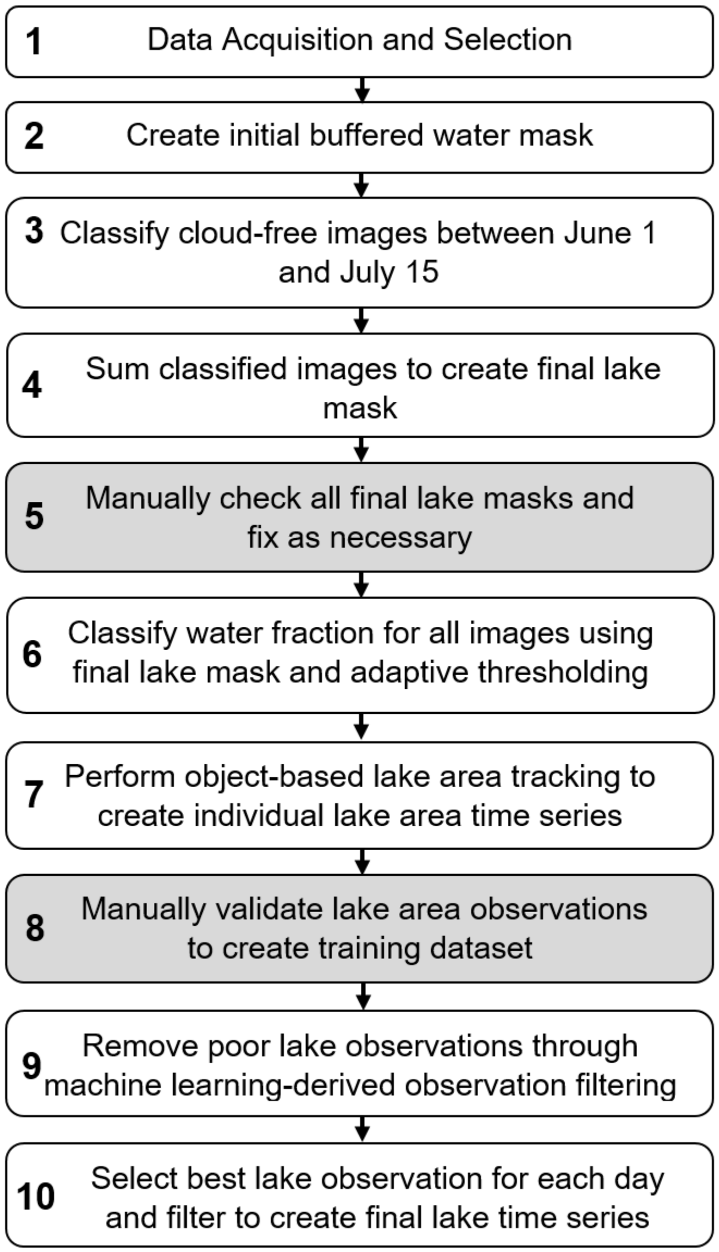

Figure S3.1. Flow chart outlining the steps involved in our CubeSat lake tracking algorithm involving object-based lake tracking and machine learning-derived observation filtering. Shaded gray boxes represent steps that require manual intervention.

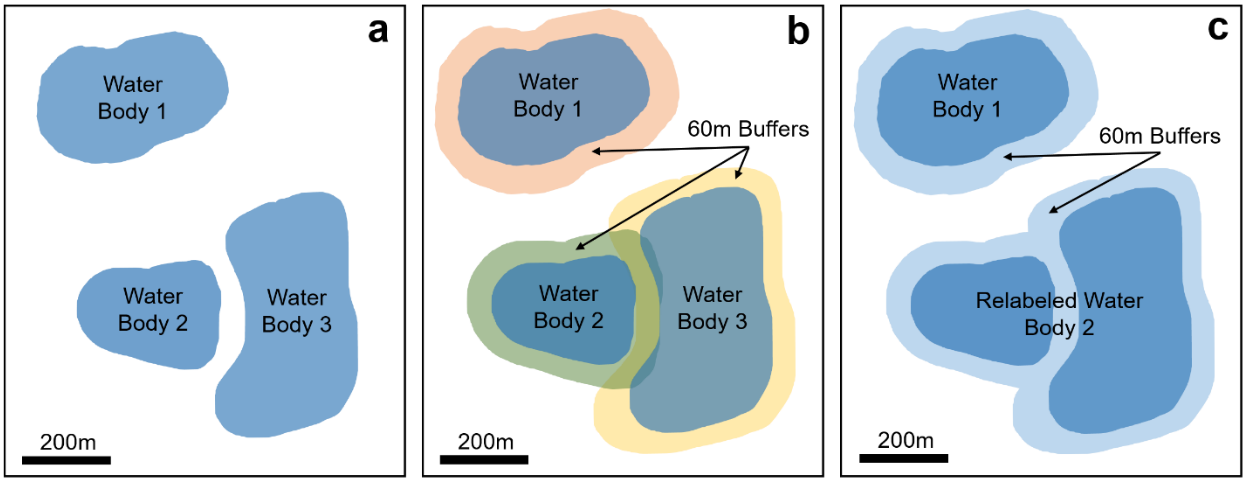

Figure S3.2. Illustration of lake buffering method used for tracking changes in lake area. Panel (a) shows three water bodies located within a small area. Panel (b) illustrates the application of the 60 m buffer, with the individual buffer areas shown in different colors. Water Body 2 and Water Body 3 are less than 60 m apart and therefore their buffered areas overlap. Panel (c) demonstrates how Water Bodies 2 and 3 are thus combined into one water body ("Relabeled Water Body 2") for lake tracking to ensure changes in lake area are not double counted.

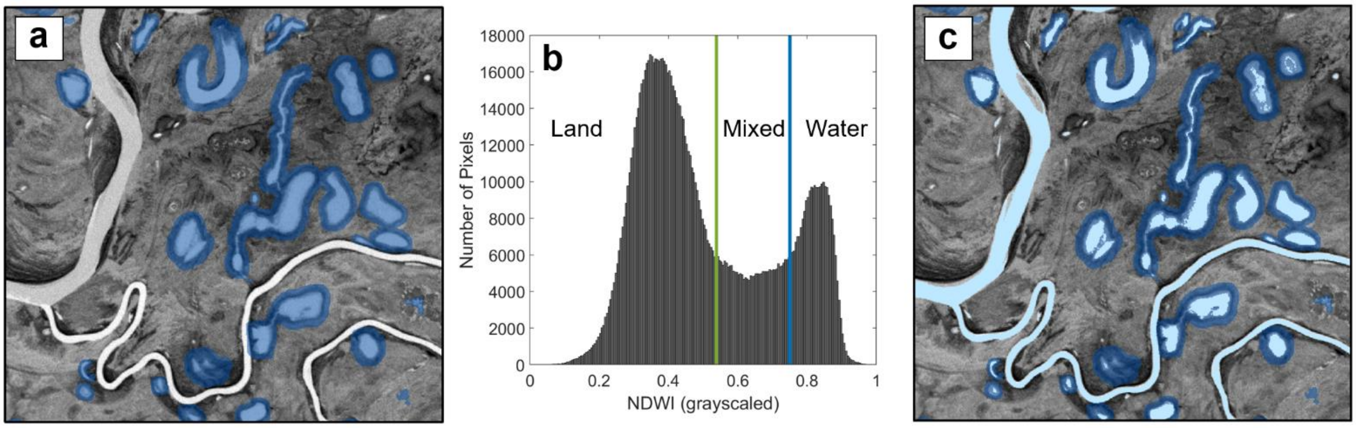

Figure S3.3. Illustration of water classification method. Step (a) shows a normalized differential water index (NDWI) image where lighter shades are water and darker shades are land. This image is overlaid with the final buffered lake mask which is used to seed water classification (in blue). Panel (b) shows the histogram of land and water pixels contained with the buffered lake mask. Using our histogram-based thresholding, we then calculate the land (green) and water (blue) thresholds. All pixels to the right of the water threshold are considered to be 100% water, and the pixels to the left of the land level are considered to be land, with mixed pixels in the middle. Panel (c) shows the resulting water classification with water pixels in light blue overlaid on the NDWI and buffered lake mask. Here we consider all pixels greater than 75% water to be water-covered, as our comparison with WorldView imagery in Cooley et al. (2017) showed this threshold to lead to the most accurate lake area results.

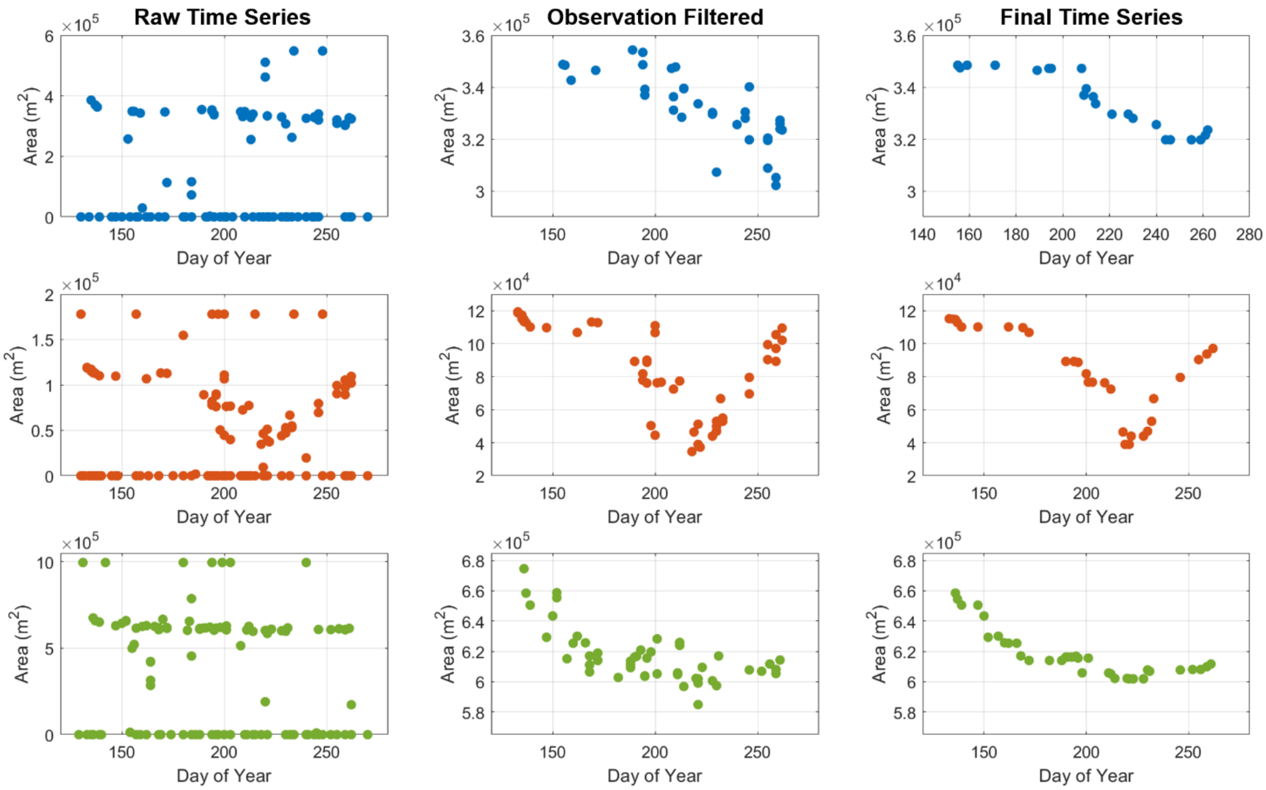

Figure S3.4. Example of our machine-learning time series filtering method. The different colors represent three different lakes. The left column shows the raw time series for three different lakes, where each dot represents an individual image. The large number of zero lake area observations is caused by the small footprint of a PlanetScope swath relative to the size of the image tile. The middle column shows the time series of lake area for the same three lakes after the machine-learning derived observation filtering is performed. Note the y-axis scale has changed. The right column shows the final filtered time series after we select the best observation for each day and apply a 10-day median filter.

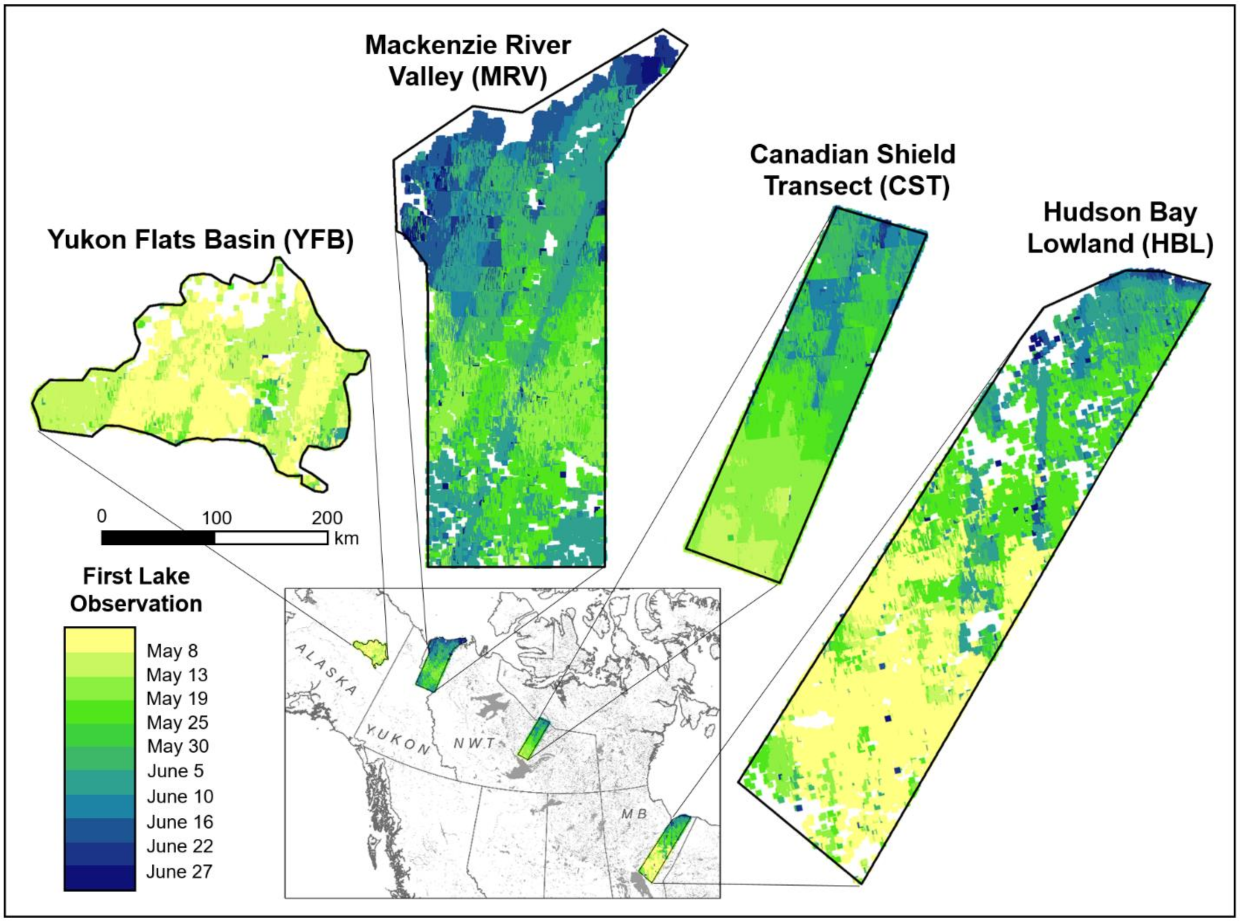

Figure S3.5. Maps of the timing of first valid lake observation for the Yukon Flats Basin, Mackenzie River Valley, Canadian Shield Transect and Hudson Bay Lowland. Each square represents an individual lake, with yellow and light green colors indicating first observation occurring in May and dark green and blue colors indicating first observation occurring in June. The timing of first lake observation follows known temperature gradients and approximately represents the timing of ice-off for each lake. Note the clear influence of different satellite paths and individual image grid tiles on the observed patterns.

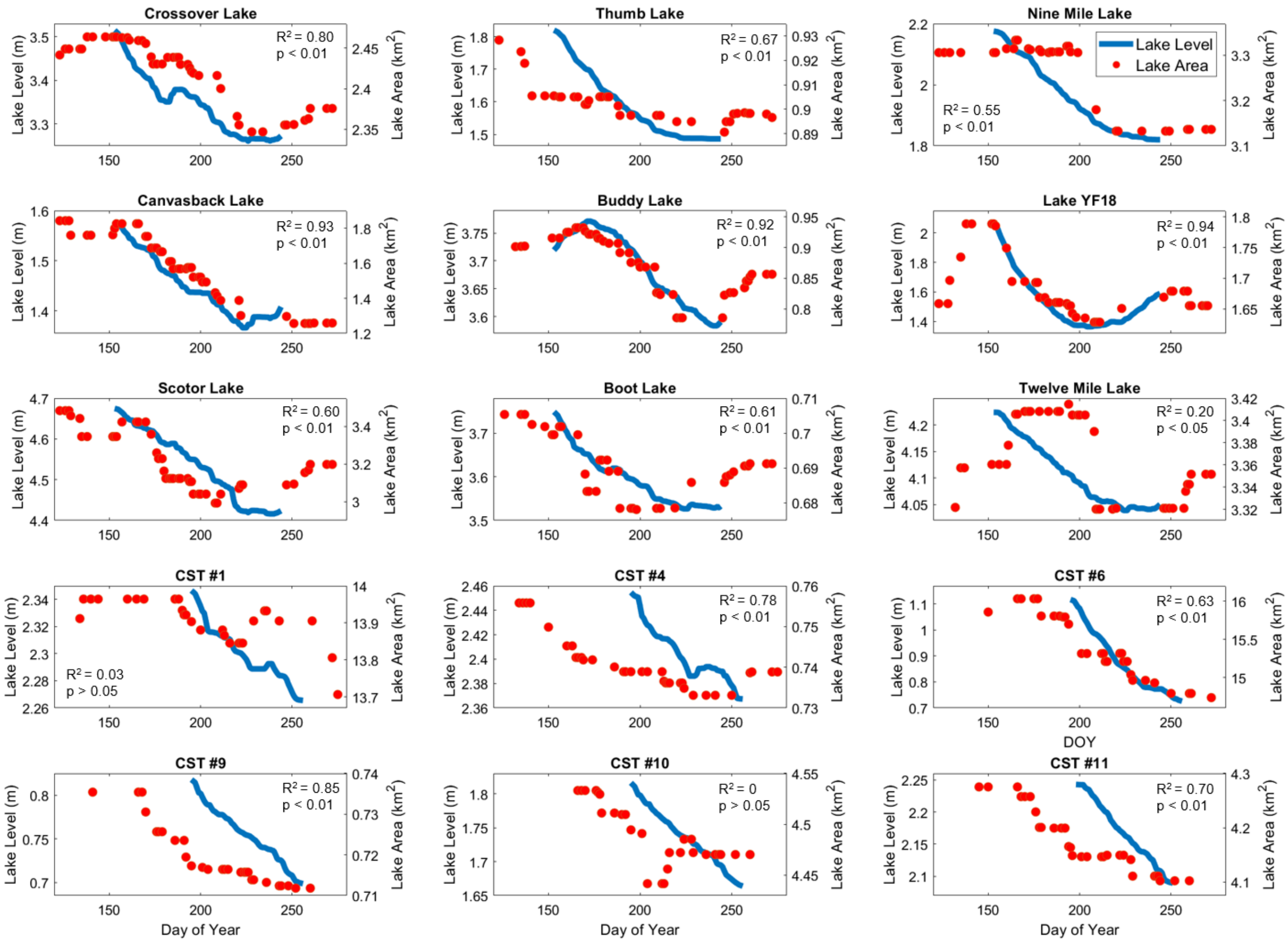

Figure S3.6. Time series comparison between CubeSat-derived lake area observations (km^2, right axes) and in situ lake level data (m, left axes) for 15 lakes from field measurements taken in summer 2017. Blue lines are the lake level records, and red circles show the CubeSat-derived lake area observations. The first three rows are from the Yukon Flats Basin, and the bottom two rows from the Canadian Shield Transect. Pearson's R correlations between the lake level and lake area time series are labeled on each panel. Lake area and lake level are correlated at $p < 0.01$ for all lakes except Twelve Mile Lake ($p < 0.05$) and CST #1 and CST #10 (not correlated). However, for all lakes, seasonal declines in both lake level and lake area are observed. The coordinates of the in situ pressure transducer lake level recorders are as follows: Crossover Lake (66.174, -146.419), Thumb Lake (66.177, -146.149), Nine Mile Lake (66.183, -146.652), Canvasback Lake (66.383, -146.354), Buddy Lake (66.432, -145.452), Lake YF18 (66.785, -145.792), Scotor Lake (66.244, -146.400), Boot Lake (66.075, -146.279), Twelve Mile Lake (66.454, -146.562), CST #1 (63.219, -114.157), CST #4 (63.605, -113.609), CST #6 (63.870, -113.215), CST #9 (64.261, -112.567), CST #10 (64.371, -112.407), and CST #11 (64.463, -112.249). Locations of these lakes are shown as stars in Figure 1 in the manuscript.

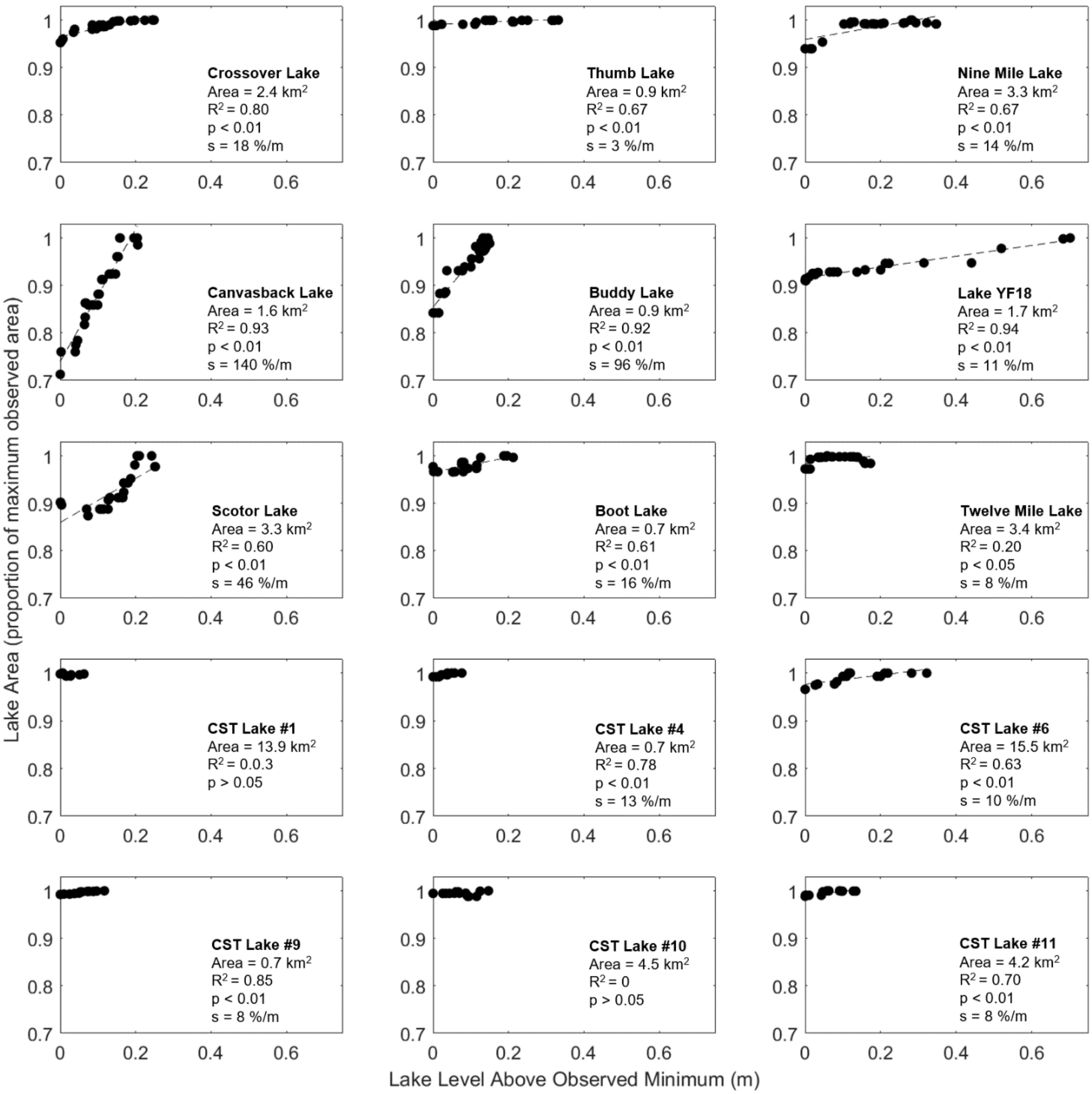

Figure S3.7. CubeSat-derived lake area (as a proportion of maximum observed lake area), vs. lake level (above observed minimum, m) from field measurements for 15 lakes taken in summer 2017. The panels here correspond to the same lakes shown in Figure S4. The first three rows are from the Yukon Flats Basin, and the bottom two rows from the Canadian Shield Transect. Where lake area and lake level are correlated at least $p < 0.05$, the regression line between lake level and lake area is plotted (gray dashed line), and the slope (s) of this line (percent change in lake area per change in lake level, %/m) is noted on each panel, along with the mean area of the lake, and the R^2 and p value of the correlation.

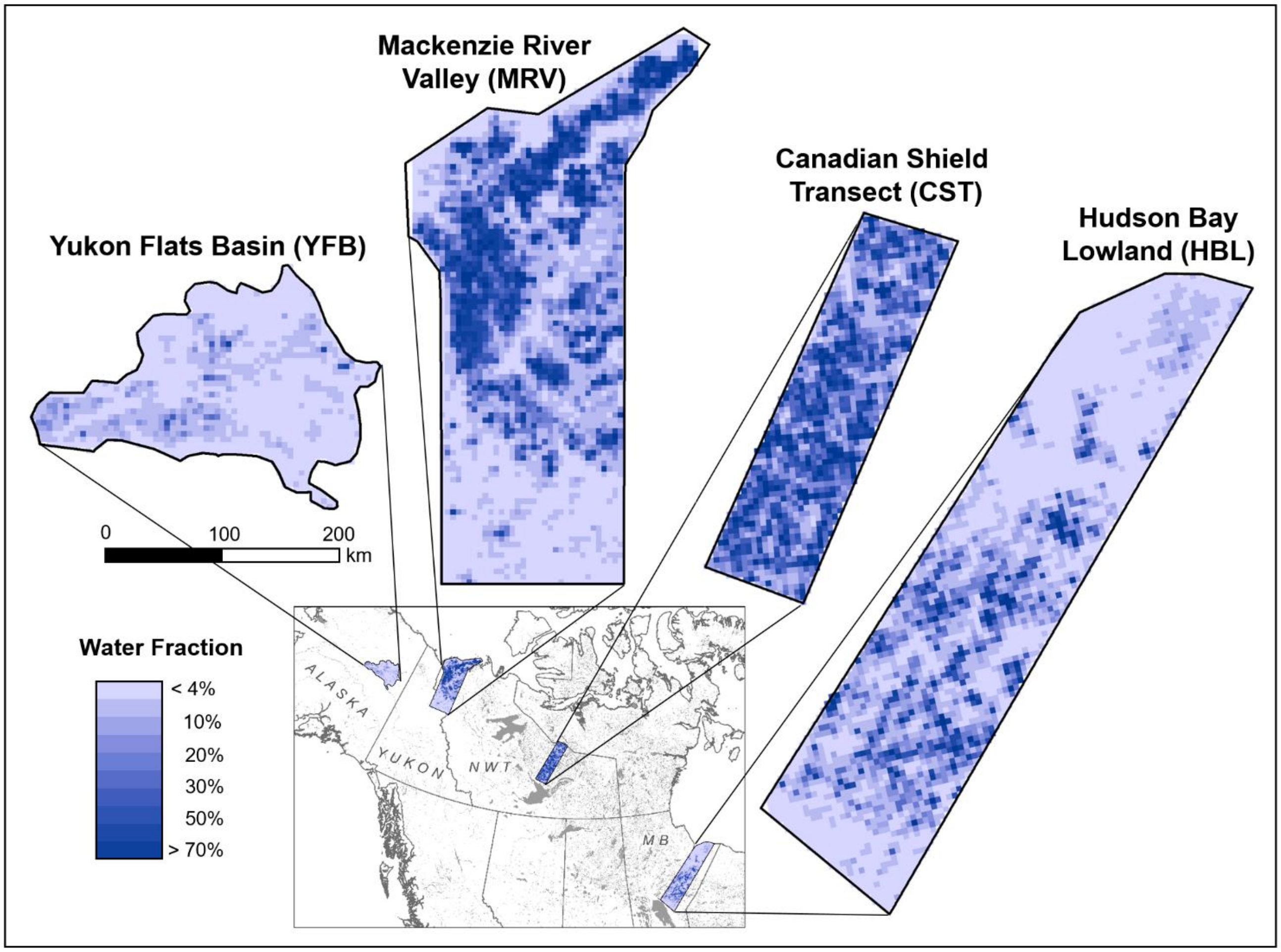

Figure S3.8. Gridded maps of water fraction for the Yukon Flats Basin, the Mackenzie River Valley, the Canadian Shield Transect and the Hudson Bay Lowland. Water fraction refers to the percent of the grid cell which is covered by lake water at every lake's maximum extent. Note the very high water fraction found in the Canadian Shield Transect and in the Mackenzie Delta and Tuktoyaktuk Peninsula in the Mackenzie River Valley.

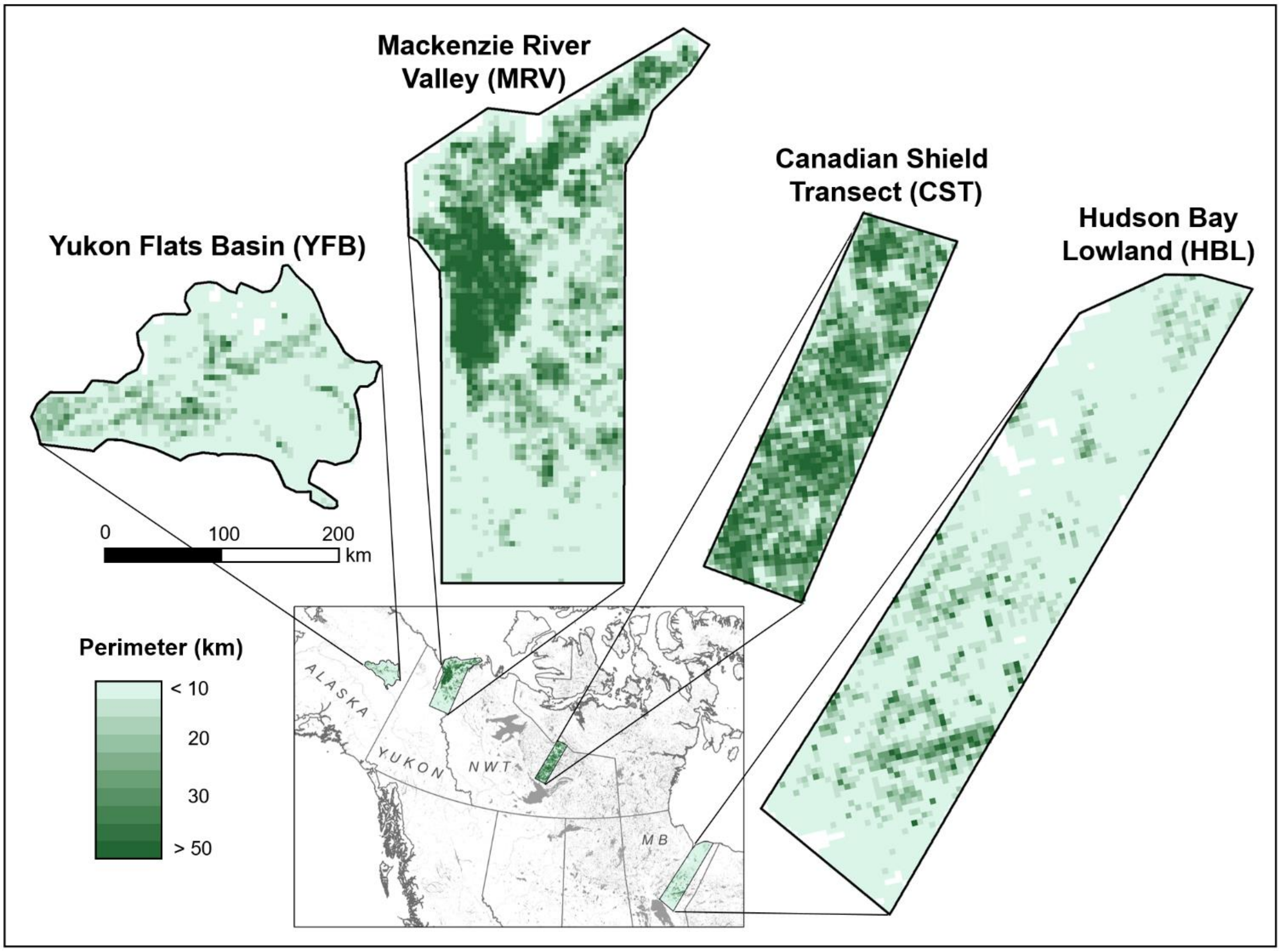

Figure S3.9. Gridded maps of lake perimeter (km) for the Yukon Flats Basin, the Mackenzie River Valley, the Canadian Shield Transect and the Hudson Bay Lowland. Gridded perimeter is calculated as the sum of the perimeters of all lakes contained within each grid cell. Like the water fraction map (Figure S3.6), very high lake perimeters are found in the Canadian Shield Transect and the Mackenzie River Delta/Tuktoyaktuk Peninsula in the Mackenzie River Valley.

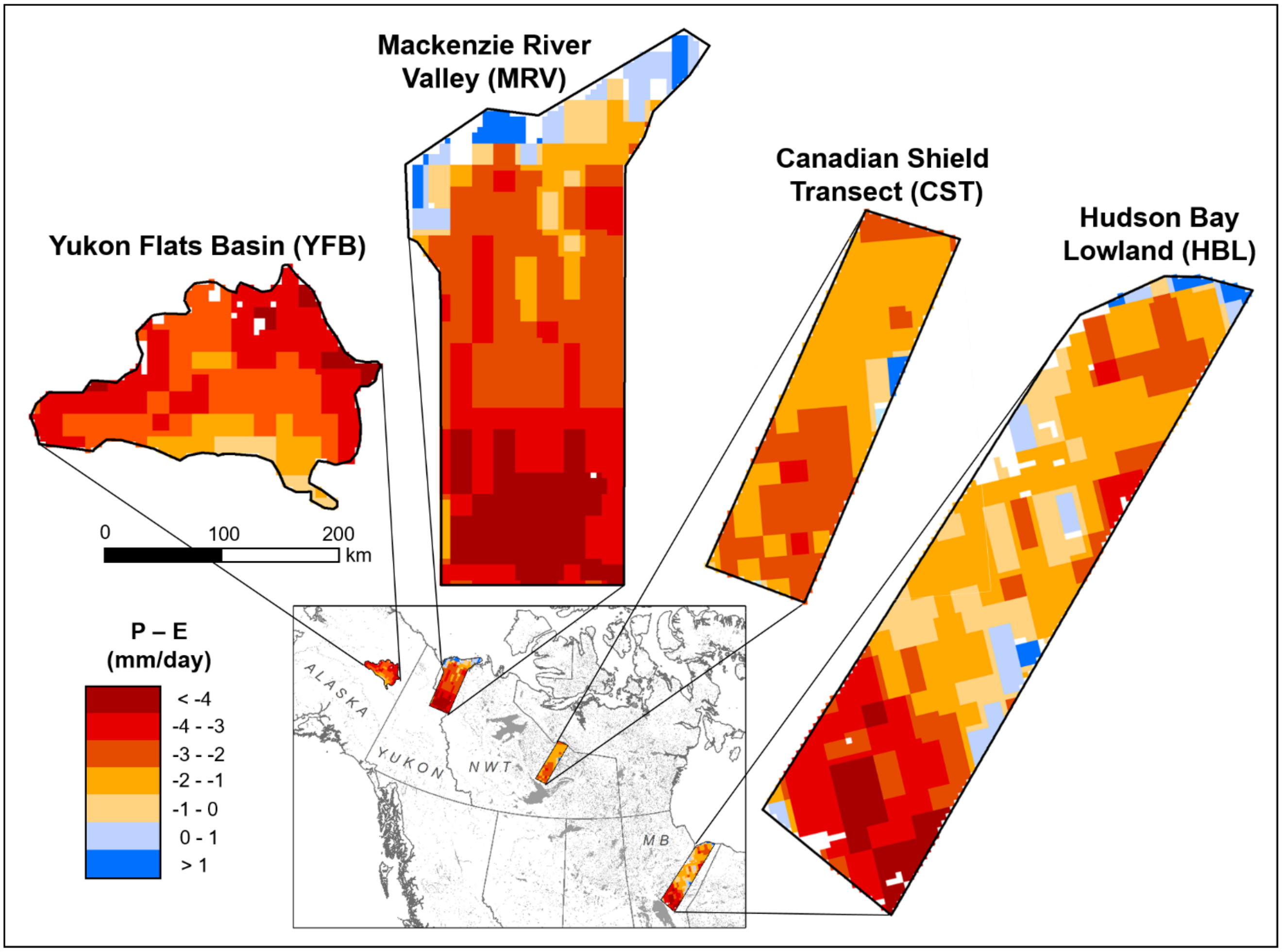

Figure S3.10. Gridded maps of precipitation minus evaporation (P – E) over summer 2017 as simulated by the Variable Infiltration Capacity (VIC) model (Vimal et al., 2018). Orange and red values show areas where evaporation is greater than precipitation (net loss) and blue values show areas where precipitation is greater than evaporation.

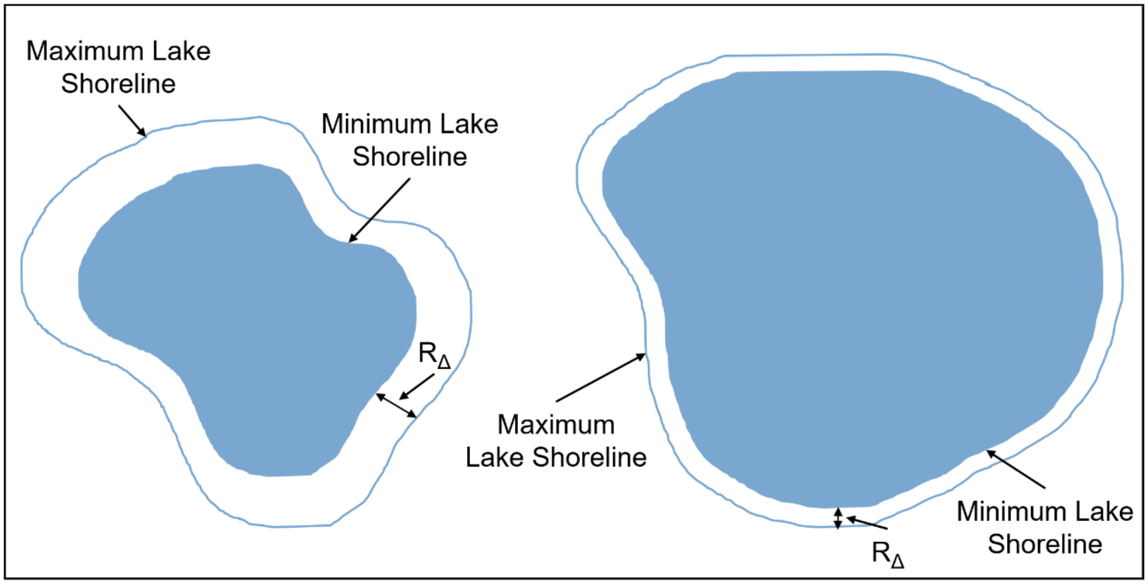

Figure S3.11. Illustration of our new metric R_Δ (in m) which is calculated as the mean lateral distance between a lake's maximum and minimum shoreline boundaries.

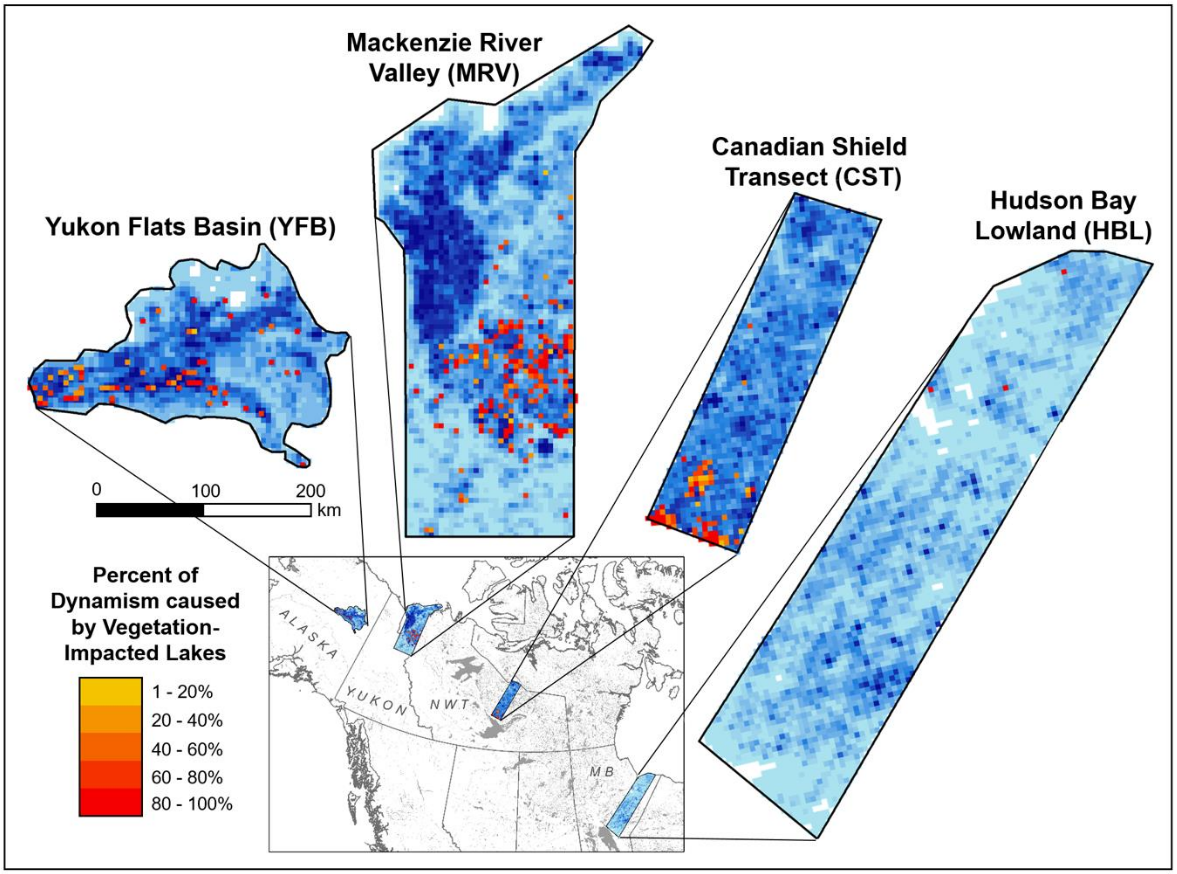

Figure S3.12. Seasonal dynamism caused by vegetation-impacted lakes as a percent of the total dynamism in each grid cell for the Yukon Flats Basin, the Mackenzie River Valley, the Canadian Shield Transect and the Hudson Bay Lowland. Orange and red grid cells contain vegetation-impacted lakes and are colored by the percent of the total dynamism in that grid cell associated with vegetation-impacted lakes. Underneath the gridded vegetation lakes is the gridded map of seasonal water dynamism shown in Figure 1 in the manuscript.

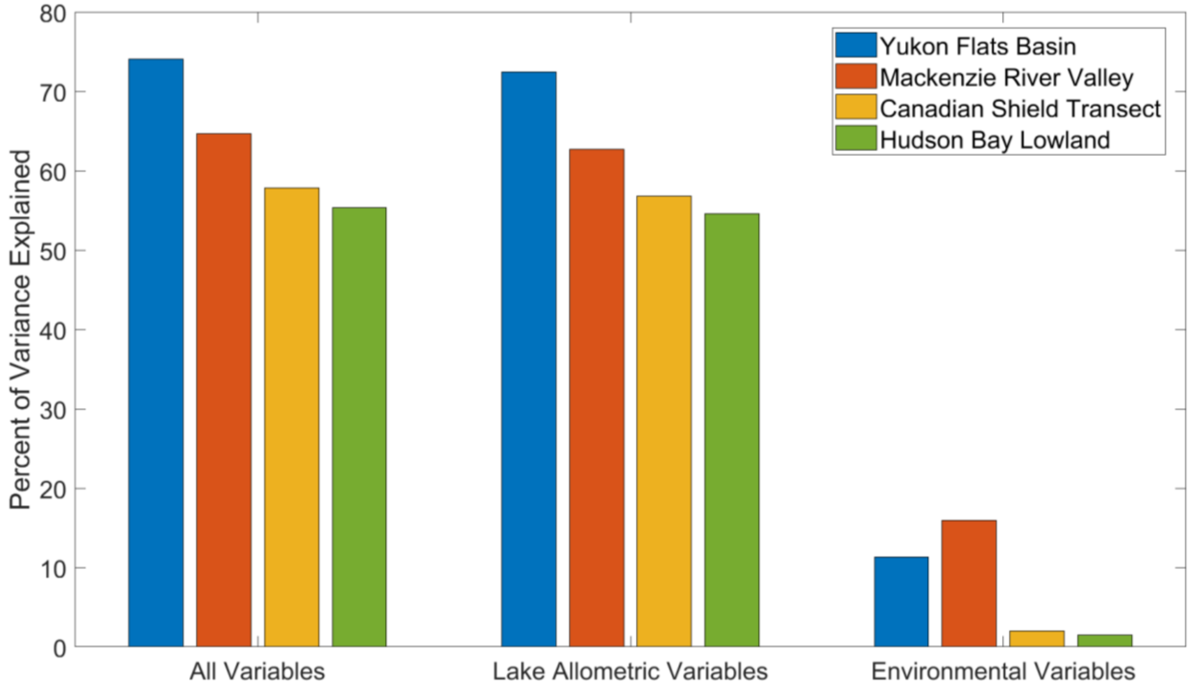

Figure S3.13. Percent of variance explained by each of the multivariate regression models calculated in the driver analysis. The first group shows the percent of variance explained given all 10 predictor variables, and the second group shows the percent of variance explained just using the lake allometric variables (water fraction, total perimeter, number of lakes and mean lake size). The third group shows the percent of variance explained for the environmental variables (permafrost presence, elevation, topographic roughness, mean annual air temperature, P – E and distance from river).

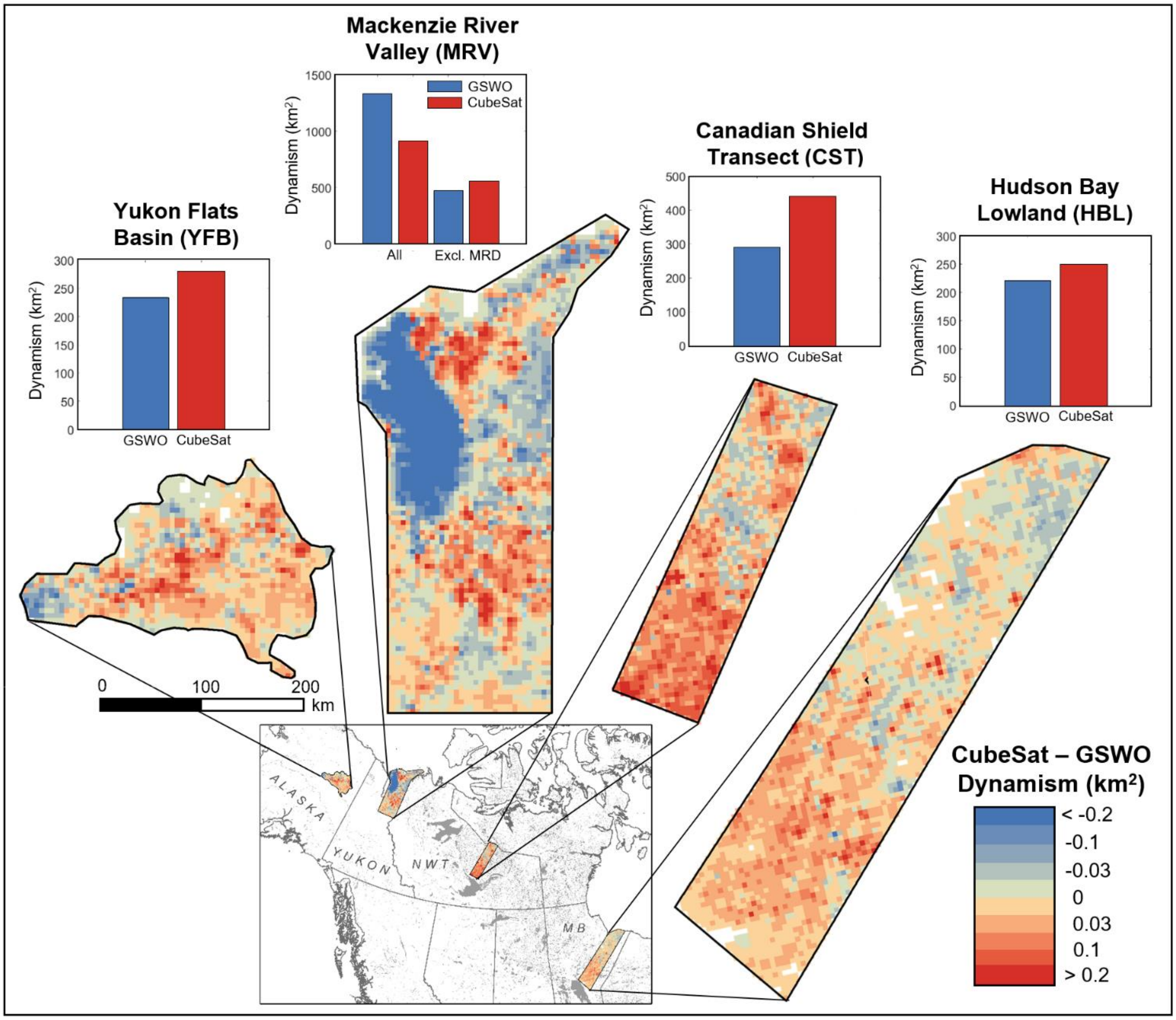

Figure S3.14. Gridded difference between our CubeSat-observed dynamism over summer 2017 and the GSWO seasonality product calculated from 2014-2015 (Pekel et al., 2016) for the Yukon Flats Basin, the Mackenzie River Valley, the Canadian Shield Transect and the Hudson Bay Lowland. Blue tones mean GSWO observes more dynamism, red tones mean CubeSat observes more dynamism. Bar graphs show the total dynamism (in km^2) observed by GSWO (blue) and our CubeSat method (red).

Supplementary Tables

Table S3.1. RMSE (in m^2) calculated from the bootstrapping machine learning error analysis.

	Mean Area (m^2)	Maximum Area (m^2)	Minimum Area (m^2)	Dynamism (m^2)
Yukon Flats Basin	3,854	5,425	22,978	23,135
Mackenzie River Valley	3,591	10,016	7,082	12,672
Canadian Shield Transect	3,904	15,409	11,552	19,185
Hudson Bay Lowland	1,248	2,997	4,973	5,661

Table S3.2. Analysis of variance (ANOVA), regression coefficients and p-values from the multiple linear regression performed for each study area for all predictor variables. Bold numbers show where relationship is significant at $p < 0.05$. Variables which are significant at $p < 0.05$ across all four study areas are also shown in bold.

	Yukon Flats Basin			**Mackenzie River Valley**		
	ANOVA	Coefficient	P-Value	ANOVA	Coefficient	P-Value
Model	74.14			64.66		
Water Fraction	**36.30**	**0.5244**	**0.0000**	**1.26**	**0.1075**	**0.0002**
Perimeter	**29.88**	**0.4069**	**0.0000**	**87.70**	**0.7016**	**0.0000**
Number of Lakes	0.04	-0.0114	0.6423	**0.87**	**-0.0452**	**0.0020**
Mean Size	0.66	-0.0507	0.0680	0.29	0.0377	0.0746
Elevation	**2.47**	**-0.1008**	**0.0004**	**1.21**	**-0.0624**	**0.0003**
Topo Roughness	0.14	0.0208	0.3952	0.04	-0.0103	0.4828
MAAT	**1.48**	**-0.0591**	**0.0065**	**3.71**	**0.1297**	**0.0000**
Distance from River	0.29	-0.0238	0.2310	0.10	0.0139	0.3000
P - E	0.17	0.0155	0.3550	**0.38**	**-0.0383**	**0.0408**
Permafrost	**2.71**	**-0.0745**	**0.0002**	**4.45**	**-0.1005**	**0.0000**
Residual	25.86			35.34		
	Canadian Shield Transect			**Hudson Bay Lowland**		
	ANOVA	Coefficient	P-Value	ANOVA	Coefficient	P-Value
Model	57.83			55.31		
Water Fraction	**23.26**	**0.5539**	**0.0000**	**8.17**	**0.4719**	**0.0000**
Perimeter	**22.27**	**0.3886**	**0.0000**	**40.12**	**0.5339**	**0.0000**
Number of Lakes	**0.90**	**0.0466**	**0.0437**	0.32	-0.0286	0.0808
Mean Size	**6.56**	**-0.2034**	**0.0000**	**3.94**	**-0.2581**	**0.0000**
Elevation	**3.49**	**-0.2345**	**0.0001**	**0.82**	**-0.1225**	**0.0053**
Topo Roughness	0.03	0.0073	0.7028	**1.27**	**0.0508**	**0.0005**
MAAT	**1.06**	**-0.1725**	**0.0284**	0.09	0.0429	0.3649
Distance from River	0.04	0.0082	0.6742	0.47	-0.0300	0.0346
P - E	0.07	0.0110	0.5686	0.08	-0.0141	0.3810
Permafrost	0.16	-0.0337	0.4011	0.01	-0.0131	0.7244
Residual	42.17			44.68		

Conclusion

Summary and Future Work

This dissertation demonstrates how the combination of high temporal resolution satellite imagery and creative methodological approaches can be used to document dynamic Arctic environmental change. The three chapters in this dissertation build upon other research I completed prior to starting my PhD, which include the use of MODIS imagery to map the timing of river ice breakup (Cooley & Pavelsky, 2016) and to identify observation bias in detection of supraglacial lake drainage events on the Greenland Ice Sheet (Cooley & Christoffersen, 2017). Overall, this body of research has leveraged near-daily satellite imagery to advance our understanding of key cryospheric and hydrologic processes and their response to climate change.

Chapter 1 presents one of the first uses of optical satellite imagery to map shorefast sea ice and in doing so enables accurate detection of breakup timing over larger areas and longer timescales than previously possible. To build upon this work, future research should include mapping of shorefast ice edge position along with breakup timing, as ice edge position is also important for marine mammal habitat, access to traditional hunting grounds and preventing coastal erosion (Mahoney, 2018). Other remaining questions include whether the strong atmospheric control on breakup timing and northward trend in sensitivity observed for Canadian and Greenlandic communities is representative of the entire pan-Arctic region, and the degree to which ocean temperatures, winds and waves also influence ice formation and breakup. Such improved understanding of these processes could ultimately enable better operational and long-term forecasting of shorefast ice conditions vital for community members (Eicken et al., 2009).

Chapters 2 and 3 represent some of the very first hydrologic applications of CubeSat imagery and present key methodological approaches required for accurate use of this new data source. In my view, the principal challenge of working with CubeSat imagery is the sheer data volumes required. Future work should thus involve integration of CubeSat imagery into cloud platforms to enable mapping of surface water dynamics at pan-Arctic or continental scales. Such work could yield valuable insight into lake size distribution and intra- and inter-annual variability, which are both critical for upscaling methane and carbon dioxide emissions (Bastviken et al., 2004, 2011; Holgerson & Raymond, 2016). This analysis could also enable better understanding of rapid thermokarst lake drainage events, which are important mechanisms of landscape change in permafrost regions (Kokelj & Jorgenson, 2013) and can lead to organic carbon sequestration (Jones et al., 2012).

Reflections

CubeSat Imagery

My PhD research, and more broadly my growth as a scientist, has benefitted from the massive growth in CubeSat imagery over the past 5 years and my involvement with the leading operator of CubeSats, Planet Labs. When I started my PhD in the fall of 2016, very little research had involved commercially-acquired CubeSat imagery. While Planet Labs began launching satellites in 2013, the imagery available in 2016 was sparse outside of the continental United States and often poor in quality. Most scientific uses of the imagery were for visualization or scene-by-scene analysis (e.g. Kääb et al., 2018), and even the most advanced CubeSat research at the time primarily relied on RapidEye imagery (Jain et al., 2017) or focused on fusion with Landsat imagery (Houborg & McCabe, 2016). After connecting with Planet Labs, my initial plans were to use CubeSat imagery to continue studying Greenland Ice Sheet surface hydrology, but I quickly realized that the imagery had much greater potential for investigating terrestrial hydrology. I therefore shifted the trajectory of my PhD and began work on evaluating the capabilities of CubeSat imagery for observing surface hydrology over a small area in central Alaska. This research, now Chapter 2 in this dissertation, ended up being one of the very first scientific evaluations of Planet CubeSat imagery. However, during this work, I realized that the key question is not whether CubeSat imagery can be used to study surface hydrology but instead whether it can be reliably and efficiently applied over large areas. I thus sought to assess CubeSat's broad-scale applicability by improving the method and applying it over diverse climatic and physiographic terrains in Northern Canada and Alaska.

While working on this upscaling, I learned an important lesson about the challenge of balancing data-driven versus hypothesis-driven science. With an exciting new dataset such as CubeSat imagery, it is easy to focus on all of the amazing things we can do with the data instead of what specific scientific questions this dataset can answer. As I worked on Chapter 3, I became so invested in the creation and upscaling of the method that I lost sight of the scientific motivations of the work. When I finally finished producing lake area time series over all of my study areas, I found myself feeling directionless as to how to extract meaningful results from the analysis. After revisiting the literature on lake dynamics, I eventually decided to focus on the implications of many small fluctuations along lake margins for estimates of freshwater greenhouse gas emissions and ended up with a concise, scientifically-sound paper narrative. This experience emphasized to me the value of hypothesis-driven research, and since then I have endeavored to conduct research clearly motivated by specific scientific questions or hypotheses. For example, in Chapter 1 (which chronologically was completed after Chapters 2 and 3), I sought to determine (1) how shorefast ice breakup timing had changed over the past 19 years and (2) whether springtime air temperature controls breakup timing. This intent led to a much cleaner narrative and an easier manuscript to write. That said, I still believe that there is a place for data-driven research within earth science, particularly with exciting new datasets such as CubeSats, and I do not think the approach taken in chapters 2 and 3 is inherently flawed. Moving forward, I hope to approach new datasets with a key question or hypothesis while continuing data exploration and remaining open to the novel findings that often come with it.

Overall, when I started working with CubeSat imagery, there was a lot of uncertainty regarding the sustainability of Planet's business model and I frequently received questions as to whether the imagery actually had scientific value. While I never regretted my decision to work with CubeSat imagery, during the first few years I certainly thought there was a fair amount of risk in this choice as more senior scientists would often doubt the importance or broad applicability of my work. It has thus been so exciting to watch the field of CubeSat research grow over the past 4 years, from only a handful of people meeting at AGU to now a full booth for Planet Labs and nearly 100 abstracts mentioning use of CubeSat imagery. I now feel tremendously fortunate to have been a part of this growth and am very grateful to have found this niche to establish myself as a scientist.

Engaging with Arctic Communities

While remote sensing is clearly a key tool for documenting Arctic environmental change, perhaps the most impactful lesson I have learned during my PhD is the value of engaging with local Arctic residents. Traditionally, most Arctic research has largely ignored local communities, focusing instead on globally relevant questions such as ice sheet mass balance, sea ice decline and permafrost-carbon feedbacks. When combined with the colonialist history underlying much of the Arctic and the substantial social, cultural and economic challenges facing Indigenous communities, it is no wonder that many communities have often felt resentful towards the scientists who pass through their communities briefly each summer. Recently, however, there has been a growing emphasis within the scientific community on the value of traditional Indigenous knowledge and the importance of collaborating with these communities to conduct research that addresses their needs.

Over my PhD, I have consistently sought out opportunities to learn about how best to engage with Arctic communities. During my first year of my PhD, I presented at a NASA Climate Science Communication Workshop in Yellowknife, Northwest Territories, Canada, which was my first introduction to interacting with local Indigenous stakeholders. I then participated in the inaugural International Arctic Field School which took place over 10 days in Iqaluit, Nunavut, Canada and included both PhD students from around the world and local Inuit students. Speaking to Indigenous students and learning about their perspectives on climate change and interactions with scientists inspired me to think about how my research could better inform their needs. This experience ultimately informed my decision to research shorefast ice breakup in Canadian and Greenlandic communities. As a result, I then the opportunity to put what I learned into action during shorefast ice fieldwork in Uummannaq, Greenland. During our two weeks in Uummannaq in spring 2019, our primary goal was simply to learn from community members and build connections, and hence we spent most of our time in community hotspots such as the harbor, children’s home and sole cafe. It was a sharp departure from the clear, measurable objectives of my previous field experiences, yet our field campaign was ultimately successful in that we had the opportunity to speak to several community members and gained substantial insight into community perspectives on shorefast ice.

From all of these experiences, I have learned that engaging positively and productively with Arctic communities is challenging but possible. Ideally, to be successful in co-producing knowledge with Inuit communities, one would need to spend years visiting a community, slowly building connections and gaining understanding of how the community functions before identifying research questions. However, this system of knowledge production is inefficient and impractical in most scenarios, and therefore the challenge facing scientists seeking to do ethical Arctic research is how to best balance the needs and perspectives of local stakeholders within the constraints of funding agency/university directives and timelines. I still have a long way to go towards this goal but I have learned that patience, respect and clear communication and intent are critical. As I continue my career as an Arctic researcher, I hope to be able to continue to visit Arctic communities, to communicate the results of my research with local stakeholders, to allow their perspectives to inform my work and to eventually be able to co-produce knowledge. Overall, I am very grateful for all of the experiences I had throughout my PhD that have pushed me towards conducting more responsible and locally-oriented Arctic research.

References

Bastviken, D., Cole, J., Pace, M., & Tranvik, L. (2004). Methane emissions from lakes: Dependence of lake characteristics, two regional assessments, and a global estimate. *Global Biogeochemical Cycles*, *18*(4), 1–12. https://doi.org/10.1029/2004GB002238

Bastviken, D., Tranvik, L. J., Downing, J. A., Crill, P. M., & Enrich-Prast, A. (2011). Freshwater methane emissions offset the continental carbon sink. *Science*, *331*(6013), 50. https://doi.org/10.1126/science.1196808

Cooley, S. W., & Christoffersen, P. (2017). Observation Bias Correction Reveals More Rapidly Draining Lakes on the Greenland Ice Sheet. *Journal of Geophysical Research: Earth Surface*, *122*. https://doi.org/10.1002/2017JF004255

Cooley, S. W., & Pavelsky, T. M. (2016). Spatial and temporal patterns in Arctic river ice breakup revealed by automated ice detection from MODIS imagery. *Remote Sensing of Environment*, *175*, 310–322. https://doi.org/10.1016/j.rse.2016.01.004

Eicken, H., Lovecraft, A. L., & Druckenmiller, M. L. (2009). Sea-Ice System Services: A Framework to Help Identify and Meet Information Needs Relevant for Arctic Observing Networks. *Arctic*, *62*(2), 119–136.

Holgerson, M. A., & Raymond, P. A. (2016). Large contribution to inland water CO2and CH4emissions from very small ponds. *Nature Geoscience*, *9*(3), 222–226. https://doi.org/10.1038/ngeo2654

Houborg, R., & McCabe, M. F. (2016). High-Resolution NDVI from planet's constellation of earth observing nano-satellites: A new data source for precision agriculture. *Remote Sensing*, *8*(9). https://doi.org/10.3390/rs8090768

Jain, M., Mondal, P., Galford, G. L., Fiske, G., & Defries, R. S. (2017). An Automated Approach to Map Winter Cropped Area of Smallholder Farms across Large Scales Using MODIS Imagery. *Remote Sesning*, *9*(566). https://doi.org/10.3390/rs9060566

Jones, M. C., Grosse, G., Jones, B. M., & Anthony, K. W. (2012). Peat accumulation in drained thermokarst lake basins in continuous, ice-rich permafrost , northern Seward Peninsula, Alaska. *Journal of Geophysical Research*, *117*, 1–16. https://doi.org/10.1029/2011JG001766

Kääb, A., Leinss, S., Gilbert, A., Bühler, Y., Gascoin, S., Evans, S. G., … Chao, W. (2018). Massive collapse of two glaciers in western Tibet in 2016 after surge-like instability. *Nature Geoscience*, 1–10. https://doi.org/10.1038/s41561-017-0039-7

Kokelj, S. V., & Jorgenson, M. T. (2013). Advances in thermokarst research. *Permafrost and Periglacial Processes*, *24*(October 2012), 108–119. https://doi.org/10.1002/ppp.1779

Mahoney, A. R. (2018). Landfast Sea Ice in a Changing Arctic. In E. Osborne, J. A. Richter-Menge, & M. O. Jeffries (Eds.), *Arctic Report Card 2018*.